Development of a Ray-Tracing Tool with Curvature Extraction Method to Perform Electromagnetic Simulations to Generate Synthetic Radar Data for Machine Learning

Mohannad Saifo

Dissertation

A thesis presented for the degree of
Doctor of Engineering (Dr.-Ing.)

School of Electrical, Information and Media Engineering
University of Wuppertal
Germany
Wuppertal, 2025

First examiner	Prof. Dr. rer. nat. Markus Clemens
Second examiner	Prof. Dr.-Ing. Bernd Tibken
Day of the exam	28.November 2025

Development of a Ray-Tracing Tool with Curvature Extraction Method to Perform Electromagnetic Simulations to Generate Synthetic Radar Data for Machine Learning

Mohannad Saifo

Abstract

The radar (radio detection and ranging) sensor is increasingly used in the automotive industry for sensing the environment of a car with its ability to detect a target's location and radial velocity with good precision. It is used for driver assistance features, increasing safety and enhancing driving experience, and is under development to be used for autonomous driving. Driver assistance features include: adaptive cruise control (ACC), blind spot monitoring (BSM), and automatic emergency braking (AEB). Developing these algorithms requires a large amount of data for tuning and validation, especially when utilizing machine learning techniques, which are used evermore for functions like object recognition and environment perception. To generate this data, either a measurement campaign should be undertaken or simulation techniques can be utilized. Several simulation methods are available like the finite element method (FEM), method of moments (MOM), or the physical optics method (PO). For large scenes, it is impossible to use the first two because they are full wave methods and very computationally expensive. Therefore, asymptotic methods are more suitable for this purpose.

In this work, a simulation tool is built using the programming language C++ with a modified version of PO called the modified equivalent current approximation (MECA) along with geometrical optics (GO) to account for the multi-bounce effect. In driving scenarios, the objects are on the ground, which causes what is called the multi-path effect. Accounting for this phenomenon by including the ground in the simulation leads to a very long run time. Therefore, the multi-path effect is implemented by assuming a virtual ground and mirroring the antenna with respect to the ground. A problem arises when simulating objects with curved surfaces due to the process of converting the object into a mesh of flat triangular facets, leading to error in the resulting RCS because of the deviation between the actual curved surface and the flat facets representing it. A study on this effect is conducted, quantifying the error with respect to the maximum surface deviation defined when meshing the object, and two solutions

are suggested. The first one is to mesh the object with a specific maximum surface deviation which generates suitable mesh and accurate results. The second one is used especially when the original CAD file of the object is not available but only the triangle-based mesh, which is to estimate the curvature from the triangular mesh and then find the intersection point and the normal using our suggested method, which resulted in much better results.

To generate results in close to real-time speed, it is proposed to use a representation of the target by a point scattering center with an RCS map in two dimensions: angle and range. Then the multi-path effect is applied using the four-path model in Matlab, which is much faster than including the ground in the simulation.

Lastly, one effect of the fascia of the car on the radar signal is studied, which is the ghost targets resulting from the reflection of the transmitted signal off the internal surface of the fascia and metal structure of the car.

Acknowledgments

I would like to express my sincere gratitude to all those who supported and guided me throughout the course of this research.

First and foremost, I would like to thank Prof. Markus Clemens, my academic supervisor, for his invaluable guidance, insightful feedback, and continued support throughout this doctoral journey. His expertise and encouragement have been instrumental in shaping the direction and depth of this work.

I am especially grateful to Dr. Alexander Ioffe, Group Leader at Aptiv, for his outstanding mentorship, technical expertise, and leadership throughout my time at the company. His guidance was fundamental to the successful completion of this work, and I greatly appreciated the opportunity to benefit from his deep knowledge and experience.

I would also like to extend my sincere thanks to Dr. Markus Stefer, Engineering Manager at Aptiv, for his valuable support, insightful discussions, and consistent readiness to assist throughout my time at the company. His contributions added meaningful depth to various aspects of the research and were truly appreciated.

I would like to thank Dr. Dennis Volbracht for his support and encouragement, which I greatly appreciated during the course of this work.

I am also thankful to Dr. Xiuzhang Cai and Bruno Camps for their kind cooperation and support during this research, which greatly contributed to its successful progress.

My sincere thanks go as well to Aptiv Services Deutschland GmbH for providing the funding, environment, resources, and opportunity to conduct my research within their organization.

Finally, I extend my appreciation to my colleagues, friends, and family for their unwavering encouragement and support.

Contents

Chapter 1

Introduction

Cars are increasingly becoming dependent on environment perception sensors to enable their sophisticated advanced driver assistance systems (ADAS) features like adaptive cruise control (ACC), emergency breaking, lane assist, collision avoidance and parking assistance. To enable these functionalities, four main types of sensors are employed: cameras, ultrasonic sensors, light detection and ranging (LiDAR), and radio detection and ranging (radar). Radar works by transmitting electromagnetic waves to travel in the environment, reflect off the surrounding objects, and return back to the receiving antennas. Using signal processing algorithms, it is capable of finding the position and velocity of the object, giving the radar several advantages like:

- The ability to function effectively in adverse weather conditions such as fog, rain, and snow, as well as darkness.
- Radar systems can detect and track objects over long distances compared to other technologies.
- Specifying range and velocity in high accuracy.

Radars are used as a set surrounding the car to sense the environment in all directions, including the blind spot for the driver (Fig. 1.1).

Recent advancements in autonomous driving are promising much safer roads due to the elimination of human errors. These systems require state-of-the-art sensors and artificial intelligence algorithms to be robust. The most utilized field of artificial intelligence is machine learning using neural networks. To develop these networks, train, and validate them, a large amount of sensor data is required. This is usually done by driving campaigns to collect data from actual measurements. Although this is the most accurate way, it is a very time-consuming and expensive operation. Therefore, simulation methods are

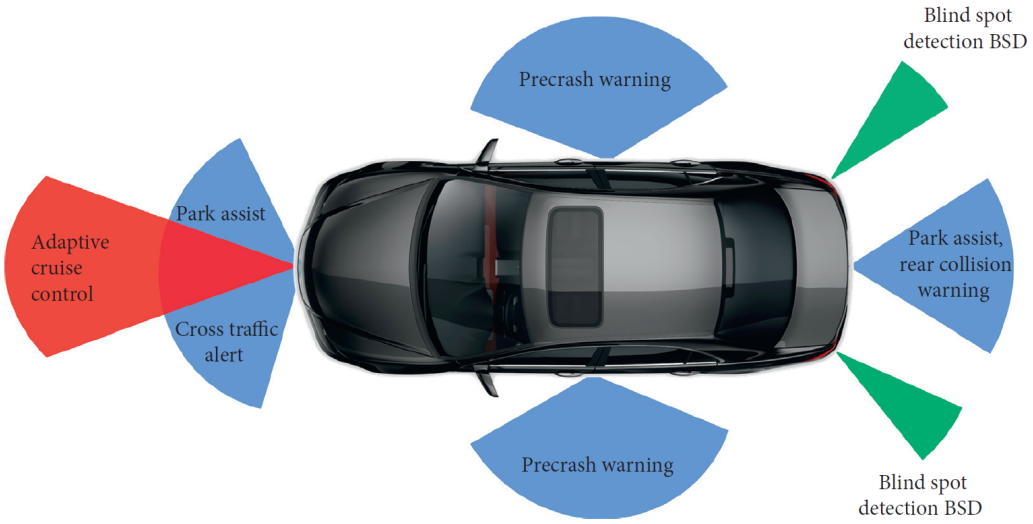

Figure 1.1: Set of radars surrounding a car [1].

being used to generate synthetic data in a more cost-effective way [1]. It is also used to simulate cases that are difficult or risky to evaluate in a traditional way, like car accidents. There are several electromagnetic discretization methods, like the finite difference time domain method (FDTD), the finite element method (FEM), the method of moments (MOM), and the multi-level fast multi-pole method (MLFMM). These are the so-called full-wave methods. They provide a high accuracy, but they are computationally demanding. When dealing with typical driving scenarios, the targets are electrically large in terms of wavelength, which is $3.9\,\mathrm{mm}$ at $77\,\mathrm{GHz}$. Therefore, other methods are developed to tackle these cases, such as geometrical optics (GO), physical optics (PO), shooting and bouncing rays (SBR), the geometrical theory of diffraction (GTD), and the physical theory of diffraction (PTD). These methods are called asymptotic methods because they are approximate solutions to the problem, assume smooth surfaces of the targets, and use rays to simulate the electromagnetic wave propagation instead of solving Maxwell's equations in space.

When simulating a large scenario, another phenomenon occurs, which is multi-path propagation. It happens because the electromagnetic waves travel to the target, get reflected by it, and travel back to the radar in two ways: direct and indirect (Fig. 1.2). This results in four paths between the radar and the target: direct-direct, direct-indirect, indirect-direct, and indirect-indirect. Therefore, to get accurate results during the simulation, this effect needs to be emulated correctly. If the road is included in the simulation as an object and meshed to account for the multi-path effect, too many rays need to be shot at the road to find which ones hit the object, and this will increase the simulation time significantly.

Hence, another approach needs to be taken, which is to not include the road as an object but rather account for the effect by means of a virtual ground, where the receiving antenna is mirrored, and the response for the indirect path is collected at the mirrored antenna.

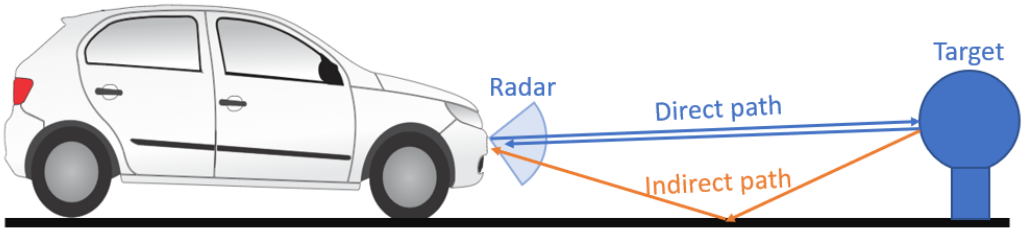

Figure 1.2: Multi-path scenario.

Another problem arises when dealing with objects that have a curved surface. To deal with an object in the simulation tool, first, it should be converted into a mesh of triangular flat facets. This will cause an error in the found hit point between the ray and the object (Fig. 1.3). Therefore, a method will be developed to handle this situation.

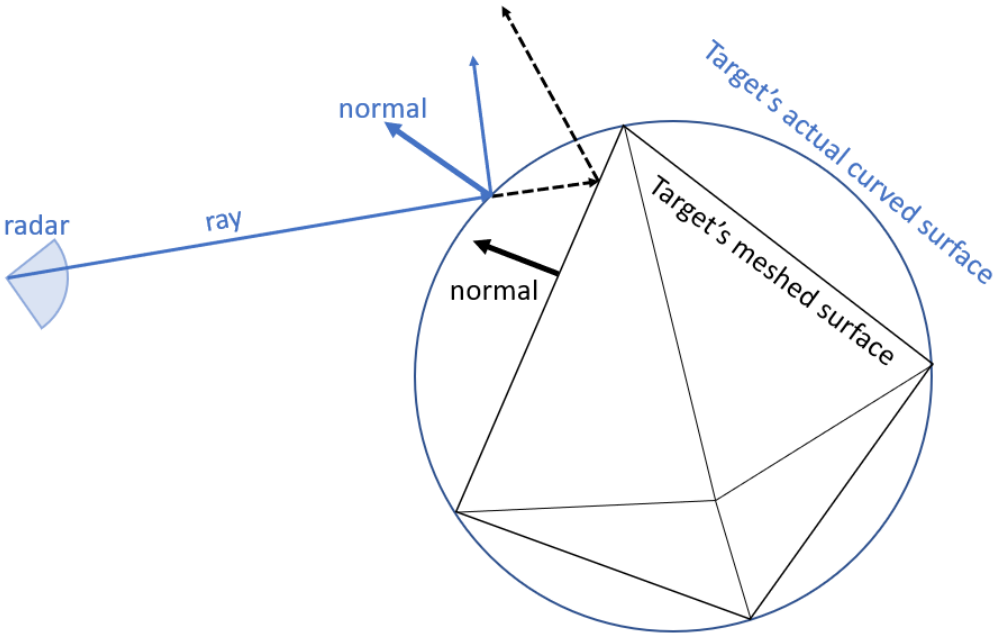

Figure 1.3: Interaction between a ray and a mesh of a curved object.

Using ray-tracing methods is relatively fast, but still not at a real-time speed.

Therefore, a faster approach to scenario simulation can be used, which is to replace objects by their RCS radial pattern. It is proposed in this work to extend the one-dimensional angle-dependent pattern to a 2D angle-range dependent map by simulating the scope of ranges using an actual antenna instead of the far-field pattern. Then, the multi-path effect is applied using the four-path model without including the ground in the simulation.

Lastly, the situation of the installed radar behind the car's fascia is considered. This causes multiple effects, like changing the radiation pattern of the antenna and the ghost targets, which occur when the radar's waves reflect off the internal side of the fascia and return to the receiver, causing a false detection called a ghost target. This effect is studied by simulation.

In this work, the following contributions are made to enable fast and relatively precise simulations to provide relevant data for machine learning:

- Handling of low-fidelity meshing of objects to be simulated
- Significant simulation speed-up representing actual objects by their respective angle-range dependent RCS patterns.
- Ghost target assessment due to bumper and body-in-white reflections.

Chapter 2

Background

2.1 Electromagnetic Fields and Maxwell's Equations

The physics of electromagnetic fields and wave propagation is described by Maxwell's equations. They have differential and integral forms. The differential form is [2] [3]:

$$\nabla \times \vec{E} = -\vec{M}s - \frac{\partial \vec{B}}{\partial t}, \quad \text{(Faraday's Law)}, \tag{2.1}$$

$$\nabla \times \vec{H} = \vec{J} + \frac{\partial \vec{D}}{\partial t} \quad \text{(Ampere's Law)}, \tag{2.2}$$

$$\nabla \cdot \vec{D} = \rho_e \quad \text{(Gauss's Law, electric)}, \tag{2.3}$$

$$\nabla \cdot \vec{B} = \rho_m = 0 \quad \text{(Gauss's Law, magnetic)}, \tag{2.4}$$

where:
$\vec{E} = \vec{E}(\vec{r}, t)$ is the electric field intensity in Volt/m;
$\vec{H} = \vec{H}(\vec{r}, t)$ is the magnetic field intensity in Ampere/m;
$\vec{D} = \vec{D}(\vec{r}, t)$ is electric flux density in As/m^2;
$\vec{B} = \vec{B}(\vec{r}, t)$ is magnetic flux density in Vs/m^2;
$\vec{J} = \vec{J}(\vec{r}, t)$ is the electric surface current density in Ampere/m^2;
$\vec{M} = \vec{M}(\vec{r}, t)$ is the fictitious magnetic current density in Volt/m^2;
$\rho_e(\vec{r}, t)$ is the electric charge density in As/m^3;
$\rho_m(\vec{r}, t)$ is the fictitious magnetic charge density in Vs/m^3.

The current density J and the charge density ρ are related by the equation of continuity:

$$\nabla \cdot \vec{J} = -\frac{\partial \rho}{\partial t}. \tag{2.5}$$

This equation describes the principle of conservation of charge.

The integral form of Maxwell's equations can be obtained by using Stoke's theorem and Green's divergence theorem, and they are given by:

$$\oint_{\partial A} \vec{E} \cdot \vec{dl} = -\iint_A \vec{M} \cdot d\vec{A} - \frac{d}{dt} \iint_A \vec{B} \cdot d\vec{A}, \tag{2.6}$$

$$\oint_{\partial A} \vec{H} \cdot dl = \iint_A \vec{J} \cdot d\vec{A} + \frac{d}{dt} \iint_A \vec{D} \cdot d\vec{A}, \tag{2.7}$$

$$\oiint_{\partial V} \vec{D} \cdot d\vec{A} = \iiint_V \rho_e \cdot dV, \tag{2.8}$$

$$\oiint_{\partial V} \vec{B} \cdot d\vec{A} = \iiint_V \rho_m \cdot dV. \tag{2.9}$$

When dealing with electromagnetic waves of radar, the waves are high-frequency time-harmonic fields, and in this case, the fields are given by:

$$\vec{E}(\vec{r}, t) = \text{Re}[\underline{\vec{E}}(\vec{r})e^{j\omega t}], \tag{2.10}$$

$$\vec{H}(\vec{r}, t) = \text{Re}[\underline{\vec{H}}(\vec{r})e^{j\omega t}], \tag{2.11}$$

$$\vec{D}(\vec{r}, t) = \text{Re}[\underline{\vec{D}}(\vec{r})e^{j\omega t}], \tag{2.12}$$

$$\vec{B}(\vec{r}, t) = \text{Re}[\underline{\vec{B}}(\vec{r})e^{j\omega t}], \tag{2.13}$$

$$\vec{J}(\vec{r}, t) = \text{Re}[\underline{\vec{J}}(\vec{r})e^{j\omega t}], \tag{2.14}$$

and Maxwell's equations become:

$$\nabla \times \underline{\vec{E}}(\vec{r}) = -\underline{\vec{M}}(\vec{r}) - j\omega \underline{\vec{B}}(\vec{r}), \tag{2.15}$$

$$\nabla \times \underline{\vec{H}}(\vec{r}) = \underline{\vec{J}}(\vec{r}) + j\omega \underline{\vec{D}}(\vec{r}), \tag{2.16}$$

$$\nabla \cdot \underline{\vec{D}}(\vec{r}) = \rho_e, \tag{2.17}$$

$$\nabla \cdot \underline{\vec{B}}(\vec{r}) = \rho_m, \tag{2.18}$$

$$\nabla \cdot \underline{\vec{J}}(\vec{r}) = -j\omega\rho. \tag{2.19}$$

2.2 Constitutive Equations

The constitutive equations relate the electric field $\vec{E}$ to the electric flux density $\vec{D}$ depending on the material properties of the medium. And they similarly relate the magnetic field $\vec{H}$ and the magnetic flux density $\vec{B}$. For a linear, homogeneous, and isotropic lossless medium, they are [2]:

$$\vec{D} = \epsilon\vec{E} = \epsilon_0\epsilon_r\vec{E}, \tag{2.20}$$

$$\vec{B} = \mu\vec{H} = \mu_0\mu_r\vec{H}, \tag{2.21}$$

where $\epsilon_0 = 8.854 \times 10^{-12}$ (As/Vm) is the electric permittivity, and $\mu_0 = 4\pi \times 10^{-7}$ (Vs/Am) is the magnetic permeability, both of vacuum. ϵ_r and μ_r are the relative permittivity and permeability of the medium, respectively.

2.3 Boundary Conditions

When traveling EM waves encounter an object with different properties than the surrounding or surface separating two media with different characteristics, which means a discontinuity in the medium, they behave according to the boundary conditions. To derive these equations, the integral form of Maxwell's equations is used [3]. Considering Fig. 2.1 and using the first Maxwell's equation (2.6) assuming the surface magnetic current density $M_s = 0$, it is seen that as Δy goes to zero, the second side becomes zero as well. Therefore, the sum of the tangential electric fields becomes zero, giving us the first boundary condition:

$$\vec{n} \times (\vec{E}_2 - \vec{E}_1) = 0, \tag{2.22}$$

which means that across an interface between two media, the tangential components of the electric field are continuous. By taking the second Maxwell equation (2.7) and assuming that the surface current density $J_s = 0$, the second boundary condition is reached:

$$\vec{n} \times (\vec{H}_2 - \vec{H}_1) = 0, \tag{2.23}$$

which, similarly, indicates that across an interface between two media, the tangential components of the magnetic field are continuous. Now by considering

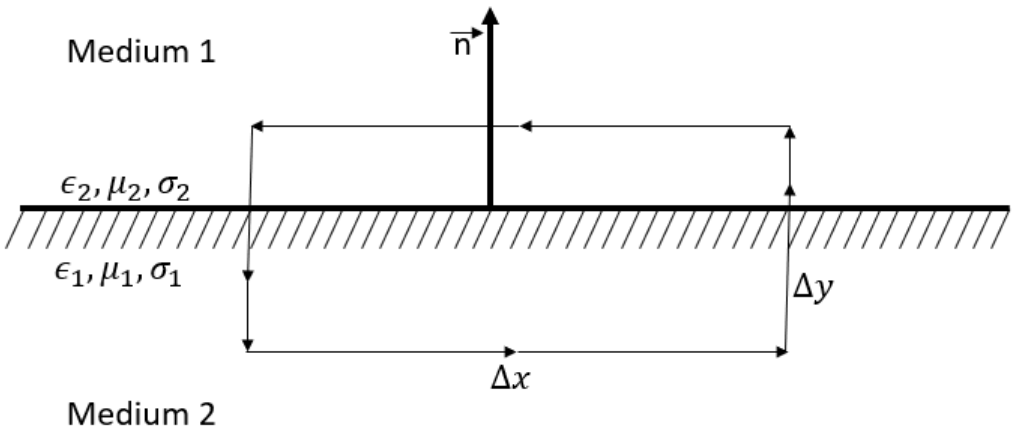

Figure 2.1: A loop around the boundary between two media.

Fig.2.2, taking Δy to zero, and using the third Maxwell's equation (2.8), while assuming the surface charge density is zero at the material interface $\rho_e = 0$, the third boundary condition is found:

$$\vec{n} \cdot (\vec{D}_2 - \vec{D}_1) = 0, \tag{2.24}$$

which states that across an interface between two media, the normal components of the electric flux density are continuous. Similarly, by considering the fourth Maxwell's equation (2.9), and assuming the surface fictitious magnetic charge density at the material interface is zero $\rho_m = 0$, the last boundary condition is described as:

$$\vec{n} \cdot (\vec{B}_2 - \vec{B}_1) = 0, \tag{2.25}$$

which means that across the interface between two media, the normal components of the magnetic flux density are continuous.

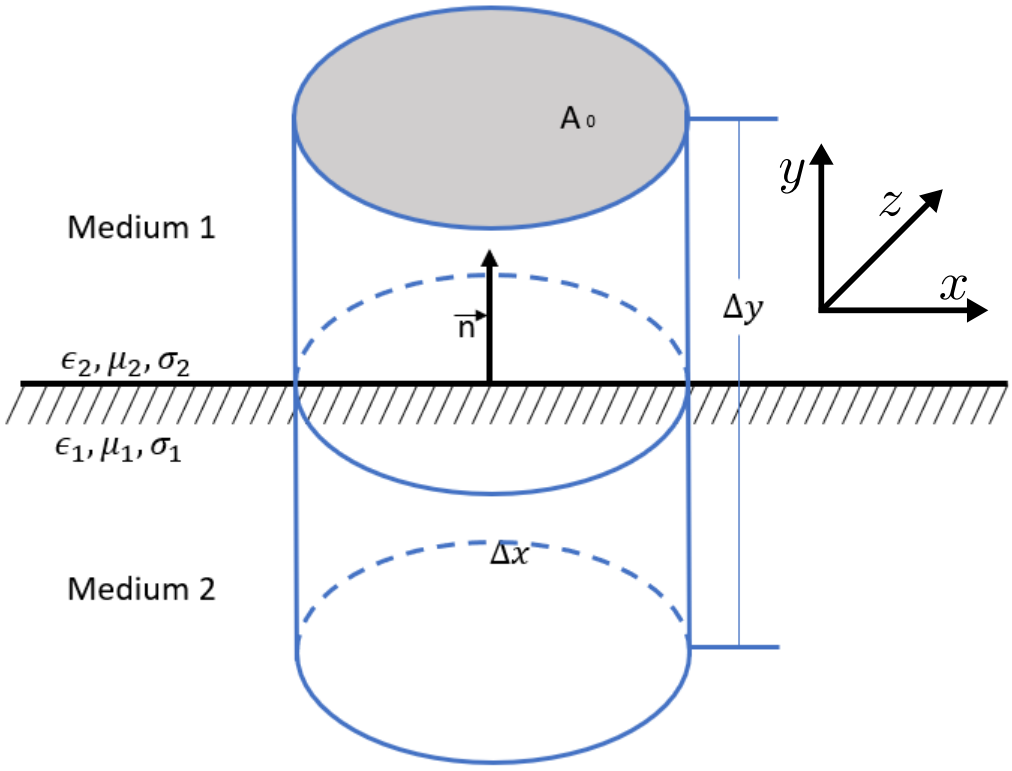

Figure 2.2: A loop around the boundary between two media.

2.3.1 Boundaries Containing Sources

If the boundary contains electric or magnetic sources, the boundary conditions become:

$$\vec{n} \times (\vec{E}_2 - \vec{E}_1) = M_s, \tag{2.26}$$

$$\vec{n} \times (\vec{H}_2 - \vec{H}_1) = J_s, \tag{2.27}$$

$$\vec{n} \cdot (\vec{D}_2 - \vec{D}_1) = q_e, \tag{2.28}$$

$$\vec{n} \cdot (\vec{B}_2 - \vec{B}_1) = q_m, \tag{2.29}$$

where M_s and J_s are the magnetic and electric surface current densities on the boundary, respectively, and q_e and q_m are the electric and magnetic charge densities on the boundary, respectively.

2.4 Reflection and Transmission at Boundaries

When a traveling electromagnetic wave encounters a boundary between two media, a portion of the wave gets reflected by the surface, and a portion transmits through the interface with an angle different than the angle of incidence. To analyze the phenomena, the plane of incidence is introduced, which is the plane containing the source, the hit-point, and the normal to the surface at the hit-point. The EM wave is considered in two polarizations, one where the electric field is perpendicular to the plane of incidence, which is called the perpendicular polarization or the transverse electric (TE) polarization. The second one is where the electric field is in the plane of incidence and is called the parallel polarization or the transverse magnetic (TM) polarization. The equations describing these reflection coefficients are Fresnel's equations.

2.4.1 Perpendicular Polarization (Transverse Electric (TE))

The perpendicular polarization (transverse electric) is depicted in Fig. 2.3. The reflection coefficient, in this case, is given by [3]

$$R_{TE} = \frac{\eta_2 \cos(\theta_i) - \eta_1 \cos(\theta_t)}{\eta_2 \cos(\theta_i) + \eta_1 \cos(\theta_t)}, \tag{2.30}$$

where η_i is the wave impedance and is given by

$$\eta_i = \sqrt{\frac{\mu_i}{\epsilon_i}}, \tag{2.31}$$

where θ_i is the angle of incidence, and θ_t is the angle of transmission, and they are related by Snell's law:

$$\sqrt{\epsilon_1}\sin\theta_i = \sqrt{\epsilon_2}\sin\theta_t. \tag{2.32}$$

The transmission coefficient, in this case, is

$$T_{TE} = \frac{2\eta_2\cos\theta_i}{\eta_2\cos(\theta_i) + \eta_1\cos(\theta_t)} \tag{2.33}$$

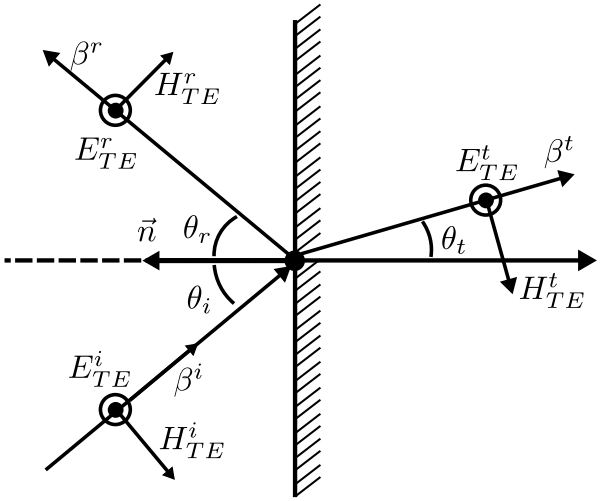

Figure 2.3: Perpendicular polarization.

2.4.2 Parallel Polarization (Transverse Magnetic (TM))

The parallel polarization (transverse magnetic) is shown in Fig. 2.4. In this case, the reflection coefficient is

$$R_{TM} = \frac{\eta_2\cos\theta_t - \eta_1\cos\theta_i}{\eta_2\cos\theta_t + \eta_1\cos\theta_i}, \tag{2.34}$$

and the transmission coefficient is

$$T_{TM} = \frac{2\eta_2\cos\theta_i}{\eta_2\cos\theta_t + \eta_1\cos\theta_i}. \tag{2.35}$$

2.4.3 Plot for Both Polarizations

Fig.2.5 shows the plot of the reflection coefficient for angles between 0 and 90 degrees with a dielectric constant of $\epsilon_r = 4$

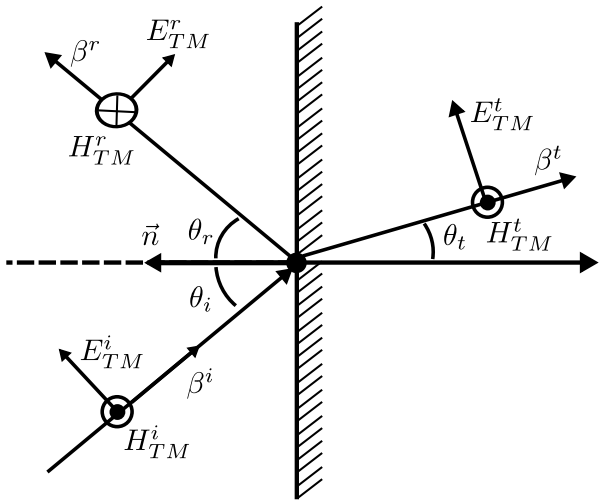

Figure 2.4: Parallel polarization.

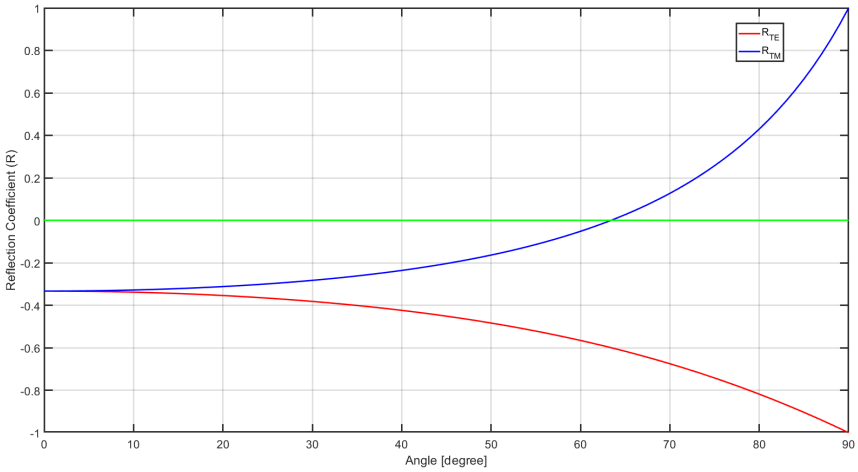

Figure 2.5: Plot of both polarizations for angles between 0 and 90.

2.4.4 The Case of Perfect Electric Conductor (PEC)

In the important case of a perfect electric conductor (PEC), there is the limit $|\epsilon_2| \to \infty$ while μ_2 is finite, and this leads to [4]:

$$\eta_2 = \sqrt{\frac{\mu_2}{\epsilon_2}} \to 0, \quad \theta_2 \to 0, \tag{2.36}$$

and thus, the equation

$$R_{TE} \to -1, \qquad R_{TM} \to -1. \tag{2.37}$$

2.5 Power Transport

When an electromagnetic wave propagates through space, it carries energy with it. The instantaneous power carried is [3]

$$\vec{S} = \vec{E} \times \vec{H}, \tag{2.38}$$

where $\vec{S}$ is known as the Poynting vector with units of power density ($Watt/m^2$). The power exiting a volume V bounded by a surface A is

$$P = \oiint_{\partial V} (\vec{E} \times \vec{H}) \cdot d\vec{A} = \oiint_{\partial V} \vec{S} \cdot d\vec{A}. \tag{2.39}$$

2.6 The Wave Equation

To solve an electromagnetic problem, Maxwell's equations should be solved, which are coupled. As a result, to uncouple them, second-order differential equations are reached, that are called the wave equations for each of $\vec{E}$ and $\vec{B}$.

2.6.1 Time-Varying Electromagnetic Fields

To derive the wave equations for electromagnetic fields [3], first, the first two Maxwell's equations are restated

$$\nabla \times \vec{E} = -\vec{M} - \frac{\partial \vec{B}}{\partial t}, \quad \text{(Faraday's Law)}, \tag{2.40}$$

$$\nabla \times \vec{H} = \vec{J} + \sigma \vec{E} + \frac{\partial \vec{D}}{\partial t} \quad \text{(Ampere's Law)}. \tag{2.41}$$

The curl of both equations is taken, and the derivation is exchanged with respect to time with the curl on the right side to get

$$\nabla \times \nabla \times \vec{E} = -\nabla \times \vec{M} - \mu \frac{\partial}{\partial t}(\nabla \times \vec{H}), \tag{2.42}$$

$$\nabla \times \nabla \times \vec{H} = \nabla \times \vec{J} + \sigma \nabla \times \vec{E} + \epsilon \frac{\partial}{\partial t}(\nabla \times \vec{E}), \tag{2.43}$$

and by substituting 2.41 into 2.42 and using the vector equation

$$\nabla \times \nabla \times \vec{F} = \nabla(\nabla \cdot \vec{F}) - \nabla^2 \vec{F}, \tag{2.44}$$

the next equation results

$$\nabla(\nabla \cdot \vec{E}) - \nabla^2 \vec{E} = -\nabla \times \vec{M} - \mu \frac{\partial \vec{J}}{\partial t} - \mu\sigma \frac{\partial \vec{E}}{\partial t} - \mu\epsilon \frac{\partial^2 \vec{E}}{\partial t^2}, \tag{2.45}$$

and by substituting the third of Maxwell's equation, which is

$$\nabla \cdot \vec{E} = \frac{q_e}{\epsilon}, \tag{2.46}$$

the following equation is reached

$$\nabla^2 \vec{E} = \nabla \times \vec{M} + \mu \frac{\partial \vec{J}}{\partial t} + \frac{1}{\epsilon} \nabla q_e + \mu\sigma \frac{\partial \vec{E}}{\partial t} + \mu\epsilon \frac{\partial^2 \vec{E}}{\partial t^2}, \tag{2.47}$$

and by a similar process for the magnetic fields, the following formula is reached

$$\nabla^2 \vec{H} = -\nabla \times \vec{J} + \sigma \vec{M} + \frac{1}{\mu} \nabla \cdot q_m + \epsilon \frac{\partial \vec{M}}{\partial t} + \mu\sigma \frac{\partial \vec{H}}{\partial t} + \mu\epsilon \frac{\partial^2 \vec{H}}{\partial t^2}, \tag{2.48}$$

and these are called the vector wave equations for each of the electric field (E) and the magnetic field (H). These equations are simplified when considering source-free space as follows

$$\nabla^2 \vec{E} = \mu\sigma \frac{\partial \vec{E}}{\partial t} + \mu\epsilon \frac{\partial^2 \vec{E}}{\partial t^2}, \tag{2.49}$$

$$\nabla^2 \vec{H} = \mu\sigma \frac{\partial \vec{H}}{\partial t} + \mu\epsilon \frac{\partial^2 \vec{H}}{\partial t^2}, \tag{2.50}$$

and when considering lossless material ($\sigma = 0$), the simplest form results as

$$\nabla^2 \vec{E} = \mu\epsilon \frac{\partial^2 \vec{E}}{\partial t^2}, \tag{2.51}$$

$$\nabla^2 \vec{H} = \mu\epsilon \frac{\partial^2 \vec{H}}{\partial t^2}. \tag{2.52}$$

2.6.2 Time-Harmonic Electromagnetic Fields

Time variation of the form $e^{j\omega t}$ is considered, and by a similar process as the previous section, the wave equations for the time-harmonic fields E and H are reached. Instead, the derivation with respect to time will be replaced with appropriate terms as follows [3]

$$\frac{\partial}{\partial t} \rightarrow j\omega, \tag{2.53}$$

$$\frac{\partial^2}{\partial t^2} \rightarrow (j\omega)^2 = -\omega^2, \tag{2.54}$$

and the instantaneous quantities are replaced by the complex equivalents, which yield the equations

$$\nabla^2 \underline{\vec{E}}(\vec{r}) = \nabla \times \underline{\vec{M}}(\vec{r}) + j\omega\mu\underline{\vec{J}}(\vec{r}) + \frac{1}{\epsilon}\nabla q_e + j\omega\mu\sigma\underline{\vec{E}}(\vec{r}) - \omega^2\mu\epsilon\underline{\vec{E}}(\vec{r}), \tag{2.55}$$

$$\nabla^2 \underline{\vec{H}}(\vec{r}) = -\nabla \times \underline{\vec{J}}(\vec{r}) + \sigma\underline{\vec{M}}(\vec{r}) + j\omega\epsilon\underline{\vec{M}}(\vec{r}) + \frac{1}{\mu}\nabla q_m + j\omega\mu\sigma\underline{\vec{H}}(\vec{r}) - \omega^2\mu\epsilon\underline{\vec{H}}(\vec{r}). \tag{2.56}$$

When considering a source-free region, the following formula arises

$$\nabla^2 \underline{\vec{E}} = +j\omega\mu\sigma\underline{\vec{E}} - \omega^2\mu\epsilon\underline{\vec{E}} = \gamma^2\underline{\vec{E}}, \tag{2.57}$$

$$\nabla^2 \underline{\vec{H}} = -j\omega\mu\sigma\underline{\vec{H}} - \omega^2\mu\epsilon\underline{\vec{H}} = \gamma^2\underline{\vec{H}}, \tag{2.58}$$

where

$$\gamma^2 = j\omega\mu\sigma - \omega^2\mu\epsilon = j\omega\mu(\sigma + j\omega\epsilon), \tag{2.59}$$

$$\gamma = \alpha + j\beta = \text{propagation constant}, \tag{2.60}$$

$$\alpha = \text{attenuation constant}, \tag{2.61}$$

$$\beta = k = \text{phase constant}, \tag{2.62}$$

$$\beta^2 = \omega^2\mu\epsilon. \tag{2.63}$$

Finally, in a lossless medium ($\sigma = 0$), the following is reached

$$\nabla^2 \underline{\vec{E}} = -\omega^2\mu\epsilon\underline{\vec{E}} = -\beta^2\underline{\vec{E}}, \tag{2.64}$$

$$\nabla^2 \underline{\vec{H}} = -\omega^2\mu\epsilon\underline{\vec{H}} = -\beta^2\underline{\vec{H}}. \tag{2.65}$$

2.6.3 Solution to the Wave Equation

There are several methods to solve the electromagnetic wave equation. Here, the method *separation of variables* is chosen with the time-harmonic quantities [3].

2.6.3.1 Cartesian Coordinate System

In this case, the vector Helmholtz wave equation can be converted to three scalar wave equations (scalar Helmholtz equations). First the case of source free and lossless medium

2.6.3.1.1 Source Free and Lossless medium A solution for $\vec{E}$ will be obtained first, then the solution for $\vec{H}$ can be obtained by replacing the quantities in the solution equations. In Cartesian coordinates, the solution for $\vec{E}$ is of the form

$$\vec{E}(x,y,z) = \vec{e}_x E_x(x,y,z) + \vec{e}_y E_y(x,y,z) + \vec{e}_z E_z(x,y,z). \tag{2.66}$$

Substituting (2.66) into the wave equation gives

$$\nabla^2\vec{E} + \beta^2\vec{E} = \nabla^2(\vec{e}_x E_x + \vec{e}_y E_y + \vec{e}_z E_z) + \beta^2(\vec{e}_x E_x + \vec{e}_y E_y + \vec{e}_z E_z) = 0, \tag{2.67}$$

and by considering the equation

$$\nabla^2(\vec{e}_x E_x + \vec{e}_y E_y + \vec{e}_z E_z) = \vec{e}_x\nabla^2 E_x + \vec{e}_y\nabla^2 E_y + \vec{e}_z\nabla^2 E_z \tag{2.68}$$

the equation (2.67) can be written in terms of three scalar wave equations

$$\nabla^2 E_x(x,y,z) + \beta^2 E_x(x,y,z) = 0 \tag{2.69}$$
$$\nabla^2 E_y(x,y,z) + \beta^2 E_y(x,y,z) = 0 \tag{2.70}$$
$$\nabla^2 E_z(x,y,z) + \beta^2 E_z(x,y,z) = 0 \tag{2.71}$$

and since the three equations are of the same form, solution to one of them leads easily to the others. Therefore, the first one (along x axis) is expanded to

$$\nabla^2 E_x + \beta^2 E_x = \frac{\partial^2 E_x}{\partial x^2} + \frac{\partial^2 E_x}{\partial y^2} + \frac{\partial^2 E_x}{\partial z^2} + \beta^2 E_x = 0. \tag{2.72}$$

To solve this, it is assumed that $E_x(x,y,z)$ can be written, as suggested by the method of *separation of variables*, in the form of

$$E_x(x,y,z) = f(x)g(y)h(z), \tag{2.73}$$

and by substitution in (2.72), the following is arrived at

$$gh\frac{\partial^2 f}{\partial x^2} + fh\frac{\partial^2 g}{\partial y^2} + fg\frac{\partial^2 h}{\partial z^2} + \beta^2 fgh = 0, \tag{2.74}$$

and since each term is dependent on one variable, the partial derivative can be exchanged with ordinary ones. Doing that will lead to the equation

$$\frac{1}{f}\frac{d^2f}{dx^2} + \frac{1}{g}\frac{d^2g}{dy^2} + \frac{1}{h}\frac{d^2h}{dz^2} = -\beta^2. \tag{2.75}$$

Each of the terms is dependent on one variable, and the sum is equal to a constant; hence each one should be equal to a constant, so the following results

$$\frac{1}{f}\frac{d^2f}{dx^2} = -\beta_x^2 \Rightarrow \frac{d^2f}{dx^2} = -\beta_x^2 f, \tag{2.76}$$

$$\frac{1}{g}\frac{d^2g}{dy^2} = -\beta_y^2 \Rightarrow \frac{d^2g}{dy^2} = -\beta_y^2 g, \tag{2.77}$$

$$\frac{1}{h}\frac{d^2h}{dz^2} = -\beta_z^2 \Rightarrow \frac{d^2h}{dz^2} = -\beta_z^2 h, \tag{2.78}$$

$$\beta_x^2 + \beta_y^2 + \beta_z^2 = \beta^2, \tag{2.79}$$

where (2.79) is the constraint equation, and $\beta_x, \beta_y, \beta_z$ are the wave constants in x,y, and z, respectively, which will be specified according to the boundary conditions. The solution to each of the previous equations can be in several forms, like

$$f_1(x) = Ae^{-j\beta_x x} + Be^{+j\beta_x x}, \tag{2.80}$$

or

$$f_2(x) = C\cos(\beta_x x) + D\sin(\beta_x x), \tag{2.81}$$

where the first solution in the form of exponentials is a traveling wave, and the second one, in terms of cosines and sines, represents *standing waves*. Various wave types representing solutions to the wave equations are listed in table 2.1

One of these forms should be chosen for each axis depending on the boundary conditions and the problem. For instance, for a rectangular wave guide along the z-axis, the solution is

$$\begin{aligned} E_x(x,y,z) =& [C_1\cos(\beta_x x) + D_1\sin(\beta_x x)] \cdot [C_2\cos(\beta_y y) + D_2\sin(\beta_y y)] \\ & \cdot [A_3 e^{-j\beta_z z} + B_3 e^{+j\beta_z z}]. \end{aligned} \tag{2.82}$$

For the instantaneous form of the wave in the +z direction (the exponential with $-j\omega t$), it is multiplied by $e^{j\omega t}$ and the real part is taken as in

$$\begin{aligned} \mathcal{E}_x(x,y,z,t)^+ &= \text{Re}[E_x(x,y,z)^+ e^{j\omega t}] \\ &= \text{Re}\{[C_1\cos(\beta_x x) + D_1\sin(\beta_x x)] \cdot [C_2\cos(\beta_y y) + D_2\sin(\beta_y y)] \\ &\cdot [A_3 e^{j(\omega t - \beta_z z}]\}. \end{aligned} \tag{2.83}$$

Table 2.1: Several possible wave functions as solutions to the wave equation in Cartesian coordinates.

Wave type	Wave function
Traveling waves	$e^{-j\beta x}$ for +x travel $e^{+j\beta x}$ for -x travel
Standing waves	$\cos(\beta x)$ for $\pm x$ $\sin(\beta x)$ for $\pm x$
Evanescent waves	$e^{-\alpha x}$ for +x $e^{+\alpha x}$ for -x
Attenuating traveling waves	$e^{-\gamma x} = e^{-\alpha x}e^{-j\beta x}$ for +x travel $e^{+\gamma x} = e^{+\alpha x}e^{+j\beta x}$ for - x travel
Attenuating standing waves	$\cos(\gamma x) = \cos(\alpha x)\cosh(\beta x)$ $-j\sin(\alpha x)\sinh(\beta x)$ for $\pm\, x$ $\sin(\gamma x) = \sin(\alpha x)\cosh(\beta x)$ $+j\cos(\alpha x)\sinh(\beta x)$ for $\pm\, x$

And if the constants are real, the following results

$$\mathcal{E}_x(x,y,z,t)^+ = [C_1\cos(\beta_x x) + D_1\sin(\beta x)]\cdot[C_2\cos(\beta_y y) + D_2\sin(\beta_y y)] \cdot [A_3\cos(\omega t - \beta_z z)]. \tag{2.84}$$

For $x = 0, y = 0$, and setting the constants to 1, the function $F(z,t) = cos(\omega t - \beta z)$ is plotted for three different times as shown in Fig.2.6. To follow a point z_p across time, the term in the last cosine is kept constant, as in

$$\omega t - \beta_z z_p = C_0 = \text{constant}. \tag{2.85}$$

The three circles in Fig.2.6 show the progression of one point z_p across time (here, three different times). By differentiating 2.85 with respect to t, the next equation arises

$$\omega - \beta_z\frac{dz_p}{dt} = 0 \Rightarrow \frac{dz_p}{dt} = \nu_p = +\frac{\omega}{\beta_z}, \tag{2.86}$$

where ν is called "the phase velocity," and the point z_p is called "the equiphase" point.

2.6.3.1.2 Source-Free and Lossy Medium When a source-free and lossy medium is assumed, the wave solution is given by the form [3]

$$\vec{E}(x,y,z) = \vec{e}_x E_x(x,y,z) + \vec{e}_y E_y(x,y,z) + \vec{e}_z E_z(x,y,z). \tag{2.87}$$

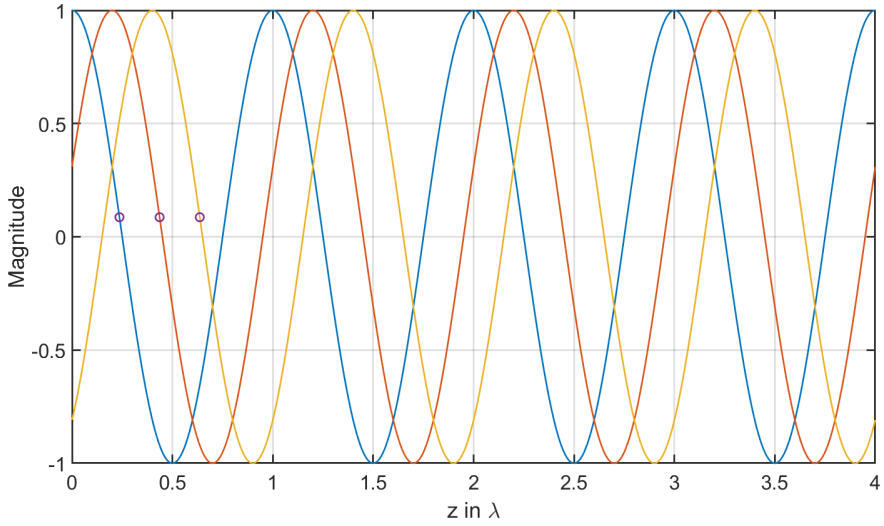

Figure 2.6: Amplitude in terms of the dimension z in λ for three time points.

and the wave equation to solve is, in this case

$$\nabla^2\vec{E} - \gamma^2\vec{E} = \nabla^2(\vec{e}_x E_x + \vec{e}_y E_y + \vec{e}_z E_z) + \gamma^2(\vec{e}_x E_x + \vec{e}_y E_y + \vec{e}_z E_z) = 0, \quad (2.88)$$

which is converted to three wave equations for three coordinates as

$$\nabla^2 E_x(x,y,z) - \gamma^2 E_x(x,y,z) = 0, \quad (2.89)$$
$$\nabla^2 E_y(x,y,z) - \gamma^2 E_y(x,y,z) = 0, \quad (2.90)$$
$$\nabla^2 E_z(x,y,z) - \gamma^2 E_z(x,y,z) = 0, \quad (2.91)$$
$$\gamma^2 = j\omega\mu(\sigma + j\omega\epsilon), \quad (2.92)$$

and for positive values for σ, it results in

$$\gamma = \pm\sqrt{j\omega\mu(\sigma + j\omega\epsilon)} = \pm(\alpha + j\beta), \quad (2.93)$$

where

$$\gamma = \text{propagation constant}, \quad (2.94)$$
$$\alpha = \text{attenuation constant(neper/m)}, \quad (2.95)$$
$$\beta = k = \text{phase constant (rad/m)}. \quad (2.96)$$

To solve the wave equation in this case, the method of separation of variables is used, as for the lossless case, so it is assumed that

$$E_x(x,y,z) = f(x)g(y)h(z), \quad (2.97)$$

where each of these functions has the form of either

$$f_1(x) = A_1 e^{-\gamma_x x} + \beta_1 e^{+\gamma_x x}, \tag{2.98}$$

or

$$f_2(x) = C_1 \cosh(\gamma_x x) + D_1 \sinh(\gamma_x x), \tag{2.99}$$

where there is the equation

$$\gamma^2 = \gamma_x^2 + \gamma_y^2 + \gamma_z^2. \tag{2.100}$$

By choosing to work with the first form (traveling wave in the positive direction $Ae^{\gamma x}$) and by substituting γ, the solution is

$$f(x) = A_1 e^{-\gamma x} = A_1 e^{-\alpha x} e^{-\beta_x x}, \tag{2.101}$$

$$\text{or } f(x) = A_1 e^{-\gamma x} = A_1 e^{+\alpha x} e^{+\beta_x x}. \tag{2.102}$$

The first equation represents a wave that travels in +z direction and decays in the same direction, while the second one represents a wave traveling in -z direction and decays in that direction as well. The instantaneous quantities can be found, like in the previous case, by multiplying with the time variation term $e^{j\omega t}$ and taking the real part of it as

$$\vec{E}(x, y, z, t) = \text{Re}[(\underline{\vec{E}}(x, y, z) e^{j\omega t}]. \tag{2.103}$$

2.6.3.2 Cylindrical Coordinates with Lossless and Source Free Medium

When solving electromagnetic problems with objects of cylindrical shape, it is better to handle them using cylindrical coordinates. The cylindrical coordinate system is shown in Fig. 2.7, which is composed of the coordinates (ρ, ϕ, z), and the unit vectors $(\vec{e}_\rho, \vec{e}_\phi, \vec{e}_z)$. In this case, a general solution is assumed, similar to what is done for the Cartesian coordinates of the form [3]

$$\vec{E}(\rho, \phi, z) = \vec{e}_\rho \vec{E}_\rho(\rho, \phi, z) + \vec{e}_\phi \vec{E}_\phi(\rho, \phi, z) + \vec{e}_z \vec{E}_z(\rho, \phi, z). \tag{2.104}$$

Substituting this equation into the wave equation for lossless and source free medium results in

$$\nabla^2(\vec{e}_\rho E_\rho + \vec{e}_\phi E_\phi + \vec{e}_z E_z) = \beta^2(\vec{e}_\rho E_\rho + \vec{e}_\phi E_\phi + \vec{e}_z E_z), \tag{2.105}$$

but in this case, there are no scalar equations for the first two coordinates, as previously done, because

$$\nabla^2(\vec{e}_\rho E_\rho) \neq \vec{e}_\rho \nabla^2 E_\rho, \tag{2.106}$$

$$\nabla^2(\vec{e}_\phi E_\phi) \neq \vec{e}_\phi \nabla^2 E_\phi. \tag{2.107}$$

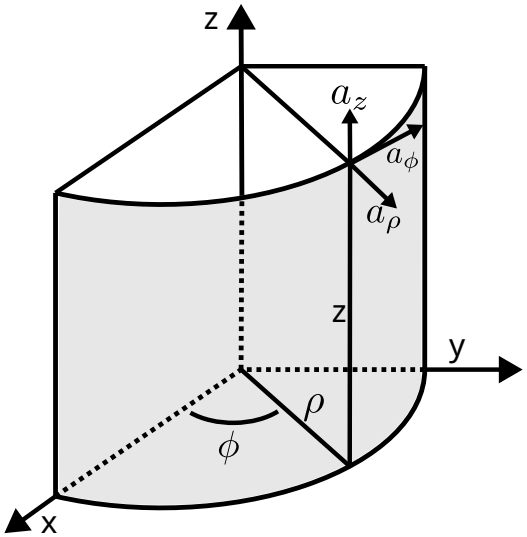

Figure 2.7: Cylindrical coordinate system.

However, the condition is satisfied only for z as

$$\nabla^2(\vec{e}_z E_z) = \vec{e}_z \nabla^2 E_z. \tag{2.108}$$

Therefore, there is the scalar equation

$$\nabla^2 E_z + \beta^2 E_z = 0. \tag{2.109}$$

The reason for the previous non-equality for the first two coordinates is that the unit vectors $\vec{e}_\rho$ and $\vec{e}_\phi$ are not constants, but rather changing with each point (ρ, ϕ, z), unlike the vector $\vec{e}_z$, which is constant for all points. Now, starting with the general wave equation

$$\nabla^2 \vec{E} = -\beta^2 \vec{E}, \tag{2.110}$$

and using the vector identity

$$\nabla \times \nabla \times \vec{F} = \nabla(\nabla \cdot \vec{F}) - \nabla^2 \vec{F}, \tag{2.111}$$

it can be written as

$$\nabla^2 \vec{E} = \nabla(\nabla \cdot \vec{E}) - \nabla \times \nabla \times \vec{E}, \tag{2.112}$$

and by substituting in the wave equation, the following is given

$$\nabla(\nabla \cdot \vec{E}) - \nabla \times \vec{E} = -\beta^2 \vec{E}. \tag{2.113}$$

Assuming the general solution form of $\vec{E}$ results in the following three scalar partial differential equations

$$\nabla^2 E_\rho + (-\frac{E_\rho}{\rho^2} - \frac{2}{\rho^2}\frac{\partial E_\phi}{\partial \phi}) = -\beta^2 E_\rho, \tag{2.114}$$

$$\nabla^2 E_\phi + (-\frac{E_\phi}{\rho^2} + \frac{2}{\rho^2}\frac{\partial E_\rho}{\partial \phi}) = -\beta^2 E_\phi, \tag{2.115}$$

$$\nabla^2 E_z = -\beta^2 E_z, \tag{2.116}$$

where ∇^2 is the Laplacian operator, and for a scalar quantity ψ in cylindrical coordinates, it is give by

$$\nabla^2 \psi(\rho, \phi, z) = \frac{\partial^2 \psi}{\partial \rho^2} + \frac{1}{\rho}\frac{\partial \psi}{\partial \rho} + \frac{1}{\rho^2}\frac{\partial^2 \psi}{\partial \phi^2} + \frac{\partial^2 \psi}{\partial z^2}, \tag{2.117}$$

and by substitution in 2.116, it gives

$$\frac{\partial^2 \psi}{\partial \rho^2} + \frac{1}{\rho}\frac{\partial \psi}{\partial \rho} + \frac{1}{\rho^2}\frac{\partial^2 \psi}{\partial \phi^2} + \frac{\partial^2 \psi}{\partial z^2} = \beta^2 \psi. \tag{2.118}$$

By assuming a separable solution of the form

$$\psi(\rho, \phi, z) = f(\rho)g(\phi)h(z) \tag{2.119}$$

the following equation is reached at

$$gh\frac{\partial^2 f}{\partial \rho^2} + gh\frac{1}{\rho}\frac{\partial f}{\partial \rho} + fh\frac{1}{\rho^2}\frac{\partial^2 g}{\partial \phi^2} + fg\frac{\partial^2 h}{\partial z^2} = -\beta^2 fgh, \tag{2.120}$$

and by dividing both sides by fgh, the following arises

$$\frac{1}{f}\frac{d^2 f}{d\rho^2} + \frac{1}{f\rho}\frac{df}{d\rho} + \frac{1}{g\rho^2}\frac{d^2 g}{d\phi^2} + \frac{1}{h}\frac{d^2 h}{dz^2} = -\beta^2. \tag{2.121}$$

By realizing that the last term is dependent only on z, the next equation can be written

$$\frac{1}{h}\frac{d^2 h}{dz^2} = -\beta_z^2 \Rightarrow \frac{d^2 h}{dz^2 = -\beta_z^2 h}, \tag{2.122}$$

and by substituting it in 2.121 and multiplying both sides by ρ^2, the following is obtained

$$\frac{\rho^2}{f}\frac{d^2 f}{d\rho^2} + \frac{\rho}{f}\frac{df}{d\rho} + \frac{1}{g}\frac{d^2 g}{d\phi^2} + (\beta^2 - \beta_z^2)\rho^2 = 0. \tag{2.123}$$

By realizing that the third term is only dependent on ϕ, the following is found

$$\frac{1}{g}\frac{d^2 g}{d\phi^2} = -m^2 \Rightarrow \frac{d^2}{d\phi^2} = -m^2 g, \tag{2.124}$$

and by letting

$$\beta^2 - \beta_z^= \beta_{rho}^2 \Rightarrow \beta_{rho}^2 + \beta_z^2 = \beta^2, \tag{2.125}$$

the next equation is reached

$$\rho^2 \frac{d^2 f}{d\rho^2} + \rho \frac{df}{d\rho} + [(\beta_\rho \rho)^2 - m^2] f = 0, \tag{2.126}$$

which is known as the Bessel differential equation. To summarize, the separable wave equation 2.118 reduces to

$$\boxed{\rho^2 \frac{d^2 f}{d\rho^2} + \rho \frac{df}{d\rho} + [(\beta_\rho \rho)^2 - m^2] f = 0} \tag{2.127}$$

$$\boxed{\frac{d^2 g}{d\phi^2} = -m^2 g} \tag{2.128}$$

$$\boxed{\frac{d^2 h}{dz^2} = -\beta_z^2 h} \tag{2.129}$$

with the constraint

$$\boxed{\beta_\rho^2 + \beta_z^2 = \beta^2} \tag{2.130}$$

These three equations take the following forms, respectively

$$f_1(\rho) = A_1 J_m(\beta_\rho \rho) + B_1 Y_m(\beta_\rho \rho), \tag{2.131}$$

or

$$f_2(\rho) = C_1 H_m^{(1)}(\beta_\rho \rho) + D_1 H_m^{(2)}(\beta_\rho \rho), \tag{2.132}$$

and

$$g_1(\phi) = A_2 e^{-jm\phi} + B_2 e^{+jm\phi}, \tag{2.133}$$

or

$$g_2(\phi) = C_2 \cos(m\phi) + D_2 \sin(m\phi), \tag{2.134}$$

and

$$h_1(z) = A_3 e^{-j\beta_z z} + B_3 e^{+j\beta_z z}, \tag{2.135}$$

or

$$h_2(z) = C_3 \cos(\beta_z z) + D_3 \sin(\beta_z z), \tag{2.136}$$

where J_m is the Bessel function of the first kind, and Y_m is the Bessel function of the second kind, while $H_m^{(1)}$ and $H_m^{(2)}$ are the Hankel functions of the first and

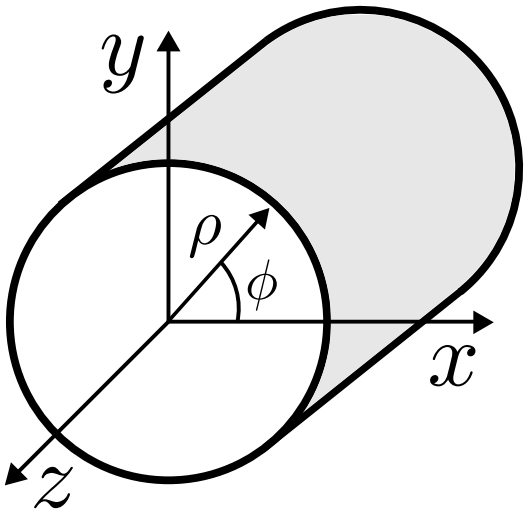

Figure 2.8: Cylindrical waveguide.

second type, respectively. The chosen form is dependent on the problem at hand. For instance, for a cylindrical waveguide (Fig. 2.8), the solution takes the form

$$\begin{aligned}\psi(\rho,\phi,z) &= f(\rho)g(\phi)h(z) \\ &= [A_1 J_m(\beta_\rho \rho) + B_1 Y_m(\beta_\rho \rho)] \\ &\cdot [C_2 \cos(m\phi) + D_2 \sin(m\phi)] \cdot [A_3 e^{-j\beta_z z} + B_3 e^{+j\beta_z z}].\end{aligned} \tag{2.137}$$

These forms are chosen for the following reasons

- For $f(\rho)$, Bessel functions represent standing waves along ρ direction
- For $g(\phi)$, cosine and sine functions represent periodic waves around the axis along ϕ direction
- For $h(z)$, exponentials represent traveling waves along the axis of the waveguide.

2.7 Auxiliary Vector Potentials

When solving electromagnetic problems, the first way is to solve directly for $\vec{E}$ and $\vec{H}$ using Maxwell's equations or the wave equations. The other way, according to [3], is to use the vector potentials $\vec{A}$ and $\vec{F}$ as a first step, then calculating $\vec{E}$ and $\vec{H}$ as a second step as shown in Fig. 2.9. Although this is a two step process, it is often simpler than the direct way. For time-harmonic fields,

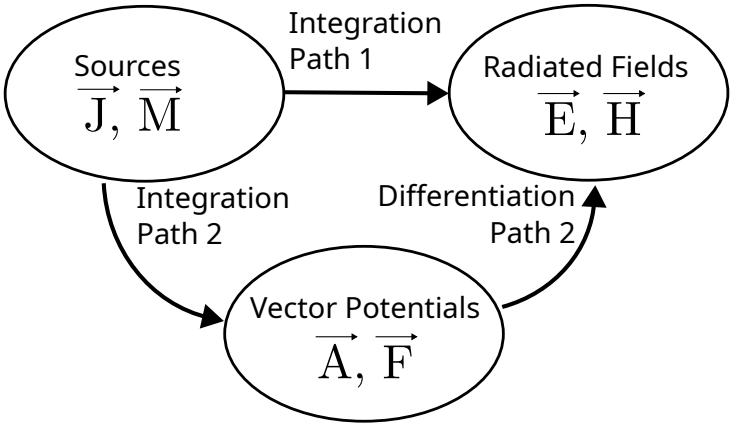

Figure 2.9: Two paths to solve for radiated fields E and H.

the first method is to solve using Maxwell's equations, which are [3]

$$\nabla \times \underline{\vec{E}} = -\underline{\vec{M}} - j\omega\mu\underline{\vec{H}}, \tag{2.138}$$

$$\nabla \times \underline{\vec{H}} = \underline{\vec{J}} + j\omega\epsilon\underline{\vec{E}}, \tag{2.139}$$

$$\nabla \cdot \underline{\vec{E}} = \frac{q_e}{\epsilon}, \tag{2.140}$$

$$\nabla \cdot \underline{\vec{H}} = \frac{q_m}{\mu}, \tag{2.141}$$

or the vector wave equations

$$\nabla^2\underline{\vec{E}} + \beta^2\underline{\vec{E}} = \nabla \times \underline{\vec{M}} + j\omega\mu\underline{\vec{J}} + \frac{1}{\epsilon}\nabla q_e, \tag{2.142}$$

$$\nabla^2\underline{\vec{H}} + \beta^2\underline{\vec{H}} = -\nabla \times \underline{\vec{J}} + j\omega\epsilon\underline{\vec{M}} + \frac{1}{\mu}\nabla q_m. \tag{2.143}$$

2.7.1 The Vector Potential $\vec{A}$

If the fields are in a region without sources, considering the equation $\nabla \cdot \vec{B} = 0$, and the vector identity [3]

$$\nabla \cdot (\nabla \times \vec{A}) = 0, \tag{2.144}$$

where $\vec{A}$ is a vector potential, which means that B can be written in terms of the curl of a vector field $\vec{A}$. Therefore, the following can be written

$$\vec{B} = \mu\vec{H} = \nabla \times \vec{A}, \tag{2.145}$$

and thus

$$\vec{H} = \frac{1}{\mu}\nabla \times \vec{A}. \tag{2.146}$$

Substituting this into the first of the harmonic Maxwell's equations results in

$$\nabla \times \underline{\vec{E}} = -j\omega\mu\underline{\vec{H}} = -j\omega\nabla \times \underline{\vec{A}}, \tag{2.147}$$

$$\Rightarrow \quad \nabla \times [\underline{\vec{E}} + j\omega\underline{\vec{A}}] = 0, \tag{2.148}$$

and by using the vector identity

$$\nabla \times (-\nabla\phi_e) = 0, \tag{2.149}$$

which leads to the conclusion that

$$\underline{\vec{E}} + j\omega\underline{\vec{A}} = -\nabla\phi_e, \tag{2.150}$$

$$\Rightarrow \boxed{\underline{\vec{E}} = -\nabla\phi_e - j\omega\underline{\vec{A}}} \tag{2.151}$$

where ϕ_e is a scalar electric potential. By utilizing the vector identity

$$\nabla \times \nabla \times \underline{\vec{A}} = \nabla(\nabla \cdot \underline{\vec{A}}) - \nabla^2\underline{\vec{A}}, \tag{2.152}$$

and taking the curl of both sides of (2.145), considering homogeneous region, it can be found that

$$\mu\nabla \times \underline{\vec{H}} = \nabla(\nabla \cdot \underline{\vec{A}}) - \nabla^2\underline{\vec{A}}. \tag{2.153}$$

By comparison with the second Maxwell's equation, it can be reached to

$$\mu\underline{\vec{J}} + j\omega\mu\epsilon\underline{\vec{E}} = \nabla(\nabla \cdot \underline{\vec{A}}) - \nabla^2\underline{\vec{A}}, \tag{2.154}$$

and substituting (2.151) leads to

$$\nabla^2\underline{\vec{A}} + \beta^2\underline{\vec{A}} = -\mu J + \nabla(\nabla \cdot \underline{\vec{A}}) + \nabla(j\omega\mu\epsilon\phi_e) = -\mu\underline{\vec{J}} + \nabla(\nabla\underline{\vec{A}} + j\omega\mu\epsilon\phi_e), \tag{2.155}$$

where $\beta^2 = \omega^2\mu\epsilon$. Now, since the divergence of $\vec{A}$ is independent of its curl, the divergence can be defined, to simplify (2.155), as

$$\nabla \cdot \underline{\vec{A}} = -j\omega\epsilon\mu\phi_e, \tag{2.156}$$

$$\Rightarrow \boxed{\phi_e = -\frac{1}{j\omega\mu\epsilon}\nabla \cdot \underline{\vec{A}}} \tag{2.157}$$

which leads (2.155) to

$$\nabla^2\underline{\vec{A}} + \beta^2\underline{\vec{A}} = -\mu\underline{\vec{J}}, \tag{2.158}$$

which is a wave equation and can be solved using the same techniques presented for $\vec{E}$. At last, the next equation is reached

$$\underline{\vec{E}} = -j\omega\underline{\vec{A}} - \nabla\phi_e, \tag{2.159}$$

$$\Rightarrow \boxed{\underline{\vec{E}} = -j\omega\underline{\vec{A}} - j\frac{1}{\omega\mu\epsilon}\nabla(\nabla \cdot \underline{\vec{A}})} \tag{2.160}$$

Once $\underline{\vec{A}}$ is found, $\underline{\vec{E}}$ and $\underline{\vec{H}}$ can be obtained easily. Solving for $\underline{\vec{A}}$ can be as difficult as for $\underline{\vec{E}}$ because it has the same wave equation, but choosing the path depends on the problem.

2.7.2 The Vector Potential $\vec{F}$

Similarly to what is done for the vector potential $\vec{A}$, the equations for the vector potential $\vec{F}$ will be derived [3]. The electric flux density $\vec{D}$ in a source free region obeys the equation($\nabla \cdot \vec{D} = 0$), and it is known that ($\nabla \cdot (-\nabla \times \vec{F}) = 0$) . Therefore, it can be equated to a curl of a vector field $\vec{F}$ as follows

$$\begin{aligned} \vec{D} &= -\nabla \times \vec{F}, \\ \Rightarrow \boxed{\vec{E} &= -\frac{1}{\epsilon}\nabla \times \vec{F}} \end{aligned} \tag{2.161}$$

By substituting it into Maxwell's second equation in harmonic form, the following is reached

$$\nabla \times (\underline{\vec{H}} + j\omega\underline{\vec{F}}) = 0, \tag{2.162}$$

and using the vector identity ($\nabla \times (-\nabla\phi_m) = 0$) reduces it to

$$\underline{\vec{H}} = -\nabla\phi_m - j\omega\underline{\vec{F}}, \tag{2.163}$$

where ϕ_m is a magnetic scalar potential. Taking the curl of (2.161) leads to

$$\nabla \times \underline{\vec{E}} = -\frac{1}{\epsilon}\nabla \times \nabla \times \underline{\vec{F}} = -\frac{1}{\epsilon}[\nabla(\nabla \cdot \underline{\vec{F}}) - \nabla^2\underline{\vec{F}}], \tag{2.164}$$

and by equating it to the first Maxwell's equation, the next formula can bee obtained

$$\nabla^2\underline{\vec{F}} + j\omega\mu\epsilon\underline{\vec{H}} = \nabla(\nabla \cdot \underline{\vec{F}}) - \epsilon\underline{\vec{M}}. \tag{2.165}$$

By substituting into it equation (2.163), it can be reduced to

$$\nabla^2\underline{\vec{F}} + \beta^2\underline{\vec{F}} = -\epsilon\underline{\vec{M}} + \nabla(\nabla \cdot \underline{\vec{F}} + j\omega\mu\epsilon\phi_m). \tag{2.166}$$

To simplify the equation, the following is considered

$$\begin{aligned} \nabla \cdot \underline{\vec{F}} &= -j\omega\mu\epsilon\phi_m, \\ \Rightarrow \phi_m &= -\frac{1}{j\omega\mu\epsilon}\nabla \cdot \underline{\vec{F}}, \end{aligned} \tag{2.167}$$

which reduces (2.166) to

$$\boxed{\nabla^2\underline{\vec{F}} + \beta^2\underline{\vec{F}} = -\epsilon\underline{\vec{M}}} \tag{2.168}$$

and (2.163) to

$$\underline{\vec{H}} = -j\omega\underline{\vec{F}} - \frac{j}{\omega\mu\epsilon}\nabla(\nabla \cdot \underline{\vec{F}}). \tag{2.169}$$

Therefore, once F is calculated, $\underline{\vec{E}}$ and $\underline{\vec{H}}$ can be obtained.

2.8 Electromagnetic Theorems

In this section, several important electromagnetic theorems will be presented [3].

2.8.1 Duality Theorem

This theorem states that when two equations have the same mathematical form, they have the same solutions. The variables described by these equations that have the same positions are the dual quantities. The solution of one can be derived from the other one by interchanging the symbols. Some of the dual equations are listed in table 2.2 [3]

Table 2.2: Several equations and their dual counterparts.

Electric sources ($\vec{J} \neq 0, \vec{M} = 0$)	Magnetic sources ($\vec{J} = 0, \vec{M} \neq 0$)
$\nabla \times \underline{\vec{E}} = -j\omega\mu\underline{\vec{H}}$	$\nabla \times \underline{\vec{H}} = j\omega\epsilon\underline{\vec{E}}$
$\nabla \times \underline{\vec{H}} = \underline{\vec{J}} + j\omega\epsilon\underline{\vec{E}}$	$-\nabla \times \underline{\vec{E}} = \underline{\vec{M}} + j\omega\mu\underline{\vec{H}}$
$\nabla^2\underline{\vec{A}} + \beta^2\underline{\vec{A}} = -\mu\underline{\vec{J}}$	$\nabla^2\underline{\vec{F}} + \beta^2\underline{\vec{F}} = -\epsilon\underline{\vec{M}}$
$\underline{\vec{A}} = \frac{\mu}{4\pi}\iiint_V \underline{\vec{J}}\frac{e^{-j\beta R}}{R}dV$	$\underline{\vec{F}} = \frac{\epsilon}{4\pi}\iiint_V \underline{\vec{M}}\frac{e^{-j\beta R}}{R}dV$
$\underline{\vec{H}} = \frac{1}{\mu}\nabla \times \underline{\vec{A}}$	$\underline{\vec{E}} = -\frac{1}{\epsilon}\nabla \times \underline{\vec{F}}$
$\underline{\vec{E}} = -j\omega\underline{\vec{A}} - j\frac{1}{\omega\mu\epsilon}\nabla(\nabla \cdot \underline{\vec{A}})$	$\underline{\vec{H}} = -j\omega\underline{\vec{F}} - j\frac{1}{\omega\mu\epsilon}\nabla(\nabla \cdot \underline{\vec{F}})$

The duality principle can be used to form mathematical solutions and imagine magnetic charges movements resulting in magnetic currents in comparison to electric charges and currents. Therefore, it is purely mathematical in nature because there are no magnetic charges or currents physically.

2.8.2 Uniqueness Theorem

When solving an electromagnetic problem, it should be determined if the solution derived is unique. A solution is unique in the case of the lossy medium in one of three cases [3]:

- The tangential components of the E field are determined over the boundary of the area
- The tangential components of the H field are determined over the boundary of the area

- One of them is determined within a section of the boundary, and the second over the remaining.

The lossless medium case is the same of the lossy one when the losses are considered to be the limit of zero.

2.8.3 Image Theory

When an electric source (Hertzian dipole) is located above a large plane interface between two media, the transmitted electromagnetic wave gets partially or completely reflected by it, and for an observer, it appears as if the reflected wave is coming from an image of the sources below the interface as if it is a mirrored image of the source [3]. This situation occurs, for instance, when the antenna is placed above a ground plane. The magnitude of the reflected wave is dependent on the constitutive properties of the two media, and for a perfect electric conductor, the wave is entirely reflected. Therefore, for simplicity, the case of PEC is considered in the analysis. Fig. 2.10 shows a vertical source above the PEC ground and its image behind the ground. At the boundary, the tangential electric field should be zero in this case, and therefore, the tangential components of the incidence field $\vec{E}_i$ and the reflected one $\vec{E}_r$ should be opposite to each other to cancel out. Thus, the vertical component is the same, and the polarization is the same, which means that the observer receives the two incoming waves (direct and reflected) in phase.

When the source is horizontal, the electric field at the boundary is tangential (Fig. 2.11). Therefore, the reflected field should be in opposite directions, and hence, the observer will see the two waves (incident and reflected) in opposite polarization, in other words, out of phase.

Considering a magnetic dipole above a PEC ground, if it is vertical, the polarization would be the opposite, and if it is horizontal, it would be the same. Therefore, it is contrary to the electric dipole case.

2.8.3.1 Vertical Electric Dipole

To calculate the electric field resulting from the addition of both the direct wave and the reflected one, an electric Hertzian dipole is considered over a PEC ground with a height of h as shown in Fig. 2.12a. The observer is at a distance r_1 from the actual source with angle θ_1, and at a distance r_2 from the image source with angle θ_2. The distance from the center point between the source and its image is r with angle θ. The length of the dipole is l. When $r \gg \lambda$, it results in the electric

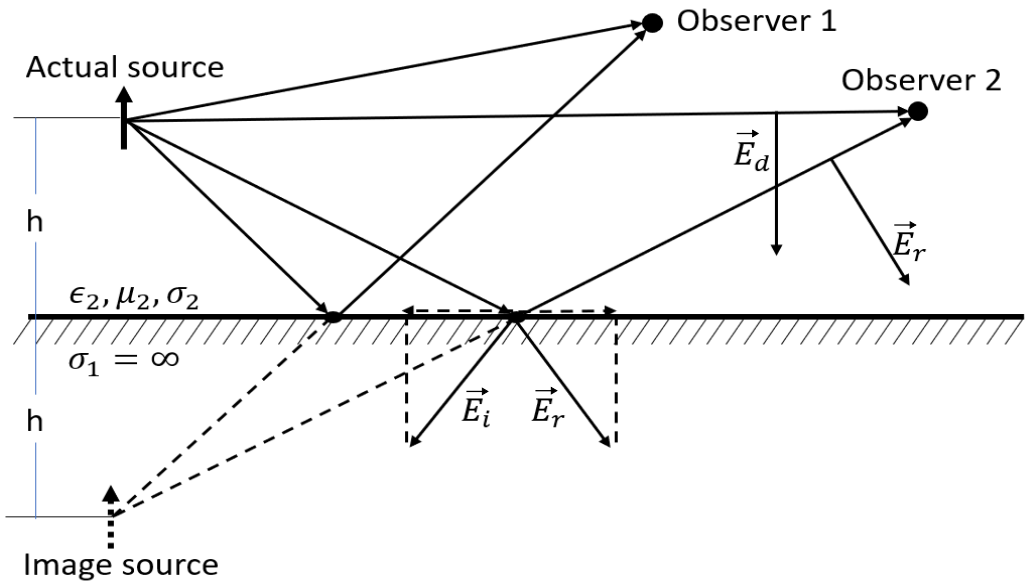

Figure 2.10: Vertical Hertzian dipole placed above PEC ground and its image.

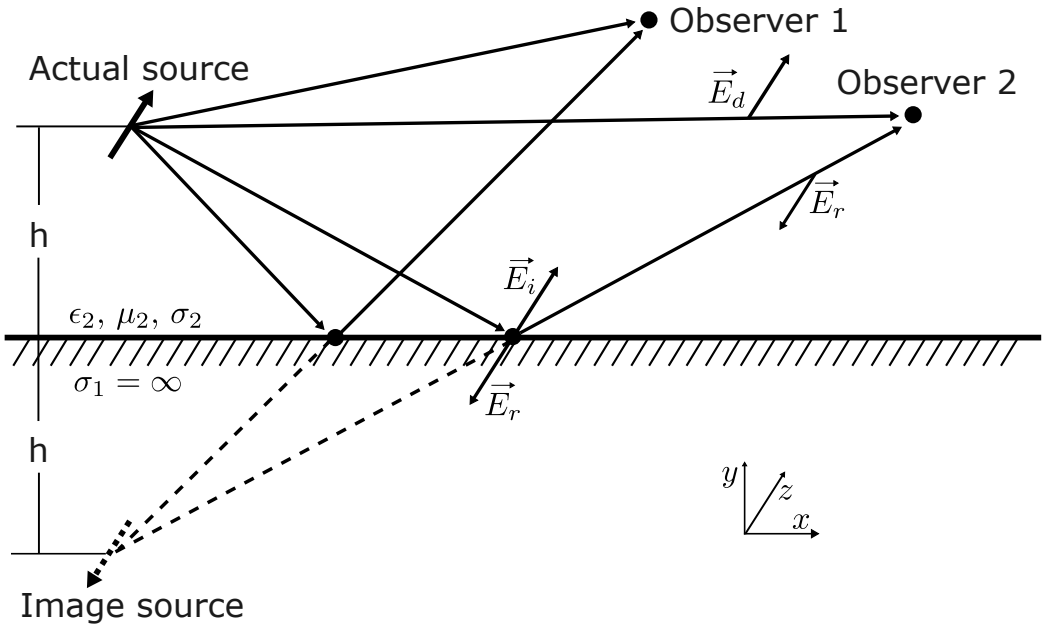

Figure 2.11: Horizontal Hertzian dipole placed above PEC ground and its image.

field of the direct path as [3]

$$E_\theta^d \approxeq j\eta \frac{\beta I_0 l e^{-j\beta r_1}}{4\pi r_1} \sin\theta_1, \tag{2.170}$$

where $\beta = 2\pi/\lambda$ and $\eta = \sqrt{\mu/\epsilon}$. The electric field is

$$E_\theta^r \approxeq jR\eta \frac{\beta I_0 l e^{-j\beta r_2}}{4\pi r_2} \sin\theta_2, \tag{2.171}$$

$$E_\theta^r \approxeq j\eta \frac{\beta I_0 l e^{-j\beta r_2}}{4\pi r_2} \sin\theta_2, \tag{2.172}$$

where R is the reflection coefficient with a value of 1 for PEC and vertical dipole. To add the fields up, for simplicity, the far-field situation is considered, where the following conditions are true

$$r \gg h, \tag{2.173}$$

$$\theta_1 \approx \theta_2 \approx \theta. \tag{2.174}$$

In this case, the total electric field can be found using

$$E_\theta = E_\theta^d + E_\theta^r = j\eta \frac{\beta I_0 l e^{-j\beta r}}{4\pi r} \sin\theta [2\cos(\beta h \cos\theta)]. \tag{2.175}$$

It can be realized that the total field is calculated from the field of the single source situated in the origin multiplied by a factor called the "*array factor*" [3], and the process is called the "*pattern multiplication*."

For example, the total electric field is calculated at a frequency of $77\,\mathrm{GHz}$, which results in $\lambda = 0.0039\,\mathrm{mm}$, for $E_0 = 1$, $l = \lambda/4$, and $h = 2\lambda$ and 5λ, and the plot is shown in Fig. 2.13

2.8.3.2 Horizontal Electric Dipole

For the horizontal dipole case, the same analysis follows, but the horizontal electric field E_ψ is considered. Here, as explained before, the direct and reflected fields are in opposite directions. Thus, the reflection coefficient R is -1 instead of 1. The final equation for the total electric field is [3]

$$E_\psi = E_\psi^2 + E_\psi^r = j\eta \frac{\beta I_0 l e^{-j\beta r}}{4\pi r} \sqrt{1 - \sin^2\theta \sin^2\Phi} [2j\sin(\beta h \cos\theta)], \tag{2.176}$$

where ψ is the angle between r and the axis y as shown in Fig. 2.14.

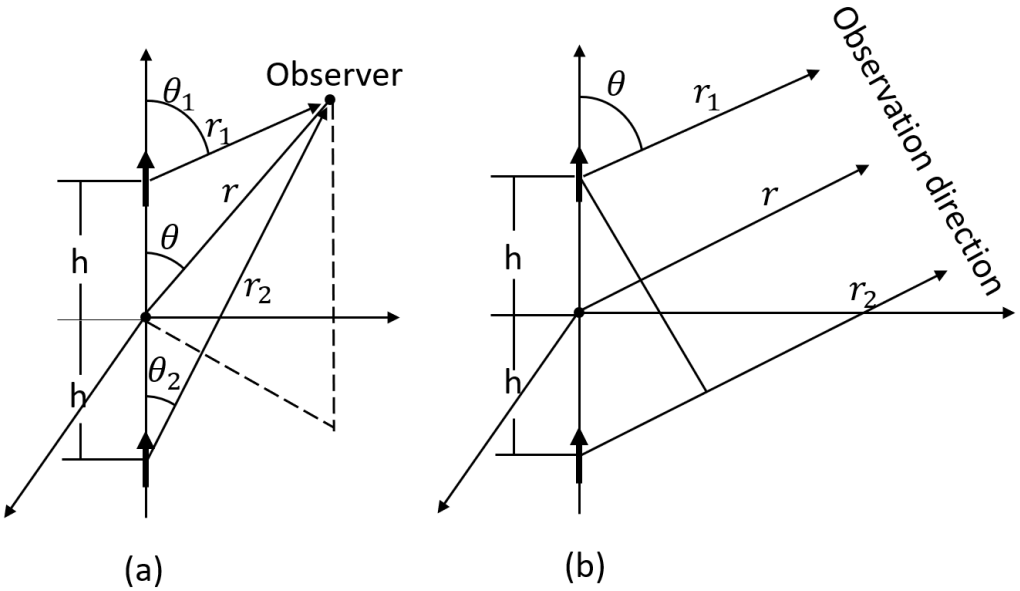

Figure 2.12: Vertical electric dipole above PEC ground. When the observation point is in the near field (a), and when in far-field (b).

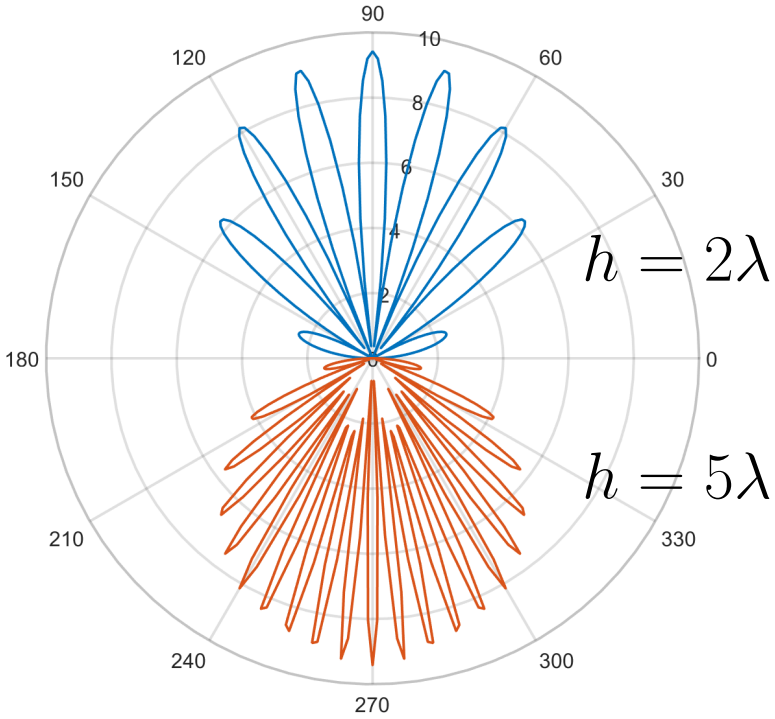

Figure 2.13: The total electric field of an electric dipole above a PEC ground at far-field with respect to angle. The upper half is for $h = 2\lambda$, and the lower half for $h = 5\lambda$.

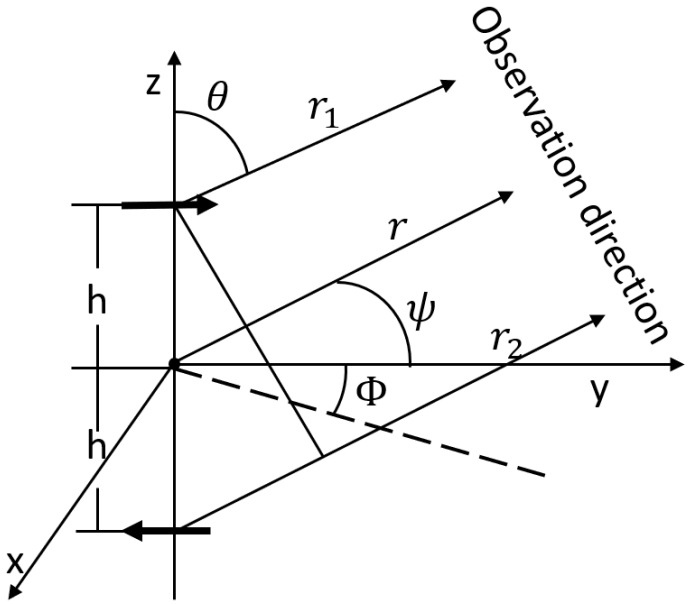

Figure 2.14: Horizontal electric dipole above PEC ground when the observation point is in the far field.

2.8.4 Reciprocity Theorem

There are many forms of the reciprocity theorem. The one stated here pertains to the electromagnetic transmitters and receivers. It states that if the electric field radiated by a transmitter is measured by a receiver at some other point, then the positions of them are exchanged, and the measured electromagnetic field will be the same [3].

2.8.5 Volume Equivalence Theorem

When electromagnetic waves travel through space and encounter a dielectric object, a scattered wave is additionally created, and it should satisfy Maxwell's equations as well. To account for the change in the electromagnetic fields, equivalent electric and magnetic sources are introduced with the equations [3]

$$\vec{J}_{eq} = j\omega(\epsilon - \epsilon_0)\vec{E}, \tag{2.177}$$

$$\vec{M}_{eq} = j\omega(\mu - \mu_0)\vec{H}. \tag{2.178}$$

These sources will generate a scattered field that is added to the original fields, which should satisfy Maxwell's equations, resulting in

$$\nabla \times \vec{E}^s = -\vec{M}_{eq} - j\omega\mu_0\vec{H}^s, \tag{2.179}$$

$$\nabla \times \vec{H}^s = \vec{J}_{eq} + j\omega\epsilon_0\vec{E}^s. \tag{2.180}$$

These equations are not easy to solve because the equivalent currents are based on the unknown fields, but they can be a basis for integral equations to solve for E^s and H^s when scattered by a dielectric object.

2.8.6 Surface Equivalence Theorem (Huygens' Principle)

The Huygen's surface equivalent theorem states that [3] on a main wavefront, we can assume each point to form a new source emanating a secondary spherical wave, and the envelope of these waves forms a secondary wavefront. This is used to analyze the radiation of a complicated structure or antenna by forming an imaginary surface that encloses the studied entity. To illustrate the use of the theorem, consider Fig. 2.15. The original problem is represented by electric and magnetic currents, radiating the fields $\vec{E}_1, \vec{H}_1$ in and outside the surface S. The equivalent problem is formulated by introducing virtual electric and magnetic currents on the virtual surface S that encloses the original problem. These imaginary currents radiate the same external fields outside S but different fields $\vec{E}, \vec{H}$ inside the surface.

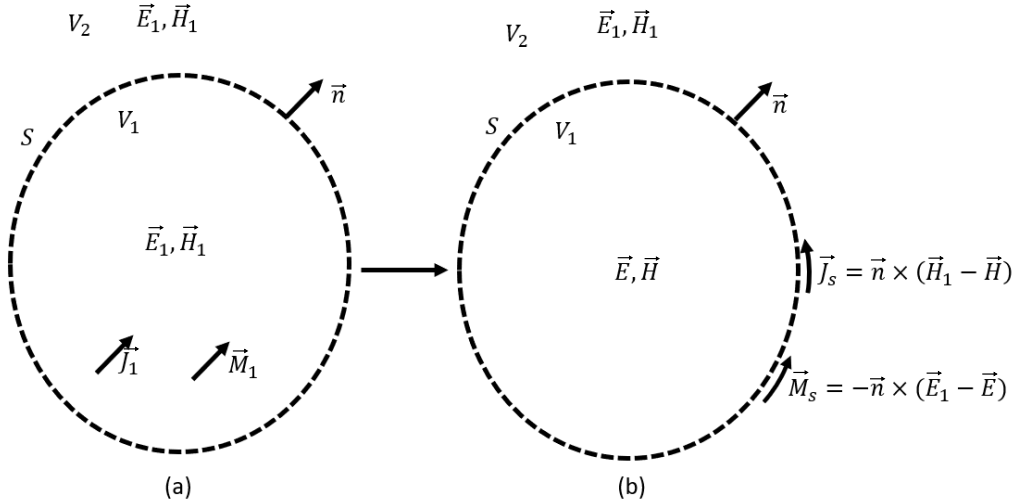

Figure 2.15: Surface equivalence theorem. The original problem of radiating electric and magnetic currents inside the virtual surface in (a). The equivalent problem with virtual electric and magnetic currents impressed on the virtual surface in (b).

The boundary conditions must be satisfied on the surface S, and therefore, the equivalent sources are:

$$\vec{J}_s = \vec{n} \times (\vec{H}_1 - \vec{H}), \tag{2.181}$$

$$\vec{M}_s = -\vec{n} \times (\vec{E}_1 - \vec{E}), \tag{2.182}$$

which radiate everywhere. Since the internal fields might be of any value, they can be set to zero, resulting in the equations:

$$\vec{J}_s = \vec{n} \times \vec{H}_1, \tag{2.183}$$

$$\vec{M}_s = -\vec{n} \times \vec{E}_1, \tag{2.184}$$

which are known as "Love's equivalence principle." Now, it is assumed that inside the virtual surface, the space is filled with a perfect electric conductor, then $\vec{J}_s = 0$ is satisfied, and there are only magnetic currents, but the radiation pattern of them is affected by the PEC boundary. In the general case, this is a problem as difficult as the original one. Therefore, it is assumed that the surface is flat and extended with no limit, as depicted in Fig. 2.16a. In this case, the image theory can be applied, which means that a virtual image of the magnetic current is created behind the surface, as shown in Fig. 2.16b. Then the two currents are merged together to produce double the field according to $\vec{M}_s = -2\vec{n} \times \vec{E}_1$ and is shown in 2.16c.

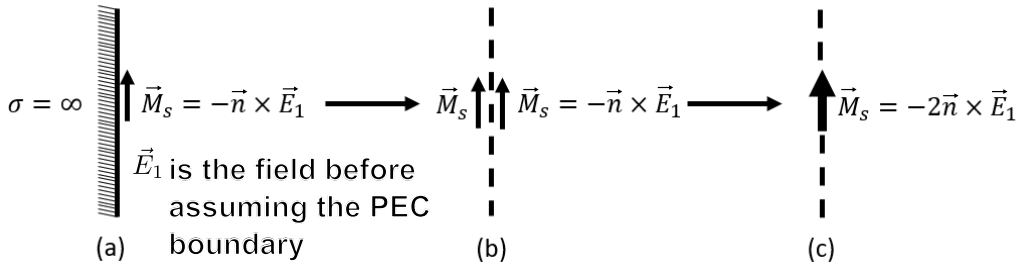

Figure 2.16: Surface equivalence theorem when the boundary is flat and extended to infinity. (a) the magnetic currents next to the boundary. (b) Image magnetic currents are placed behind the surface in the same direction as the original ones. (c) the original and the image currents are combined.

2.8.7 Induction Equivalence Theorem

The induction equivalence theorem is dedicated to scattering problems by objects in electromagnetic waves by substituting the physical object with equivalent electric and magnetic current densities. As shown in Fig. 2.17a, the electric and magnetic currents $\vec{J}_1$ and $\vec{M}_1$ respectively radiate in the medium, including inside the imaginary surface S_1, the fields $\vec{E}_1$ and $\vec{H}_1$. Now, the surface is filled with a different material with constitutive properties ϵ_2 and μ_2. Therefore, the fields inside the volume V_1 become $\vec{E}^t$ and $\vec{H}^t$, and outside the volume they become [3]

$$\vec{E} = \vec{E}_1 + \vec{E}^s, \tag{2.185}$$

$$\vec{H} = \vec{H}_1 + \vec{H}^s, \tag{2.186}$$

where $\vec{E}^s$ and $\vec{H}^s$ are known as scattered fields caused by the obstacle inside the surface. Since now different fields exist inside and outside the surface, the boundary conditions must be satisfied by introducing equivalent current densities located on the bounding surface as:

$$\vec{J}_i = \vec{n} \times (\vec{H}^s - \vec{H}^t), \tag{2.187}$$

$$\vec{M}_i = -\vec{n} \times (\vec{E}^s - \vec{E}^t). \tag{2.188}$$

According to the boundary conditions, it is known that the tangential components across the boundary are continuous, which means

$$\vec{n} \times (\vec{E}_1 + \vec{E}^s) = \vec{n} \times \vec{E}^t, \tag{2.189}$$

$$\vec{n} \times (\vec{H}_1 + \vec{H}^s) = \vec{n} \times \vec{H}^t, \tag{2.190}$$

and this can be rewritten as:

$$\vec{n} \times (\vec{E}^s - \vec{E}^t) = -\vec{n} \times \vec{E}_1, \tag{2.191}$$

$$\vec{n} \times (\vec{H}^s - \vec{H}^t) = -\vec{n} \times \vec{H}_1. \tag{2.192}$$

By substituting the last equations into (2.187 and 2.188), the following equations result

$$\vec{J}_i = -\vec{n} \times \vec{H}_1, \tag{2.193}$$

$$\vec{M}_i = \vec{n} \times \vec{E}_1, \tag{2.194}$$

which is shown in Fig.2.17c.

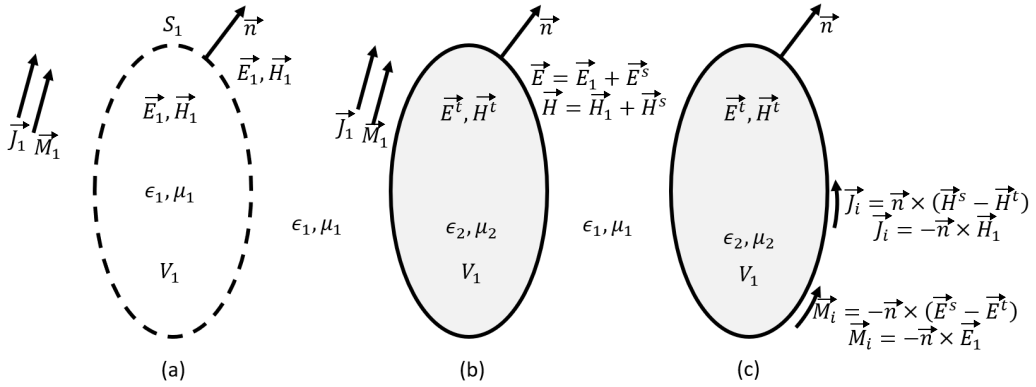

Figure 2.17: Induction equivalence theorem. (a) The original problem with an imaginary surface. (b) The closed surface is filled with a different material property, resulting in different fields inside and outside. (c) The equivalent problem is set up by introducing the imaginary electric and magnetic currents.

Now, the original problem is replaced by an equivalent problem where equivalent currents are placed on the surface, which radiates near an obstacle with a different material. Therefore, this problem is not easier than the original unless simplifications are introduced. For that, it is assumed that the inside of the obstacle is filled with perfect electric conductor. According to the uniqueness theorem, only one of the currents is needed over the boundary, so only the magnetic currents $\vec{M}_i = \vec{n} \times \vec{E}_1$ are kept. The other simplification is to consider the boundary as flat and extending to infinity, as shown in Fig.2.18a. Then, using the image theory, mirrored magnetic sources are placed behind the surface equal in magnitude and direction to the original ones, as shown in Fig.2.18b. The last step is to combine them as illustrated in Fig.2.18c to yield the magnetic currents such that

$$\vec{M}_i = 2\vec{n} \times \vec{E}_1, \tag{2.195}$$

which radiates into unbounded homogeneous space, and thus, the resulting fields can be calculated.

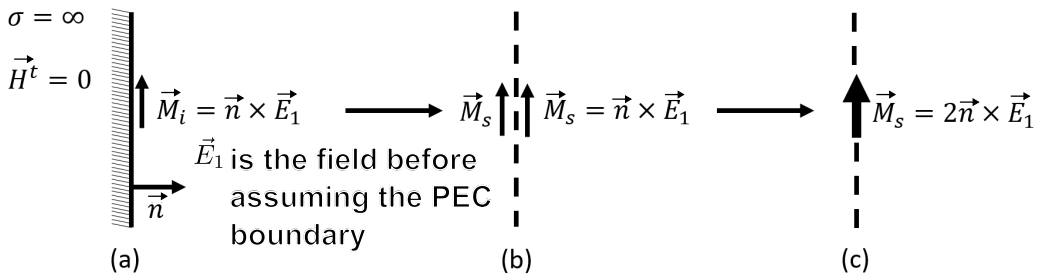

Figure 2.18: Induction equivalence theorem when the boundary is flat, extending to infinity, and the material is PEC in (a). Using image theory to replace the boundary with virtual image magnetic currents in (b). The resulting magnetic current in (c).

2.8.8 Physical Optics Equivalent

Considering the problem of an obstacle of the perfect electric conductor in the fields of $\vec{J}_1, \vec{M}_1$ as depicted in Fig.2.19a. Without the obstacle, the fields are $\vec{E}_1, \vec{H}_1$, which can be calculated, while when the obstacle is present, the fields inside it are zero, and outside it they are [3]

$$\vec{E} = \vec{E}_1 + \vec{E}^s, \tag{2.196}$$

$$\vec{H} = \vec{H}_1 + \vec{H}^s. \tag{2.197}$$

Now, the equivalent problem is formulated by replacing the object with its surface and placing fictitious currents on the boundary, as can be seen in Fig. 2.19b. Due to the uniqueness theorem, either the electric or the magnetic currents on the surface should be found. Therefore, only the electric currents are kept and the magnetic currents are set to zero. As a result, on the boundary, the following holds

$$\vec{M}_p = -\vec{n} \times (\vec{E} - \vec{E}^t) = -\vec{n} \times \vec{E} = -\vec{n} \times (\vec{E}_1 + \vec{E}^s) = 0, \tag{2.198}$$

$$\Rightarrow \quad -\vec{n} \times \vec{E}_1 = \vec{n} \times \vec{E}^s, \tag{2.199}$$

$$\vec{J}_p = \vec{n} \times (\vec{H} - \vec{H}^t) = \vec{n} \times \vec{H} = \vec{n}(\vec{H}_1 + \vec{H}^s), \tag{2.200}$$

$$\Rightarrow \quad \vec{J}_p = \vec{n} \times \vec{H}_1 + \vec{n} \times \vec{H}^s. \tag{2.201}$$

These currents will produce $\vec{E}^s, \vec{H}^s$ outside the volume (scattered fields) and $-\vec{E}_1, -\vec{H}_1$ inside it since the following equations hold

$$\vec{J}_p = \vec{n}(\vec{H}_1 + \vec{H}^s) = \vec{n} \times [\vec{H}^s - (-\vec{H}_1)], \tag{2.202}$$

$$\vec{M}_p = -\vec{n} \times (\vec{E}_1 + \vec{E}^s) = -\vec{n} \times [\vec{E}^s - (-\vec{E}_1)] = 0. \tag{2.203}$$

The fictitious currents are dependent on the total fields $\vec{E}, \vec{H}$. Therefore, solving the equivalent problem is as hard as the original one. However, additional simplification can be assumed, which is to consider the surface at each point as flat and extends to infinity as shown in Fig. 2.19c, enabling the writing of the formula of $\vec{J}_p$ as

$$\vec{J}_P = \vec{n} \times \vec{H} = \vec{n} \times (\vec{H}_1 + \vec{H}^s) = 2\vec{n} \times \vec{H}_1, \tag{2.204}$$

which is called the physical optics approximation.

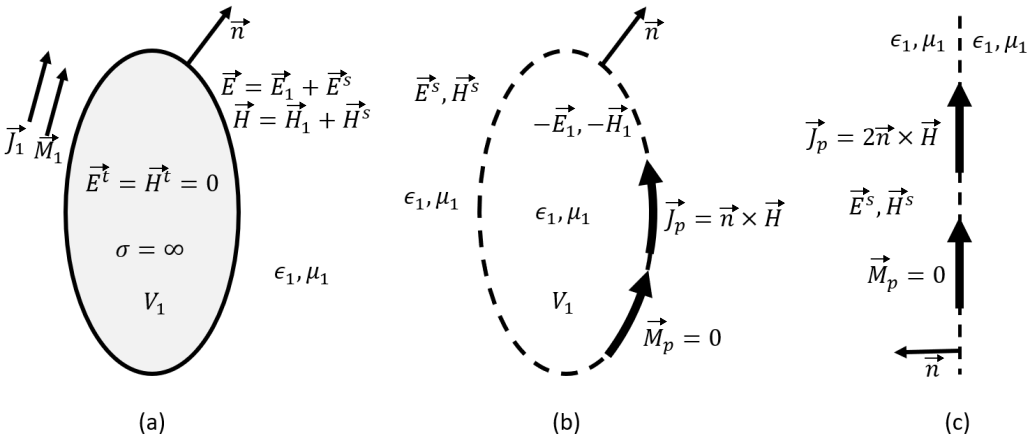

Figure 2.19: Physical equivalent theorem. (a) the original problem. (b) the equivalent problem. (c) the flat surface approximation.

2.9 Geometrical Optics (GO)

The geometrical optics (GO) method was originally developed to simulate light rays at very high frequencies, which allows us to not consider the wave nature of light [3]. Therefore, GO is a high-frequency asymptotic method to simulate wave propagation and its interaction with matter. i.e., reflection, refraction, and transmission. In GO, reflection is simulated considering only specular direction, which is accurate for smooth surfaces with curvature much larger than the

wavelength. If the medium is homogeneous, then the waves propagate in straight lines, and reflect off surfaces according to the reflection law, i.e., the incidence and reflection angles are equal. Further more, the power per unit solid angle is conserved in a tube of rays.

The primary wavefront is a line perpendicular to the rays emanating from the source in all directions at a specific time point. To form a secondary wavefront, a few points are selected on the primary wavefront and dray lines vertical to it at each point, and at a second time point along the lines (rays), a second wavefront is drawn perpendicular to all the rays. This can be done again to form further wavefronts, as shown in Fig. 2.20. These wave fronts are called also $eikonal$

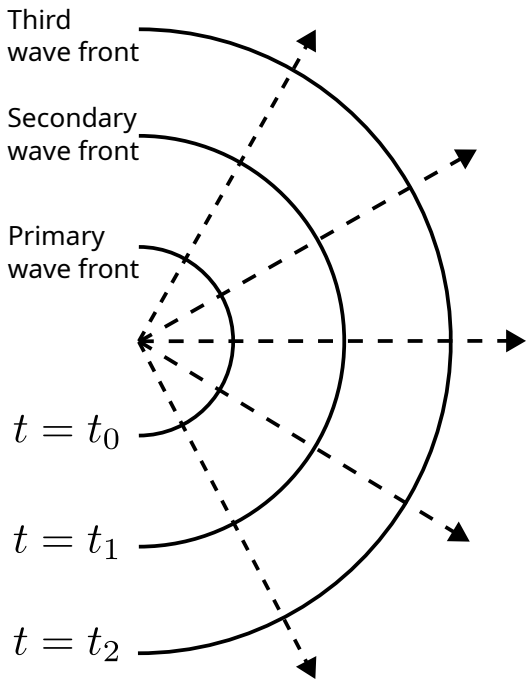

Figure 2.20: Construction of primary, secondary, and third wavefronts.

surfaces.

2.9.1 Amplitude of the E Field in Rays

The conservation of energy flux in a tube of rays states that the power per unit solid angle is conserved [3]. For the case of a point source emitting spherical waves as shown in Fig. 2.21. The surface area at the reference point $s = 0$ and at s are represented by dA_0 and dA, respectively. The radiation density S at s, and

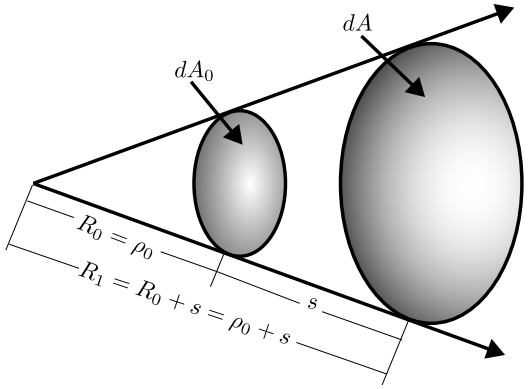

Figure 2.21: Tube of rays for a spherical wave point source.

S_0 at 0 are given by [3]

$$\frac{S(s)}{S_0(0)} = \frac{dA_0}{dA}. \tag{2.205}$$

The electric field in the far-field region is related to the radiation density by

$$S = \frac{1}{2}\sqrt{\frac{\epsilon}{\mu}}|\vec{E}|^2. \tag{2.206}$$

Therefore, the next equation is true

$$\frac{|\vec{E}|^2}{|\vec{E}_0|^2} = \frac{dA_0}{dA}, \tag{2.207}$$

or

$$\frac{|\vec{E}|}{|\vec{E}_0|} = \sqrt{\frac{dA_0}{dA}}. \tag{2.208}$$

And since the surfaces dA_0 and dA are sections of spheres with corresponding radii of curvature R_0 and R_1 respectively, 2.208 can be written as

$$\frac{|\vec{E}|}{|\vec{E}_0|} = \sqrt{\frac{dA_0}{dA}} = \sqrt{\frac{4\pi R_0^2/C_0}{4\pi R_1^2/C_0}} = \frac{R_0}{R_1} = \frac{\rho_0}{\rho_0 + s}, \tag{2.209}$$

where C_0 is a proportionality constant. When the wave front surface (eikonal surface) is cylindrical, the following results

$$\frac{|\vec{E}|}{|\vec{E}_0|} = \sqrt{\frac{dA_0}{dA}} = \sqrt{\frac{4\pi R_0/C_1}{4\pi R_1/C_1}} = \sqrt{\frac{R_0}{R_1}} = \sqrt{\frac{\rho_0}{\rho_0 + s}}, \tag{2.210}$$

and finally, when the wave front is planar, the following holds

$$\frac{|\vec{E}|}{|\vec{E}_0|} = 1. \tag{2.211}$$

In general, the surface of the wavefront might have two radii of curvature, one in the vertical plane and the other in the horizontal plane ($R_1 \neq R_2$), as shown in Fig. 2.22. As can be seen, the rays 1,2,3, and 4 intersect at various points. This

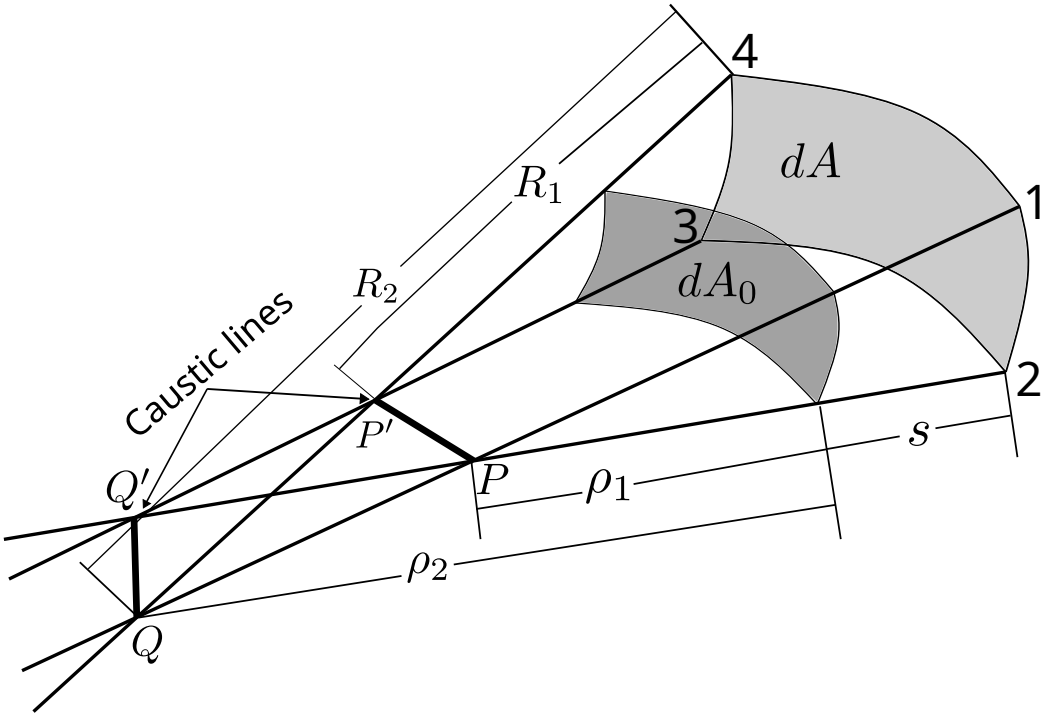

Figure 2.22: Wave front surface with two radii of curvature [3].

tube of rays is called *astigmatic*, and the lines PP' and QQ' are named *caustic*. In this case, the electric field intensity for one surface relative to another is given by [3]

$$\boxed{\frac{|\vec{E}|}{|\vec{E}_0|} = \sqrt{\frac{dA_0}{dA}} = \sqrt{\frac{\rho_1\rho_2}{(\rho_1+s)(\rho_2+s)}}} \tag{2.212}$$

It can be deduced that this general equation reduces to one of the following equivalent cases

- Spherical when ($\rho_1 = \rho_2$)
- Cylindrical when $\rho_1 = \infty$ or $\rho_2 = \infty$
- Planar when $\rho_1 = \rho_2 = \infty$

2.9.2 Phase Factor

It can be shown that considering the phase factor and solving the wave equation considering the astigmatic wave front yields the equation [3]

$$\vec{E}(s) = \underbrace{\vec{E}_0'(0)e^{j\phi_0(0)}}_{\substack{\text{Field at reference} \\ \text{point(s=0)}}} \underbrace{\sqrt{\frac{\rho_1\rho_2}{(\rho_1+s)(\rho_2+s)}}}_{\substack{\text{Spatial attenuation} \\ \text{(divergence, spreading)} \\ \text{factor}}} \underbrace{e^{-j\beta s}}_{\substack{\text{Phase} \\ \text{factor}}}. \tag{2.213}$$

This equation is a high frequency approximation, and its accuracy increases with frequency. Never the less, in several practical problems, it predicts sufficiently accurate results.

2.9.3 Reflection from Surfaces

Geometrical optics can be used to determine the reflected fields for high-frequency waves [3]. It states that incidence and reflection angles are equal as shown in Fig. 2.23, where $\vec{s}^{\,i}$ is the unit vector in the direction of incidence, Q_R is the reflection point, $\vec{e}_{\parallel}^{\,i}$, $\vec{e}_{\parallel}^{\,r}$ are the unit vectors for the incident and reflected fields, parallel to the plane of incidence, $\vec{s}^{\,r}$ is the unit vector in the direction of reflection, and $\vec{e}_{\perp}^{\,i}$, $\vec{e}_{\perp}^{\,r}$ are the unit vectors for the electromagnetic fields, perpendicular to the plane of incidence. The plane of incidence is the plane containing the normal vector $\vec{n}$, the unit vector $\vec{s}^{\,i}$, and the point of reflection Q_R. The angle between $\vec{n}$ and $\vec{s}^{\,i}$ is the incidence angle θ_i, and the angle between $\vec{n}$ and $\vec{s}^{\,r}$ is the reflection angle θ_r, and they are equal. The polarization unit vectors are configured such that

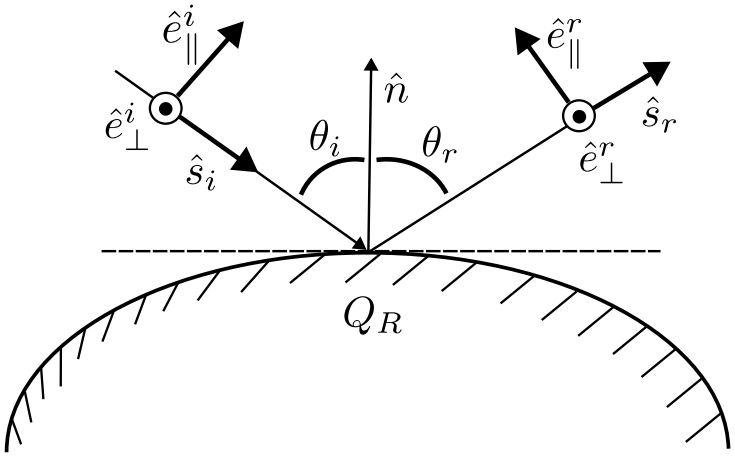

Figure 2.23: Reflection of an electromagnetic wave by a curved surface [3].

$$\vec{e}_{\perp}^{\,i} \times \vec{s}^{\,i} = \vec{e}_{\parallel}^{\,i}, \tag{2.214}$$

$$\vec{e}_{\perp}^{\,r} \times \vec{s}^{\,r} = \vec{e}_{\parallel}^{\,r}, \tag{2.215}$$

and the electric incident and reflected fields are obtained by

$$\vec{E}_0^{\,i} = \vec{e}_{\parallel}^{\,i} E_{0\parallel}^{\,i} + \vec{e}_{\perp}^{\,i} E_{0\perp}^{\,i}, \tag{2.216}$$

$$\vec{E}_0^{\,r} = \vec{e}_{\parallel}^{\,r} E_{0\parallel}^{\,r} + \vec{e}_{\perp}^{\,r} E_{0\perp}^{\,r}. \tag{2.217}$$

Considering a perfect electric conductor (PEC) and applying the boundary condition that states that the tangential components of the electric field are zero, gives us the relation between the incident and reflected field at the point of reflection as [3]

$$\vec{E}_0^{\,r}(s=0) = \vec{E}_0^{\,i}(Q_R) \cdot \bar{R} = \vec{E}_0^{\,i}(Q_R) \cdot [\vec{e}_{\parallel}^{\,i}\vec{e}_{\parallel}^{\,r} - \vec{e}_{\perp}^{\,i}\vec{e}_{\perp}^{\,r}], \tag{2.218}$$

where $\bar{R}$ is the dyadic reflection coefficient, which can be written in matrix form as

$$R = \begin{bmatrix} 1 & 0 \\ 0 & -1 \end{bmatrix}. \tag{2.219}$$

Thus, it can be realized that two approximations are applied

- The reflecting surface is considered planar at the point of reflection
- The wave front of the incident field is as well planar

Therefore, considering (2.213 and 2.218), results in the equation [3]

$$\vec{E}(s) = \underbrace{\vec{E}^{\,i}(Q_R)}_{\substack{\text{Field at reference} \\ \text{point(s=0)}}} \cdot \underbrace{\bar{R}}_{\substack{\text{Reflection} \\ \text{Coefficient}}} \cdot \underbrace{\sqrt{\frac{\rho_1\rho_2}{(\rho_1+s)(\rho_2+s)}}}_{\substack{\text{Spatial attenuation} \\ \text{(divergence, spreading)} \\ \text{factor}}} \underbrace{e^{-j\beta s}}_{\substack{\text{Phase} \\ \text{factor}}}. \tag{2.220}$$

In the case of a tube of rays reflecting off a curved surface, as shown in Fig. 2.24, the equations relating the radii of curvature for the incident and reflected wave fronts are found as

$$\frac{1}{\rho_1^r} = \frac{1}{2}\Big(\frac{1}{\rho_1^i} + \frac{1}{\rho_2^i}\Big) + \frac{1}{f_1}, \tag{2.221}$$

$$\frac{1}{\rho_2^r} = \frac{1}{2}\Big(\frac{1}{\rho_1^i} + \frac{1}{\rho_2^i}\Big) + \frac{1}{f_2}, \tag{2.222}$$

where ρ_1^i and ρ_2^i are the principal radii of curvature for the incident wavefront, and f_1 and f_2 are focal distances. The equations for f_1 and f_2, when the wavefront for

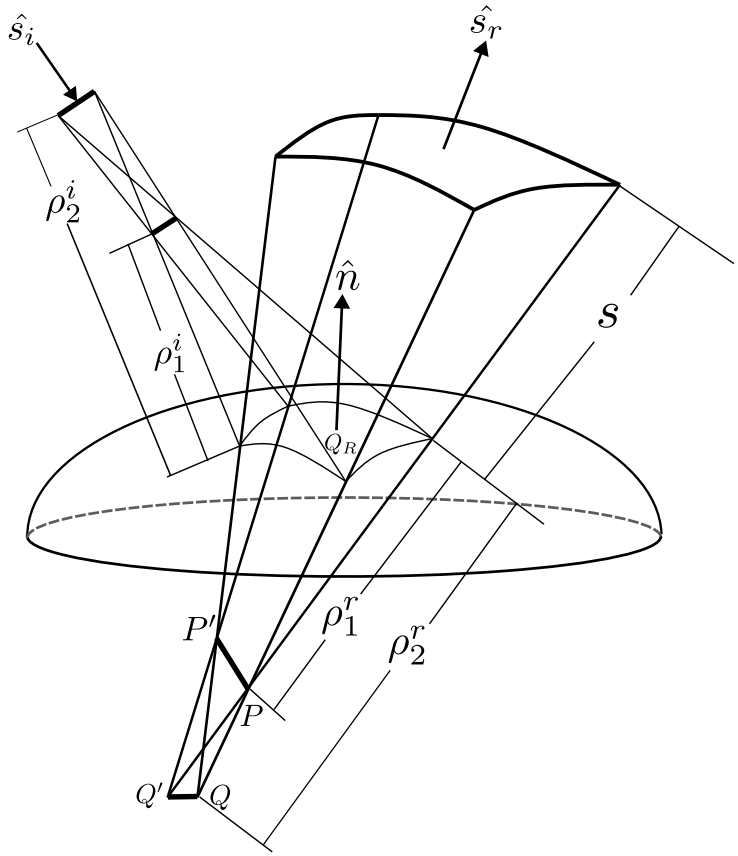

Figure 2.24: Reflection of electromagnetic wave with curved wavefront by a curved surface [3].

the incident electric field is spherical, are [3]

$$\frac{1}{f_1} = \frac{1}{\cos\theta_i}\Big(\frac{\sin^2\theta_2}{R_1} + \frac{\sin^2\theta_1}{R_2}\Big) + \sqrt{\frac{1}{\cos^2\theta_i}\Big(\frac{\sin^2\theta_2}{R_1} + \frac{\sin^2\theta_1}{R_2}\Big)^2 - \frac{4}{R_1 R_2}}, \tag{2.223}$$

$$\frac{1}{f_2} = \frac{1}{\cos\theta_i}\Big(\frac{\sin^2\theta_2}{R_1} + \frac{\sin^2\theta_1}{R_2}\Big) - \sqrt{\frac{1}{\cos^2\theta_i}\Big(\frac{\sin^2\theta_2}{R_1} + \frac{\sin^2\theta_1}{R_2}\Big)^2 - \frac{4}{R_1 R_2}}, \tag{2.224}$$

where R_1, R_2 are the radii of curvature of the reflecting surface

θ_1 is the angle between the direction of incidence $\hat{s}^i$ and $\hat{u}_1$

θ_2 is the angle between the direction of incidence $\hat{s}^i$ and $\hat{u}_2$

$\hat{u}_1$ the unit vector in the first principal direction of S with a radius of R_1

$\hat{u}_2$ the unit vector in the second principal direction of S with a radius of R_2

2.10 The Physical Optics Method

The physical optics technique is a high-frequency approximation [5], where the first step is to find the equivalent current densities on the illuminated surface of a perfectly electrically conductive (PEC) object. After determining these current densities, the electric and magnetic fields are determined from the radiation integrals. The PO method is suitable when dealing with electrically large problems (the dimension is much larger than the wavelength) and with radii of curvature much larger than the wavelength. Another problem needs to be tackled when utilizing the method of PO, which is the line of sight to all the points on the surface to determine the lit region from the one in the shadow.

2.10.1 PO Formulation

As described in the section "physical optics equivalent" (2.8.8), a PEC object can be replaced by a virtual boundary with impressed equivalent currents as shown in Fig. 2.25, and the currents are expressed by the equations

$$\vec{J}^{PO} = \vec{n} \times (\vec{H}^{inc} + \vec{H}^{ref}) \approx 2\vec{n} \times \vec{H}^{inc}, \tag{2.225}$$

$$\vec{M}^{PO} = -\vec{n} \times (\vec{E}^{inc} + \vec{E}^{ref}) = 0. \tag{2.226}$$

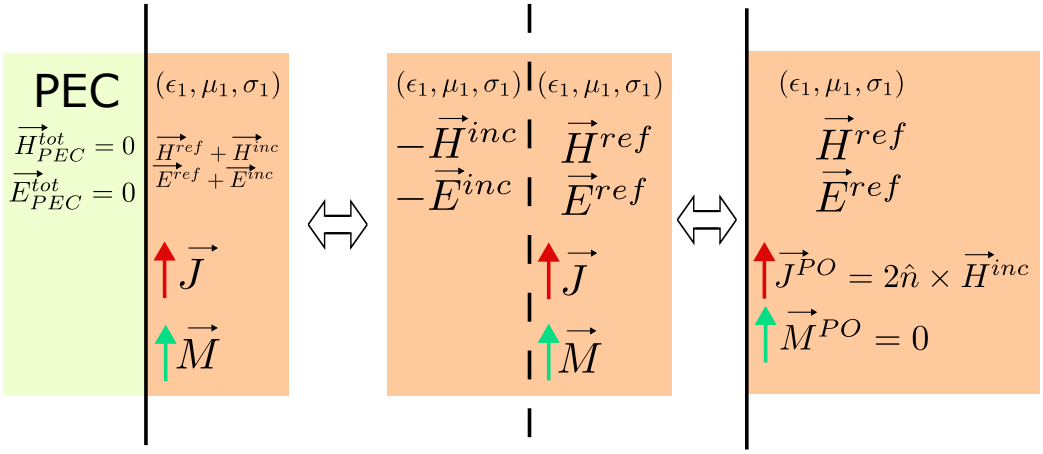

Figure 2.25: Induced equivalent PO electric and magnetic currents [5].

2.10.2 The Modified Equivalent Current Approximation (MECA) Method

The physical optics (PO) method is restricted to work with perfect electric conductor (PEC) objects, which limits the scope of applications where this method can be employed. Therefore, the modified equivalent current approximation (MECA) method is introduced to handle penetrable and dielectric objects [5]. This method accounts for the reflection coefficient R when applying the boundary conditions between two media; usually, one is air, and the other is a dielectric medium. To perform the calculations, it is simpler to decompose the incident fields into two components: transverse electric (TE) and transverse magnetic (TM). The TE component is in which the electric field is perpendicular to the incidence plane, while the TM is in which the magnetic field is perpendicular to the plane of incidence. This way, the reflection coefficients R_{TE} and R_{TM} can be applied to each one separately. The incident electric field is decomposed as

$$\vec{E}^{inc} = E^{inc}_{TE}\vec{e}_{TE} + E^{inc}_{TM}\vec{e}_{TM}, \tag{2.227}$$

where $\vec{e}_{TE}$ and $\vec{e}_{TM}$ are the vectors with unit length in the directions of the transverse electric and transverse magnetic components of the incoming electric field, respectively, E^{inc}_{TE} and E^{inc}_{TM} are the components of the electric field on each unit vector. The magnetic fields are decomposed in a similar manner. The most important characteristics of the MECA method are [5]:

- MECA can handle electrically large objects of dielectric surfaces by taking into consideration both electric and magnetic equivalent currents, $\vec{J}^{MECA}$ and $\vec{M}^{MECA}$.

- When dealing with PEC objects, MECA becomes PO. Therefore, MECA can be considered as extension of the typical Physical Optics approximation

2.10.3 MECA Formulation

A plane wave is assumed incident on the surface of a dielectric medium S with an angle of incidence θ^{inc} and a vector in the incident direction with a unit length $\vec{k}^{inc}$. The two media have electric permittivities (ϵ_1, ϵ_2) and magnetic permeabilities (μ_1, μ_2), respectively. The cases of TE and TM are studied separately.

2.10.3.1 TE Component

A coordinate system is chosen for the incident wave as

$$[\vec{k}^{inc}, \vec{e}_{TM}, \vec{e}_{TE}], \tag{2.228}$$

where

$$\vec{e}_{TE} = \frac{\vec{k}^{inc} \times \vec{n}}{|\vec{k}^{inc} \times \vec{n}|}, \tag{2.229}$$

$$\vec{e}_{TM} = \vec{e}_{TE} \times \vec{k}^{inc}, \tag{2.230}$$

which are shown in Fig. 2.26, where $[\vec{k}^{inc},\vec{e}_{TM},\vec{e}_{TE}]$ and $[\vec{s}_{TM},\vec{k}^{ref},\vec{s}_{TE} = \vec{e}_{TE}]$ are coordinate systems for the incident and reflected waves, respectively. The

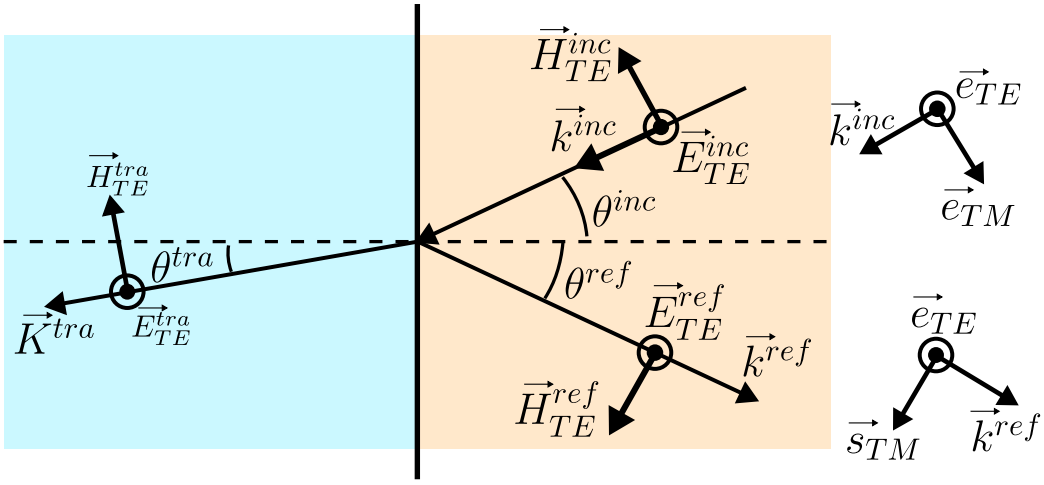

Figure 2.26: TE components of the field decomposition [5].

incident fields are written in these unit vectors as follows:

$$\vec{E}_{TE}^{inc} = E_{TE}^{inc}\vec{e}_{TE}, \tag{2.231}$$

$$\vec{H}_{TE}^{inc} = -H_{TE}^{inc}\vec{e}_{TM} = \frac{1}{\eta}E_{TE}^{inc}(\vec{k}^{inc} \times \vec{e}_{TE}), \tag{2.232}$$

where η is the intrinsic impedance, which for the non-lossy medium is

$$\eta = \sqrt{\frac{\mu}{\epsilon}}. \tag{2.233}$$

To find the system of coordinates to the reflected fields, the two facts according to Snell's law are used as

- The angle of incidence θ^{inc} is equal to the angle of reflection θ^{ref}
- The plane of incidence spanned by $\vec{k}^{inc}$ and the normal $\vec{n}$ is the same as the plane of reflection spanned by $\vec{k}^{ref}$ and the normal.

Therefore, the unit vector is found in the reflection direction using

$$\vec{k}^{ref} = \vec{k}^{inc} - 2\vec{n}(\vec{k}^{inc} \cdot \vec{n}). \tag{2.234}$$

Thus the coordinate system for the reflected fields is defined as $[\vec{s}_{TM}, \vec{k}^{ref}, \vec{s}_{TE} = \vec{e}_{TE}]$, and the reflected fields are defined based on this system and using the reflection coefficient as the following

$$\vec{E}_{TE}^{ref} = \mathrm{R}_{TE}E_{TE}^{inc}\vec{e}_{TE}, \tag{2.235}$$

$$\vec{H}_{TE}^{ref} = \frac{1}{\eta}\mathrm{R}_{TE}E_{TE}^{inc}\vec{s}_{TM} = \frac{1}{\eta}\mathrm{R}_{TE}E_{TE}^{inc}(\vec{k}_{ref} \times \vec{e}_{TE}). \tag{2.236}$$

As a result, the total fields for the TE components are:

$$\vec{E}_{TE}^{tot} = E_{TE}^{inc}(1 + R_{TE})\vec{e}_{TE}), \tag{2.237}$$

$$\vec{H}_{TE}^{tot} = \frac{1}{\eta}E_{TE}^{inc}[(\vec{k}^{inc} \times \vec{e}_{TE}) + R_{TE}(\vec{k}^{ref} \times \vec{e}_{TE})]. \tag{2.238}$$

2.10.3.2 TM Component

Fig. 2.27 shows the TM components of the incident, reflected, and transmitted fields. By following the same steps as for the TE components, the following equations are found for the total fields

$$\vec{E}_{TM}^{tot} = E_{TM}^{inc}[\vec{e}_{TM} + R_{TM}(\vec{k}^{ref} \times \vec{e}_{TE})], \tag{2.239}$$

$$\vec{H}_{TM}^{tot} = \frac{1}{\eta}E_{TM}^{inc}(1 - R_{TM})\vec{e}_{TE}. \tag{2.240}$$

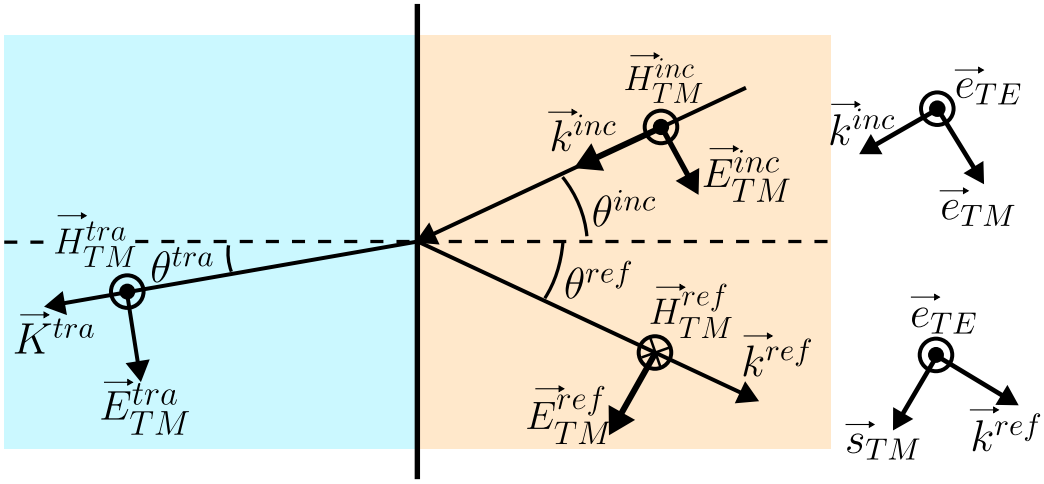

Figure 2.27: TM components of the field decomposition [5].

2.10.3.3 MECA Equivalent Currents

Combining the transverse electric and transverse magnetic components of the fields, the total electric and magnetic fields can be described as

$$\vec{E}^{tot} = \vec{E}^{inc} + R_{TE}E^{inc}_{TE}\vec{e}_{TE} + R_{TM}E^{inc}_{TM}(\vec{k}^{ref} \times \vec{e}_{TE}), \tag{2.241}$$

$$\vec{H}^{tot} = \frac{1}{\eta}\vec{k}^{inc} \times \vec{E}^{inc} + \frac{1}{\eta}[R_{TE}E^{inc}_{TE}(\vec{k}^{ref} \times \vec{e}_{TE}) - R_{TM}E^{inc}_{TM}\vec{e}_{TE}], \tag{2.242}$$

which, by considering the boundary conditions, leads to the equivalent electric and magnetic surface current densities using equations [5]

$$\begin{aligned}\vec{J}^{MECA} &= \vec{n} \times \vec{H}^{tot} \\ &= \frac{1}{\eta}\{E^{inc}_{TE}\cos\theta^{inc}(1 - R_{TE})\vec{e}_{TE} + E^{inc}_{TM}(1 - R_{TM})(\vec{n} \times \vec{e}_{TE})\},\end{aligned} \tag{2.243}$$

$$\begin{aligned}\vec{M}^{MECA} &= -\vec{n} \times \vec{E}^{tot} \\ &= \{E^{inc}_{TE}(1 + R_{TE})(\vec{e}_{TE} \times \vec{n}) + E^{inc}_{TM}\cos\theta^{inc}(1 + R_{TM})\vec{e}_{TE}\}.\end{aligned} \tag{2.244}$$

By referring to Fig. 2.28, the scattered electric and magnetic fields are given by:

$$\vec{E}^{s} \approx \frac{j}{2\lambda}\frac{\exp(-j\frac{2\pi}{\lambda}r)}{r}\iint_S [\vec{r} \times \vec{M}^{MECA} - (\vec{r} \times \eta\vec{J}^{MECA} \times \vec{r})]\exp(j\frac{2\pi}{\lambda}\vec{r}\cdot\vec{r'})dS, \tag{2.245}$$

$$\vec{H}^{s} \approx \frac{j}{2\lambda}\frac{\exp(-j\frac{2\pi}{\lambda}r)}{r}\iint_S [\vec{r} \times \vec{J}^{MECA} - (\vec{r} \times \vec{r} \times \frac{1}{\eta}\vec{M}^{MECA})]\exp(j\frac{2\pi}{\lambda}\vec{r}\cdot\vec{r'})dS, \tag{2.246}$$

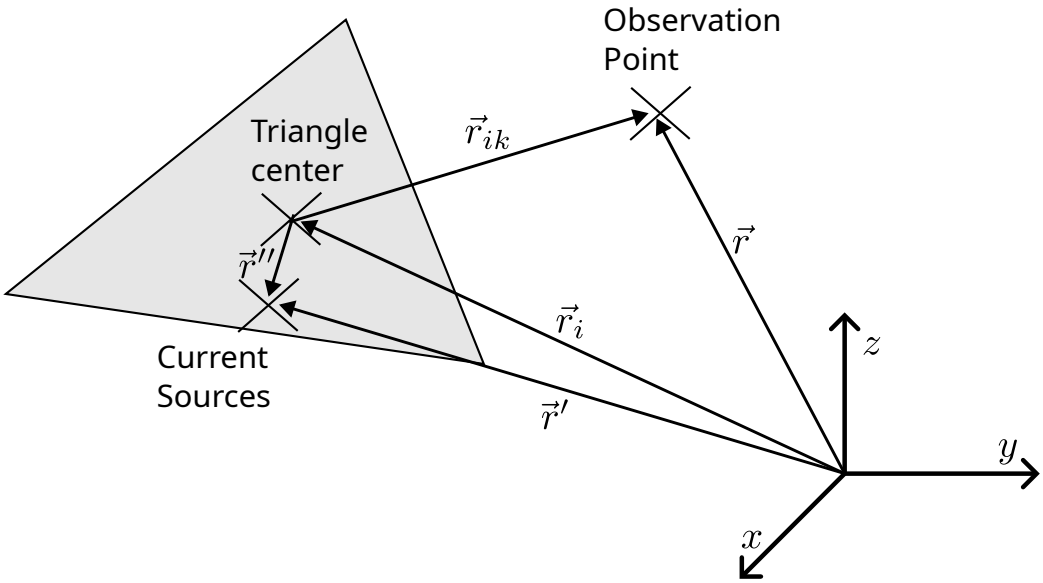

Figure 2.28: The coordinate system and vectors for calculating the scattered fields from a triangle [5].

and these equations can be simplified by using the auxiliary vectors $\vec{E}^a$ and $\vec{H}^a$ as formulated by

$$\vec{E}^s \approx \frac{j}{2\lambda}\frac{\exp(-j\frac{2\pi}{\lambda}r)}{r}[\vec{E}^a - \eta\vec{H}^a \times \vec{r}], \tag{2.247}$$

$$\vec{H}^s \approx \frac{j}{2\lambda}\frac{\exp(-j\frac{2\pi}{\lambda}r)}{r}[\vec{H}^a - \frac{1}{\eta}\vec{r} \times \vec{E}^a], \tag{2.248}$$

where

$$\vec{E}^a = \iint_S \vec{r} \times \vec{M}^{MECA} \exp\{j\frac{2\pi}{\lambda}\vec{r}\cdot\vec{r'}\}dS, \tag{2.249}$$

$$\vec{H}^a = \iint_S \vec{r} \times \vec{J}^{MECA} \exp\{j\frac{2\pi}{\lambda}\vec{r}\cdot\vec{r'}\}dS. \tag{2.250}$$

Since the equations for $\vec{E}^a$ and $\vec{H}^a$ are similar, the equation for $\vec{H}^a$ will be further simplified. The equivalent surface current densities $\vec{J}$ and $\vec{M}$ can be assumed to have a constant amplitude on the triangle as calculated at its center, and linear phase difference as given by the equations

$$\vec{J}^{MECA} = \vec{J}_0^{MECA} \exp(j\frac{2\pi}{\lambda}\vec{p}\cdot\vec{r''}), \tag{2.251}$$

$$\vec{M}^{MECA} = \vec{M}_0^{MECA} \exp(j\frac{2\pi}{\lambda}\vec{p}\cdot\vec{r''}), \tag{2.252}$$

where $\vec{p}$ is the direction of propagation of the EM waves or the Poynting vector described by the equation

$$\vec{p} = \frac{\mathcal{R}\{\frac{1}{2}\vec{E}^{inc} \times (\vec{H}^{inc})^*\}}{|\mathcal{R}\{\frac{1}{2}\vec{E}^{inc} \times (\vec{H}^{inc})^*\}|}, \tag{2.253}$$

and $\vec{P}$ can be substituted by $\vec{r}_i$ because of approximating the wave by plane waves in the direction of the center of the triangle. Therefore, the contribution due to the electric current J on the i-th facet is calculated by

$$\vec{H}^a_{ik} = \exp\{j\frac{2\pi}{\lambda}\vec{r}_{ik} \cdot \vec{r}_i\} \iint_S (\vec{r}_{ik} \times \vec{J}^{MECA}) \exp\{j\frac{2\pi}{\lambda}\vec{r}_{ik} \cdot \vec{r}\,''\} dS, \tag{2.254}$$

which can be written in the following form, taking into consideration the linear phase variation

$$\vec{H}^a_{ik} = \exp\{j\frac{2\pi}{\lambda}\vec{r}_{ik} \cdot \vec{r}_i\}(\vec{r}_{ik} \times \vec{J}^{MECA}_0) I(\vec{r}_{ik}), \tag{2.255}$$

$$I(\vec{r}_{ik}) = \iint_S \exp\{j\frac{2\pi}{\lambda}(\vec{r} - \vec{p}) \cdot \vec{r}\,''\} dS. \tag{2.256}$$

When handling flat facets with triangular shape, $\vec{r}\,''$ can be written based on the vectors $\vec{v}_{mn}$ as

$$\vec{r}\,'' = \vec{v}_{01} + f\vec{v}_{12} + g\vec{v}_{13}, \tag{2.257}$$

where $\vec{v}_{mn} = \vec{P}_n - \vec{P}_m$, considering $\vec{P}_l$ as the position vector of the vertices of the triangle when $l = 1, 2, 3$, and the barycenter when $l = 0$. Variables f and g are real coefficients. The nomenclature is shown in fig.2.29

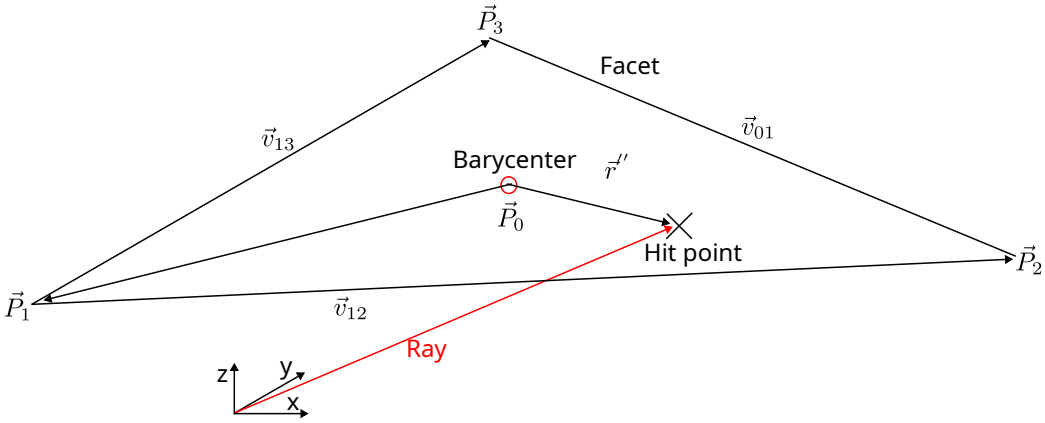

Figure 2.29: The facet, its barycenter, and the edge vectors.

Using this transformation, the integral can be written as

$$I(\vec{r}) = 2A\exp\{-j\frac{a+b}{3}\}\int_0^1\int_0^{1-f}\exp\{j(af+bg)\}dgdf, \tag{2.258}$$

where A is the facet surface area, and a and b is given by:

$$a = \frac{2\pi}{\lambda}\vec{v}_{12}\cdot(\vec{r}-\vec{p}_i), \tag{2.259}$$

$$b = \frac{2\pi}{\lambda}\vec{v}_{13}\cdot(\vec{r}-\vec{p}_i). \tag{2.260}$$

To avoid some singularities, the integral is given by one of the cases in table 2.3.

Table 2.3: All Equations For the Integral $I(\vec{r})$.

a	b	$I(\vec{r})$
Any	Any	$2A\exp\{-j\frac{a+b}{3}[\frac{a\exp\{jb\}-b\exp\{ja\}+b-a}{(a-b)ab}]\}$
0	Any	$2A\exp\{-j\frac{b}{3}\}[\frac{1+jb-\exp\{jb\}}{b^2}]$
Any	0	$2A\exp\{-j\frac{a}{3}\}[\frac{1+ja-\exp\{ja\}}{a^2}]$
Any	a	$2A\exp\{-j\frac{2a}{3}\}[\frac{\exp\{ja\}(1-ja)-1}{a^2}]$
0	0	A

2.11 Ray-Tracing

When using the method of GO, the propagation of the electromagnetic waves is modeled by rays, and these rays hit the objects in space and bounce off them. One task when performing this ray-tracing is finding the hitting point between the ray and the object. Because of dealing with objects consisting of flat triangles,

ray-triangle hit tests need to be performed to find out whether the ray hit the triangle or not and the hitting point. The following section describes the method used for the ray-triangle intersection.

2.11.1 Ray-Triangle Intersection Test

In this section, the used method is described, which is described by Tomas Möller and Ben Trumbore in [6]. First, a ray with origin O and direction D is described by the equation

$$R(t) = O + tD, \tag{2.261}$$

where t is the distance between the origin O and the point R(t) in the direction of the ray. Three vertices V_0, V_1, and V_2 define the triangle. A point, $T(u, v)$ on a triangle is found using the barycentric coordinate (U, v) using the equation

$$T(u, v) = (1 - u - v)V_0 + uV_1 + vV_2, \tag{2.262}$$

where (u, v) must satisfy $u \geq 0$, $v \geq 0$, and $u + v \leq 1$. Finding the intersection between the ray and the triangle is done by $R(t) = T(u, v)$, which gives the equation

$$O + tD = (1 - u - v)V_0 + uV_1 + vV_2. \tag{2.263}$$

By rearranging, the following is obtained

$$[-D, V_1 - V_0, V_2 - V_0] \begin{bmatrix} t \\ u \\ v \end{bmatrix} = O - V_0, \tag{2.264}$$

which means that the coordinates $[t, v, u]$ can be found by solving this linear system of equations. For insight, we can think of that equation as first, moving the triangle so that V_0 is on the origin, and second, converting the triangle into a unit triangle in (y, z) and the direction of the ray is aligned with x, so the new coordinate system is $[t, u, v]$ which is illustrated in Fig. 2.30 By setting the following equations

$$E_1 = V_1 - V_0, \tag{2.265}$$
$$E_2 = V - 2 - V_0, \tag{2.266}$$
$$T = O - V_0. \tag{2.267}$$

The solution can be obtained using Cramer's rule as

$$\begin{bmatrix} t \\ u \\ v \end{bmatrix} = \frac{1}{|-D, E_1, E_2|} \begin{bmatrix} |T, E_1, E_2| \\ |-D, T, E_2| \\ |-D, E_1, T| \end{bmatrix}. \tag{2.268}$$

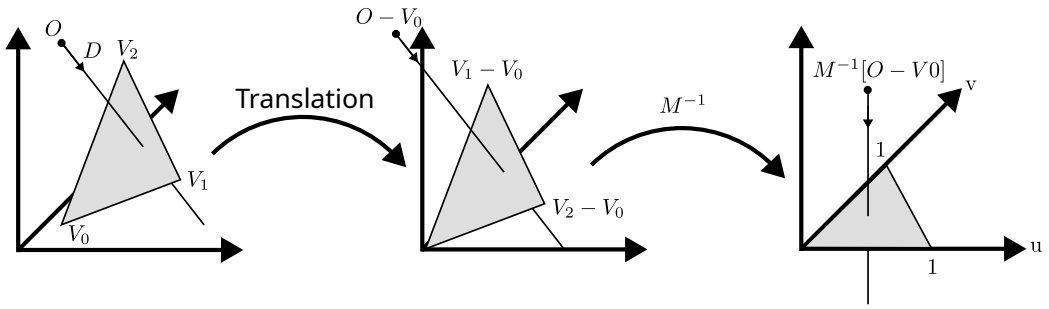

Figure 2.30: Transformation of the triangle and the ray to the u-v coordinates [6].

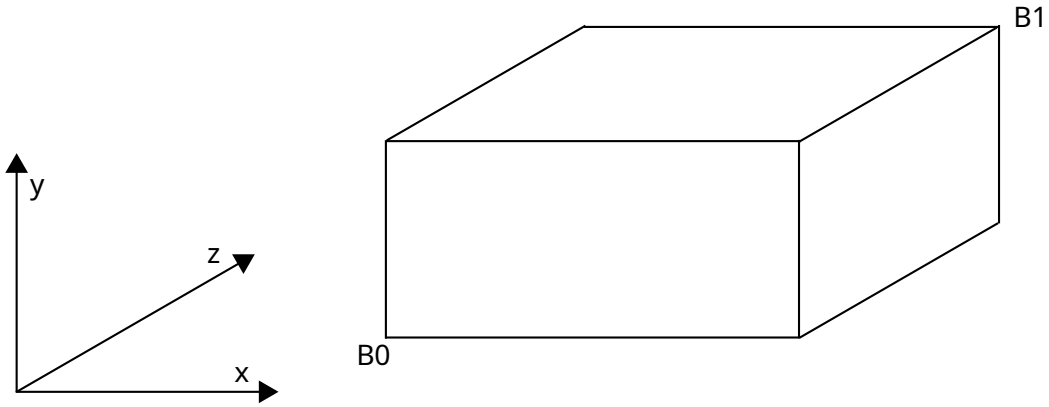

Figure 2.31: Axis aligned bounding box (AABB).

From linear algebra, it is known that

$$|A, B, C| = -(A \times C) \cdot B = -(C \times B) \cdot A. \tag{2.269}$$

Therefore, the previous equation (solution) can be written as

$$\begin{bmatrix} t \\ u \\ v \end{bmatrix} = \frac{1}{(D \times E_2) \cdot E_1} \begin{bmatrix} (T \times E_1) \cdot E_2 \\ (D \times E_2) \cdot T \\ (T \times E_1) \cdot D \end{bmatrix} = \frac{1}{P \cdot E_1} \begin{bmatrix} Q \cdot E_2 \\ P \cdot T \\ Q \cdot D \end{bmatrix}, \tag{2.270}$$

where $P = (D \times E_2)$ and $Q = T \times E_1$.

2.11.2 Ray-Box Intersection

To find whether a ray hit an object or not, first, it should be tested whether the ray intersects the object's bounding box because it is much faster to test this property. The bounding box is oriented along the coordinate axes. Thus, it is named the axis-aligned bounding box or (AABB) as shown in Fig.

. The box is defined by two points, $B0, B1$, that determine its minimum and maximum in the three directions. There are six planes that confine the box. First, the intersections of the ray and these planes are found, and then it should be examined whether the intersections are within the faces of the box or not. For instance, the plane that is parallel to the yz plane and passes through the first defining point is

$$x = B_{0x}. \tag{2.271}$$

To find the intersection between this plane and the ray, we substitute this equation in the x component of the ray equation, which gives

$$O_x + tD_x = B_{0x}, \tag{2.272}$$

and solving for t yields

$$t_{0x} = \frac{B_{0x} - O_x}{D_x}. \tag{2.273}$$

Solving for the six planes gives six equations as in the following

$$t_{0x} = \frac{B_{0x} - O_x}{D_x}, \tag{2.274}$$

$$t_{1x} = \frac{B_{1x} - O_x}{D_x}, \tag{2.275}$$

$$t_{0y} = \frac{B_{0y} - O_y}{D_y}, \tag{2.276}$$

$$t_{1y} = \frac{B_{1y} - O_y}{D_y}, \tag{2.277}$$

$$t_{0z} = \frac{B_{0z} - O_z}{D_z}, \tag{2.278}$$

$$t_{1z} = \frac{B_{1z} - O_z}{D_z}. \tag{2.279}$$

Now, to find whether the ray intersects the box, the logic will be shown in 2D first, then in 3D.

Fig. 2.32 illustrates the two cases of hitting and missing the box. In (b), two cases can be seen where the ray misses the box. This occurs when the following condition is satisfied:

```
if(t0x>t1y || t0y>t1x) return false
```

And then t_{min} and t_{max} are calculated, which are the closest and farthest intersection points, respectively, using the following pseudo-code

```
tmin = (t0x > t0y)? t0x : t0y
tmax = (t1x < t1y)? t1x : t1y
```

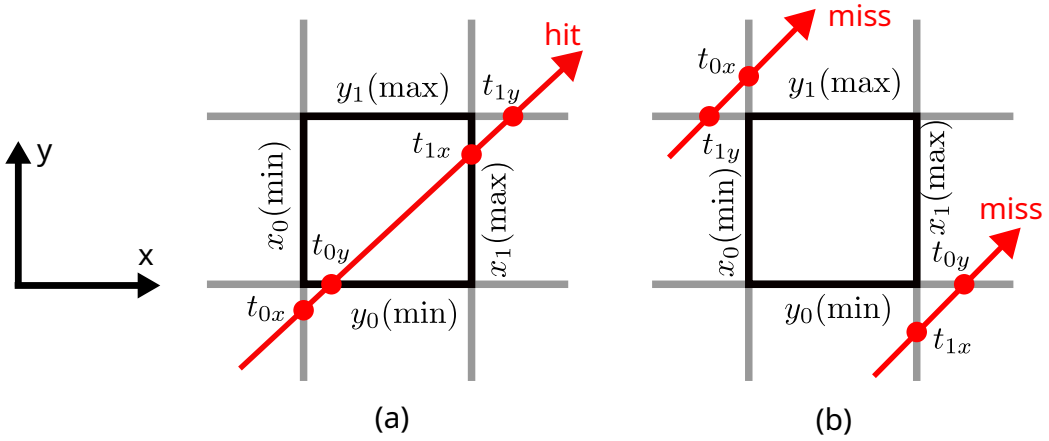

Figure 2.32: Ray-Box intersection test. Ray hits the box in (a), and misses the box in (b) [7].

which means t_{min} is set to t_{0x} if it is greater that t_{0y}, otherwise it is set to t_{0y} instead, in other words, the farthest of t_{0x} and t_{0y} to the ray's origin is taken. For t_{max} the opposite is done, so the closest of t_{1x} and t_{1y} is taken to be t_{max}. Then the z-axis is examined to see if the ray misses the box, and that occurs when the following condition is fulfilled

```
if(tmin > t1z || t0z > tmax) return false
```

If the above condition is not met, it is known that the ray intersects the box, so true is returned. Two illustrate these two cases in 3D, and a figure is shown for each case. The first condition ($t_{min} > t_{1z}$) occurs when the ray passes behind the box without intersecting it, as shown in Fig. 2.33. It is visible that the ray intersects xy planes (z=constant) before intersecting the other planes, which means that tmin (the farthest of t_{0x} and t_{0y} from the ray's origin) is farther from the origin of the ray than t_{1z}, satisfying the mentioned condition.

For the second condition ($t_{0z} > t_{max}$), Fig. 2.34 is shown, where it is clear that the ray passes in front of the box not through it. It can be seen that the ray passes through the first xy plane (z=constant) after passing through all the other planes, which means that the condition is fulfilled. The final case is where the ray passes through the box. It occurs when both previous conditions are not met or the opposite condition is met ($t_{min} < t_{1z}$ && $t_{0z} < t_{max}$). Fig. 2.35 illustrates this case. In this figure, it is clear that t_{1z} is farther than t_{min} and that t_{0z} is closer than t_{max} with respect to the ray's origin.

Finally, t_{min} and t_{max} are chosen using the following code

```
if (t0z > tmin) tmin=t0z
if (t1z < tmax) tmax=t1z
```

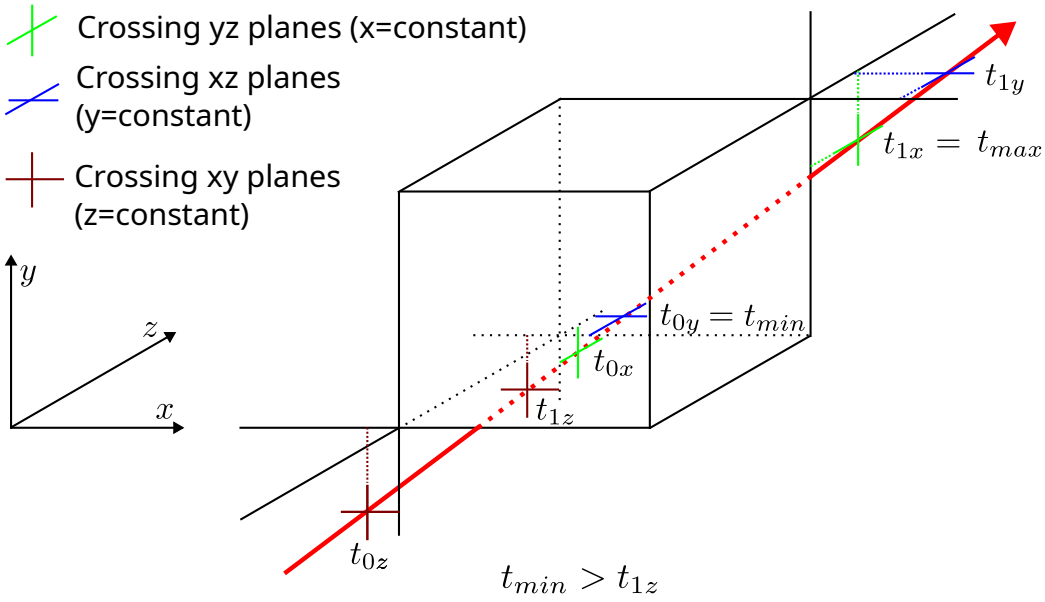

Figure 2.33: Ray-Box intersection test. Ray passes behind the box in z axis.

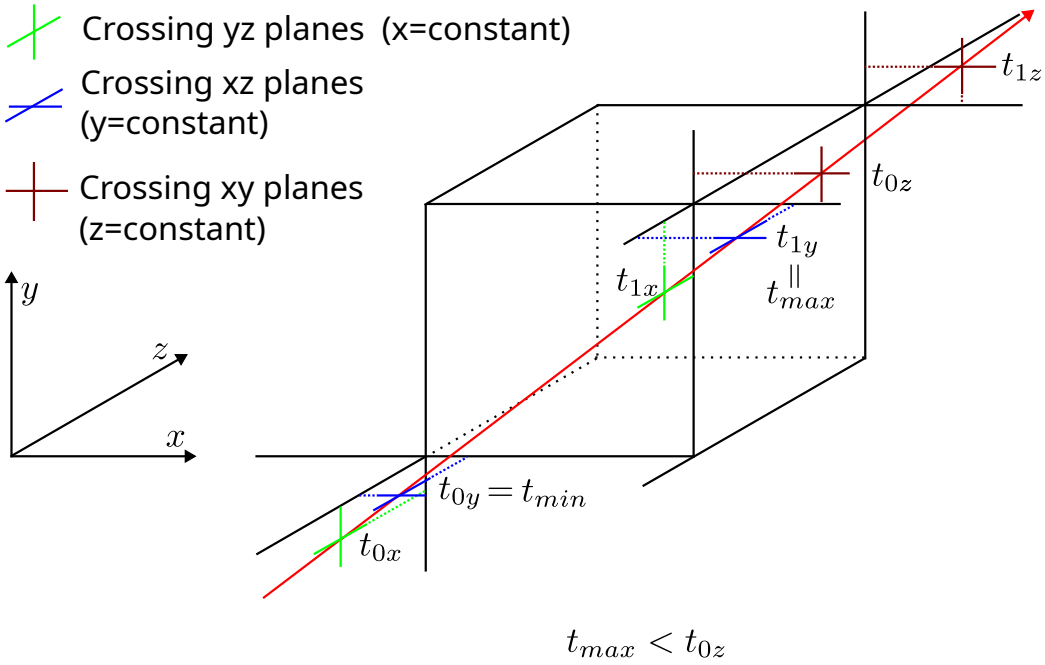

Figure 2.34: Ray-Box intersection test. Ray passes in front of the box in z axis.

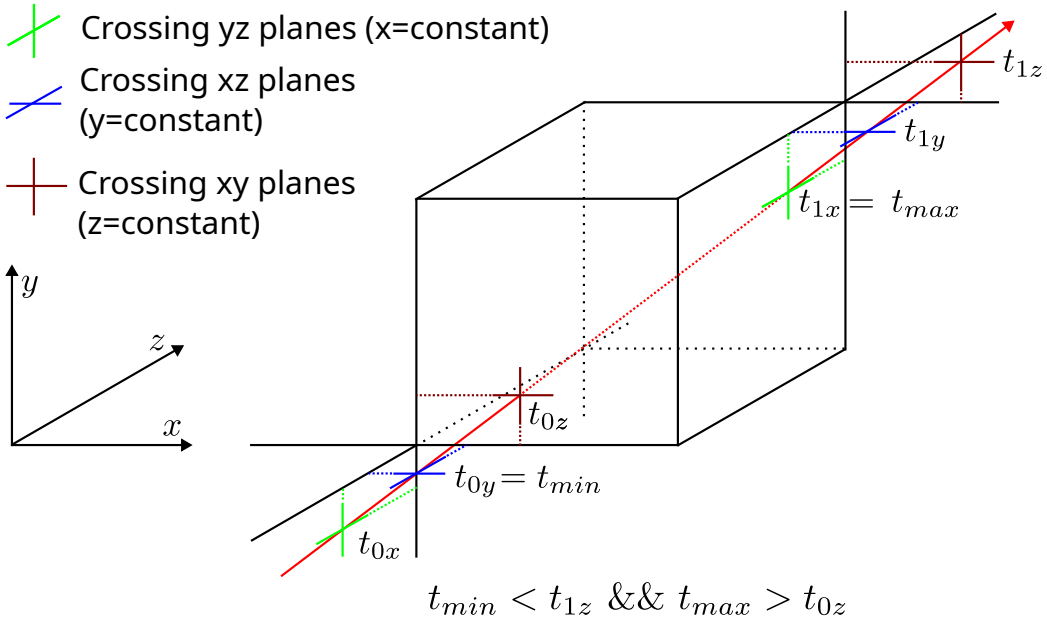

Figure 2.35: Ray-Box intersection test. Ray passes through the box.

which, like in the xy case, means that we choose the farthest of (t_{0x}, t_{0y}, t_{0z}) to be t_{min}, and the closest of (t_{1x}, t_{1y}, t_{1z}) to be t_{max}, both with respect to the ray's origin.

2.11.3 Triangle-Box Overlap

Later, the acceleration structure used to speed up the ray-tracing process will be discussed. One function needed to build the KD-tree (K-dimensional tree) (used acceleration structure) is the Triangle-Box overlap test. The algorithm is based on the separating axis theorem (SAT) [8]. According to this theorem, when dealing with two convex polyhedra, denoted as A and B, they are considered non-intersecting if it is possible to create a gap between them along one of two types of axes. The first type is an axis parallel to a normal vector of a face from either A or B. The second type involves an axis formed by taking the cross-product of an edge from A and an edge from B. The case of an axis-aligned bounding box (AABB) is examined, determined by a center c, and a vector of half lengths, h, with a triangle $\Delta(u_0, u_1, u_2)$. For simplicity, first, the objects are transformed such that the center of the box is at the origin, as shown in Fig. 2.36. When the box is oriented (not axis-aligned), first, the objects are transformed such that the box is axis-aligned, then continue. Now, the test should be performed along 13 axes as follows:

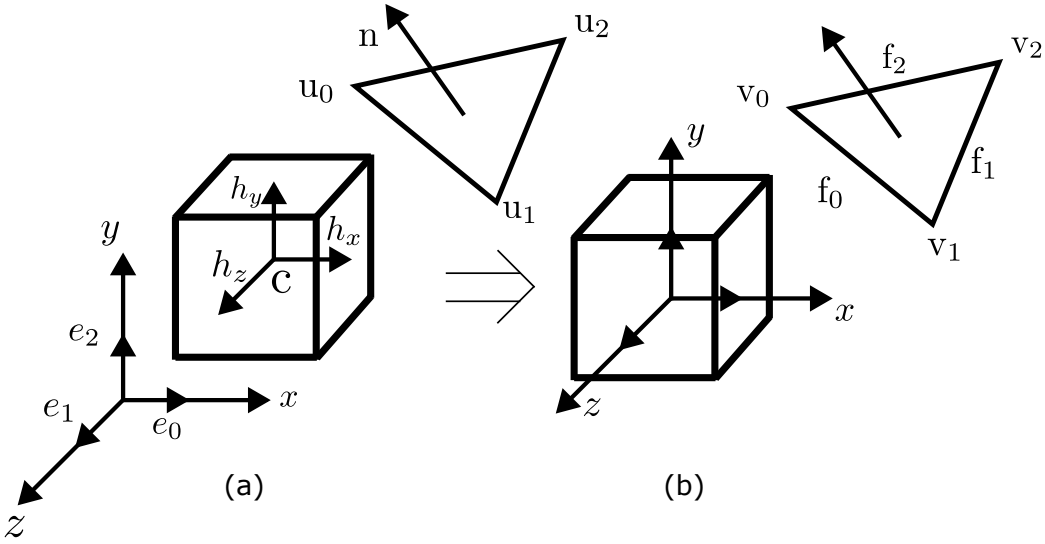

Figure 2.36: Box-Triangle overlap test. In (a), the box is in its original location, and in (b), the center of the box is aligned with the coordinate origin [8].

- test along three normals of the AABB ($e_0 = (1,0,0)$, $e_1 = (0,1,0)$, $e_2 = (0,0,1)$). Test against the smallest AABB bounding the triangle.
- test along n, the normal of the triangle. Possible to use the AABB-plane overlap test [9] [10], which tests the two diagonal vertices that most aligned to the normal
- Test along the 9 directions defined by $a_{ij} = e_i \times f_j$, where $i, j \in \{0,1,2\}$

One of the nine tests where $i = 0$ and $j = 0$ will be illustrated. In this case, the following equation results

$$a_{00} = e_0 \times f_0 = (0, -f_{0z}, f_{0y}). \tag{2.280}$$

Now the triangle vertices will be projected onto a_{00} (from now on it is called a):

$$p_0 = a \cdot \mathrm{v}_0 = (0, -f_{0z}, f_{0y}) \cdot \mathrm{v}_0 = v_{0z}v_{1y} - v_{0y}v_{1z}, \tag{2.281}$$
$$p_1 = a \cdot \mathrm{v}_1 = (0, -f_{0z}, f_{0y}) \cdot \mathrm{v}_1 = v_{0z}v_{1y} - v_{0y}v_{1z} = p_0, \tag{2.282}$$
$$p_2 = a \cdot \mathrm{v}_2 = (0, -f_{0z}, f_{0y}) \cdot \mathrm{v}_2 = (v_{1y} - v_{0y})v_{2z} - (v_{1z} - v_{0z})v_{2y}. \tag{2.283}$$

Now the box needs to be projected onto ”a” as well, and a ”radius” r is computed using

$$r = h_x|a_x| + h_y|a_y| + h_z|a_z| = h_y|a_y| + h_z|a_z|. \tag{2.284}$$

Finally, the test for this axis is given by

```
if(min(p0,p2)>r or max(p0,p2)<-r) return false;
```

and at the end, if all the 13 tests pass without finding a separating plane, then the triangle overlaps the box

2.11.4 Acceleration Structure (KD-Tree)

When performing ray tracing, the intersection between a ray and an object in the scene needs to be found. The simplest way to find it is to test the ray against all the triangles in the object to find out whether it intersects one or more triangles, where the closest intersection to be the point of intersection with the object is selected. However, this needs to be done for every ray, which is very time-consuming, so this method is inefficient. The other approach is to use what is called ”accelerating structures,” which the ray can traverse to limit the number of ray-triangle intersection tests to the lowest possible. One of these structures is the so-called KD-Tree or the k-dimensional tree. A KD-tree is a binary tree where each node represents an axis-aligned cell in the k-dimensional space. Each cell is divided into two cells along a chosen axis each time. The parent node is connected then to two child nodes. When the chosen criteria are met, the node becomes a leaf, which holds the triangles overlapping it. Such a criterion could be the number of triangles it overlaps, the depth of the node, or other criteria. Fig. 2.37 shows space division in 2D for simplicity, and Fig. 2.38 shows a diagram of a KD-Tree where the red circles are nodes, and the green rectangles are leaves holding the blue triangles, which are the mesh triangles that this KD-Tree contains. The two figures are for the same structure. The first red node is for the whole scene (bounding box), which is split into two cells. The left cell is split into two leaves holding three and one triangle. The right cell is split into two cells: the left is a normal cell, which is further split, and the right cell is a leaf holding two triangles. The construction of the KD-Tree starts by assigning the whole scene to the root node, which is the axis-aligned bounding box to the entire scene. From that, we start subdividing the root node into child nodes and assign to each one the triangles that overlap with each one. The algorithm is outlined as follows [11]

- Find a plane P to split the current cell V. There are sophisticated algorithms like the surface heuristic approach [11], but here, for simplicity, a simple algorithm is used, which is to select the axis along which the bounding box has the longest edge, and split it in the middle into two equal bounding boxes.

- Find the overlapping triangles with each resulting cell and assign them to it.

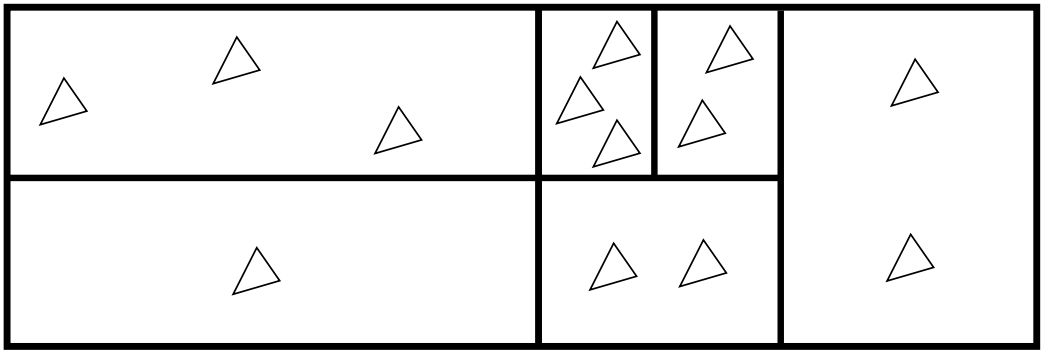

Figure 2.37: Illustration of a KD-Tree in 2D.

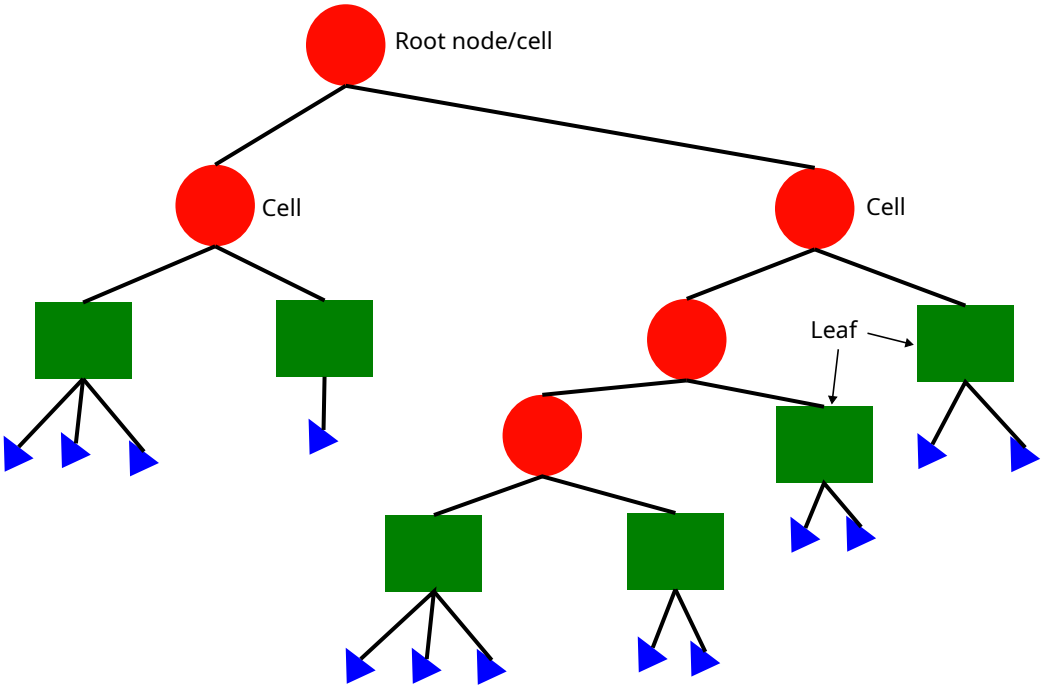

Figure 2.38: Diagram of a KD-Tree. The red circles are the nodes, the green rectangles are the leaves, and the blue triangles are the contained mesh triangles.

- If the cell achieves leaf criteria, it is flagged as a leaf.
- If the cell does not meet leaf criteria, the process is repeated until all cells are leaves, and a pointer to the root node (the head node) is returned.

Now, the problematic part of the algorithm is to find the best plane P to split V. There are sophisticated algorithms like the surface heuristic approach [11], but here, for simplicity, a simple algorithm is used, which is to select the axis along which the bounding box has the longest edge, and split it in the middle into two equal bounding boxes.

2.11.5 Traversing the KD-Tree

The next step in ray-tracing a scene is traversing a KD-Tree. There are several traversal algorithms, like the sequential algorithm, which is the simplest, and the recursive stack-based one [12]. In this work, the simple sequential algorithm will be used. The algorithm proceeds in the following steps:

- Intersection test is performed between the ray and the bounding box (AABB) that contains all the objects in the scene because if it does not intersect the box, then it will not intersect any object, and we can immediately return false, saving computation time. The function returns entry and exit points between which the test for object intersections is done.
- In this step, the first leaf the ray passes through is found (leaf location). There are two cases for this:
  - The origin of the ray is inside the bounding box. In this case, the leaf containing the origin is found to start with.
  - If the origin is outside the box, an entry point to it is returned from the previous step. The point is moved a slight shift along the ray to be inside the bounding box, and the leaf containing it is found.
- A test for intersection is performed with all the triangles overlapping the leaf cell. If there is an intersection, then a check for validity is done by examining whether the intersection point is inside the current leaf or not. The reason for this is explained later. If there is a valid intersection, true is returned.
- If there is no valid intersection, the algorithm proceeds to the next leaf in two steps. First, the exit point of the leaf is found. Then, the point is moved by a small distance, and the next leaf containing it is found.

- The procedure is continued in the same manner until a valid intersection is found or the next point is outside the bounding box, in which case, there is no valid intersection, and false is returned.

The reason why a test is done for the intersection point to check whether it is in the current leaf or not is illustrated in Fig. 2.39. As can be seen, ray 1 intersects cell one, which is overlapping with triangle 1 (Tr1), so an intersection test is performed, which returns true since the ray intersects it in intersection point 2 (I2). But, as can be seen, this point is located in cell 2, and the ray intersects triangle 2 at I1, which lies on the ray closer to the origin, which means it is the valid intersection, and I2 is not valid. In comparison, ray 2 intersects Tr1 at I3, which lies inside cell 1, so this is a valid intersection. As an illustration of the previous

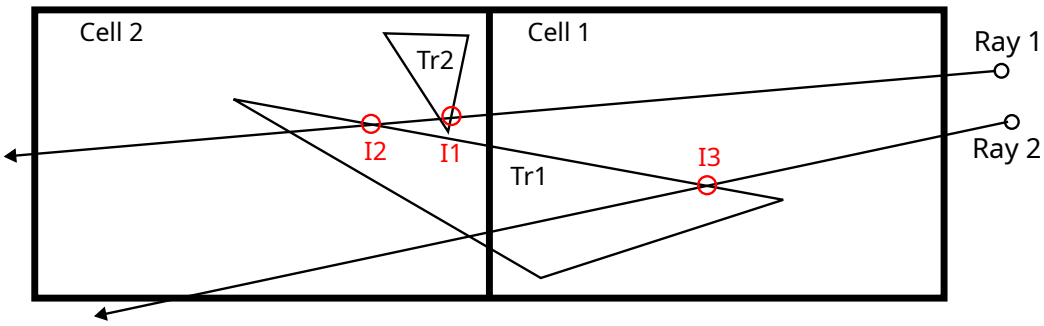

Figure 2.39: Illustration of the reason why the intersection should be inside the cell to be valid.

procedure, Fig. 2.40 shows examples of two rays intersecting the bounding box. The first ray starts outside the bounding box; thus, at first, the intersection with the bounding box is checked, and the entry and exit points are returned. Then the entry point is moved a slight shift along the ray, and the leaf is found, which is here Cell 1. Next, an intersection test is done with all the triangles in the cell (Tr1 and Tr2), and the intersection is returned with Tr1, which, by examining, is inside cell 1, so the intersection is valid and true is returned. On the other hand, ray 2 starts inside the bounding box, and by locating the origin, it is found that cell 2 is the first leaf to start with. So, an intersection test is performed with the triangle in this cell, and false is returned since it does not intersect it as shown. Therefore, the procedure proceeds by finding the exit point from the leaf, and by moving it a small distance along the ray, the next leaf is located, which is cell 3. Subsequently, all triangles (two here) are tested, and an intersection is found with Tr4, which lies inside cell 3, so it is valid, and true is returned.

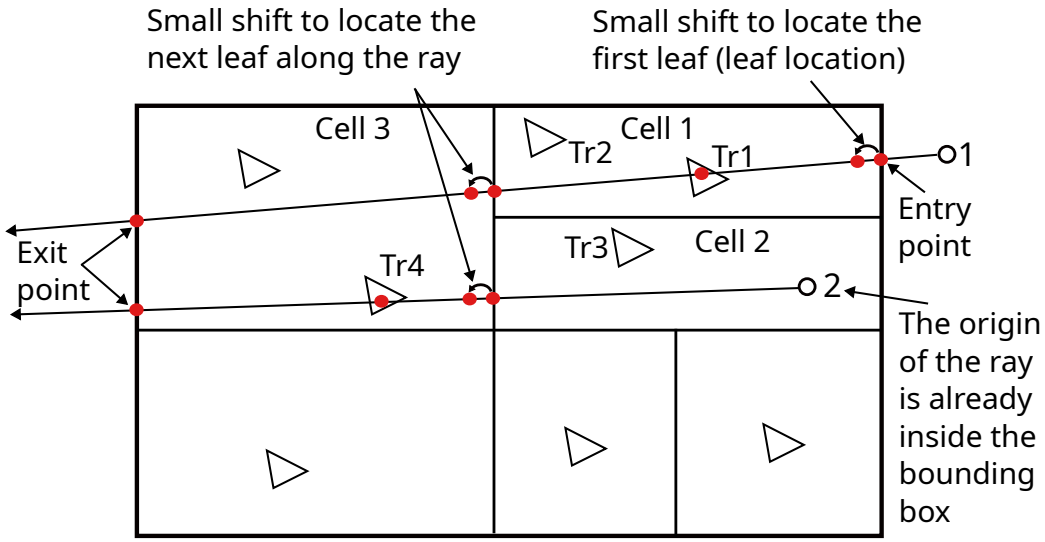

Figure 2.40: Illustration of the algorithm for finding ray-object intersection.

2.12 Curves and Curvature

A parametrized curve in R^n is defined as a map $\gamma(t) \ : \ R \rightarrow R^n$ [13]. For instance, in R^2, it is defined as

$$\vec{\gamma}(t) = (\gamma_1(t), \gamma_2(t)) \tag{2.285}$$

Fig.2.41 shows an example of a parametric curve in 2 dimensions.

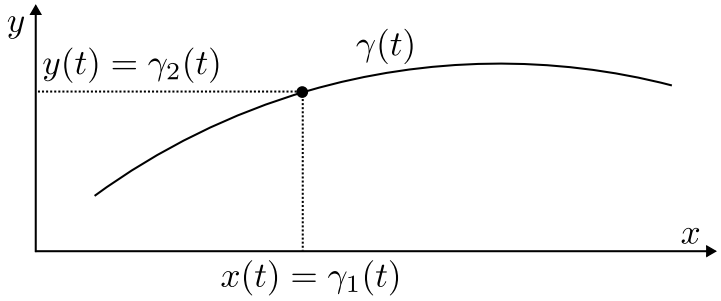

Figure 2.41: A curve $\vec{\gamma}(t)$ in 2 dimensions.

2.12.1 Tangent Vector

The first derivative of the curve $\vec{\gamma}'(t)$ is the tangent vector of $\gamma(t)$.

2.12.2 Arc-Length

The arc-length of a curve $\vec{\gamma}(t)$ between two points t_0 and t is defined by [13]

$$s(t) = \int_{t0}^{t} ||\vec{\gamma}'(u)||du. \tag{2.286}$$

2.12.3 Unit-Speed Curve

The speed of a curve is defined as $||\vec{\gamma}'(t)||$, and a unit speed curve is a curve with speed = 1.

2.12.4 Curvature of a Curve

The curvature of a curved line at a point $\gamma(t)$ is determined by its deviation from its tangent line at that point. To measure it, we assume the curve is a unit speed curve, then when t changes to $t + \Delta t$, $\gamma(t)$ changes to $\gamma(t + \Delta t)$, and the deviation from the tangent line will be [13]

$$(\vec{\gamma}(t + \Delta t) - \vec{\gamma}(t)) \cdot \vec{n}, \tag{2.287}$$

where n is a normalized vector orthogonal to the tangent vector $\vec{\gamma}'(t)$ as depicted in fig.2.42

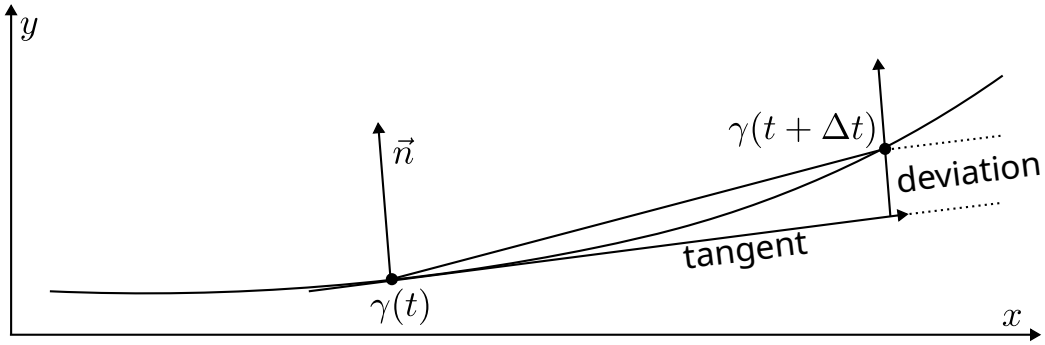

Figure 2.42: The curvature of a curve as the deviation from the tangent line.

Using Taylor's theorem:

$$\vec{\gamma}(t + \Delta t) - \vec{\gamma}(t) = \vec{\gamma}'(t)\Delta t + \frac{1}{2}\vec{\gamma}''(t)(\Delta t)^2 + \text{reminder}. \tag{2.288}$$

Therefore, the deviation from the tangent line is (ignoring higher order terms):

$$\frac{1}{2}\vec{\gamma}''(t)(\Delta t)^2. \tag{2.289}$$

This leads to the definition of the curvature for a unit-speed curve as the following:

2.12.4.1 The Curvature of a Unit-Speed Curve

The curvature κ at the point $\vec{\gamma}(t)$ along a unit-speed parametrized curve is [13]

$$\kappa = ||\vec{\gamma}''(t)||.$$

2.12.4.2 The Curvature of a General Regular Curve

The curvature of a general (not unit-speed) curve is defined by the following equation [13]:

$$\kappa = \frac{||\vec{\gamma}'' \times \vec{\gamma}'||}{||\vec{\gamma}'||^3} \tag{2.290}$$

2.13 Conclusion

In this chapter, the main background theory behind the work is presented. Additionally, the main algorithms required to perform ray-tracing simulations are outlined, which include the following algorithms:

- Ray-triangle intersection test.
- Ray-box intersection test.
- Triangle-box overlap
- Building the used acceleration structure (KD-tree)
- Traversing the KD-tree

Then, the main concepts behind curvature handling are presented. Starting in the next chapter, the main work and results will be presented.

Chapter 3

Simulation for Machine Learning

Radar is increasingly used in the automotive industry for environment perception due to its advantageous capabilities in several conditions [14]. Developing radar algorithms requires a large amount of data for tuning and model training, especially when employing machine learning techniques. To generate this data at a lower cost, simulation methods are used to create driving scenarios and simulate them efficiently. Several simulation methodologies can be used, like the full wave based finite element method (FEM), the method of moments (MOM), and asymptotic techniques like the shooting and bouncing rays method (SBR). The FEM and MOM are considered full-wave methods, and they are based on Maxwell's equations with mathematical convergence results. But this means that they are also prohibitively time-consuming when dealing with electrically large targets in terms of wavelengths. Therefore, when simulating automotive scenarios, only asymptotic methods will be considered. Namely, SBR, physical optics (PO), and the ray launching geometrical optics method (RLGO).

3.1 Testing Available Tools

As a first step to perform a simulation for data generation, the available tools were tested to see if one of them at least meets the required conditions, which are speed and accuracy. The tested tools are:

1. The simulation tool HFSS from ANSYS using the method SBR+(shooting and bouncing rays plus) [15] as implemented in commercial simulation tools, which is a modified algorithm from the method of SBR [16]. The original method handles objects with cavities and collects the rays at the aperture (opening) of the cavity, where it calculates the back-scattered fields using the method of physical optics (PO). The modified method, on the other hand, handles arbitrary objects in a similar way to [17], where

equivalent current densities are painted on the surface of the object and then used to calculate the scattered field at the receiver. The geometrical optics principles are used to extend this algorithm to multiple reflections on the object's surface or between objects.

2. The simulation tool FEKO from Altair [18], using the following methods:
   - Physical Optics (PO)(2.8.8)
   - Large element PO (LE-PO), which is similar to PO but allows larger mesh triangles to be used.
   - Ray Launching Geometrical Optics (RLGO), which is a ray-based method suitable for electrically large objects, utilizing the method SBR to account for multiple reflections efficiently.
3. The simulation tool Wavefarer from Remcom [19], using the methods SBR, PO, geometrical optics (GO), and the Uniform Theory of Diffraction (UTD). GO and UTD methods are used to calculate the incident field at a scattering point after being reflected by nearby surfaces from objects and the ground (GO for small objects and UTD for large, smooth/flat ones).
4. Mathematical model in Matlab for comparison

3.1.1 Test Cases

For testing our tools, two cases are considered: a metal sphere shown in Fig. 3.1 and a metal cylinder as shown in Fig. 3.2.

For the sphere case, the corresponding theoretical model is a point scattering center with two rays, direct and indirect, forming the four paths model: direct-direct, direct-indirect, indirect-direct, and indirect-indirect. In the case of the cylinder, it is modeled with two rays as well; one reflects specularly only, and one reflects off the bottom corner with the ground, forming the indirect path. This is modeled as two-point scattering centers, one at the same height as the antenna and one on the bottom, as seen in the figure.

3.1.2 Simulation Methodology

The material of the road is modeled as a perfect electric conductor (PEC) or as Asphalt (dielectric layer with a dielectric constant of 4 [20]). The road itself is modeled in one of three ways:

1. Modeled as an actual layer, which gets meshed and takes part in the simulation

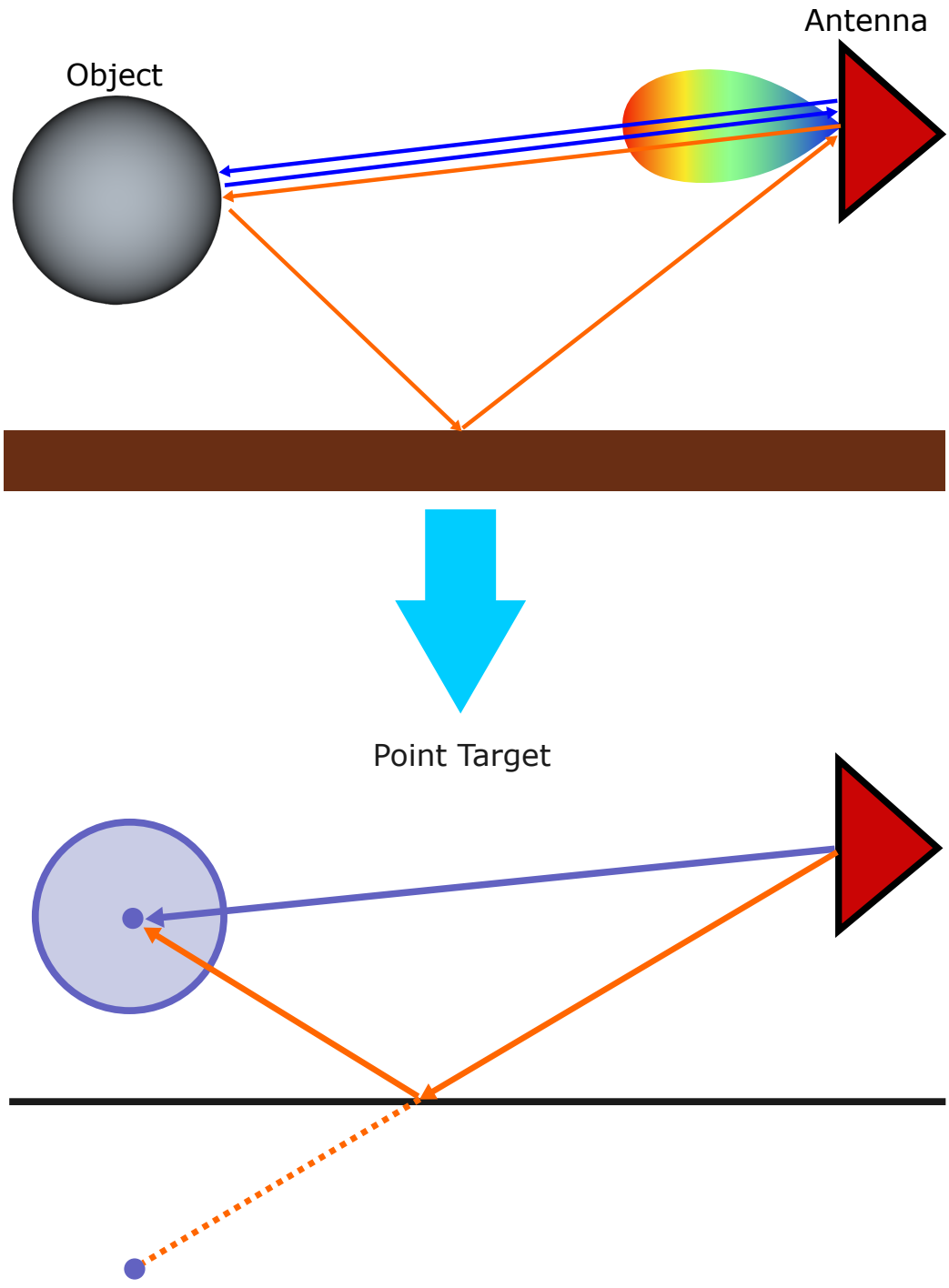

Figure 3.1: Sphere test case for the simulation tools. On the upper side is the simulation model, and on the lower side is the corresponding theoretical model for Matlab modeling.

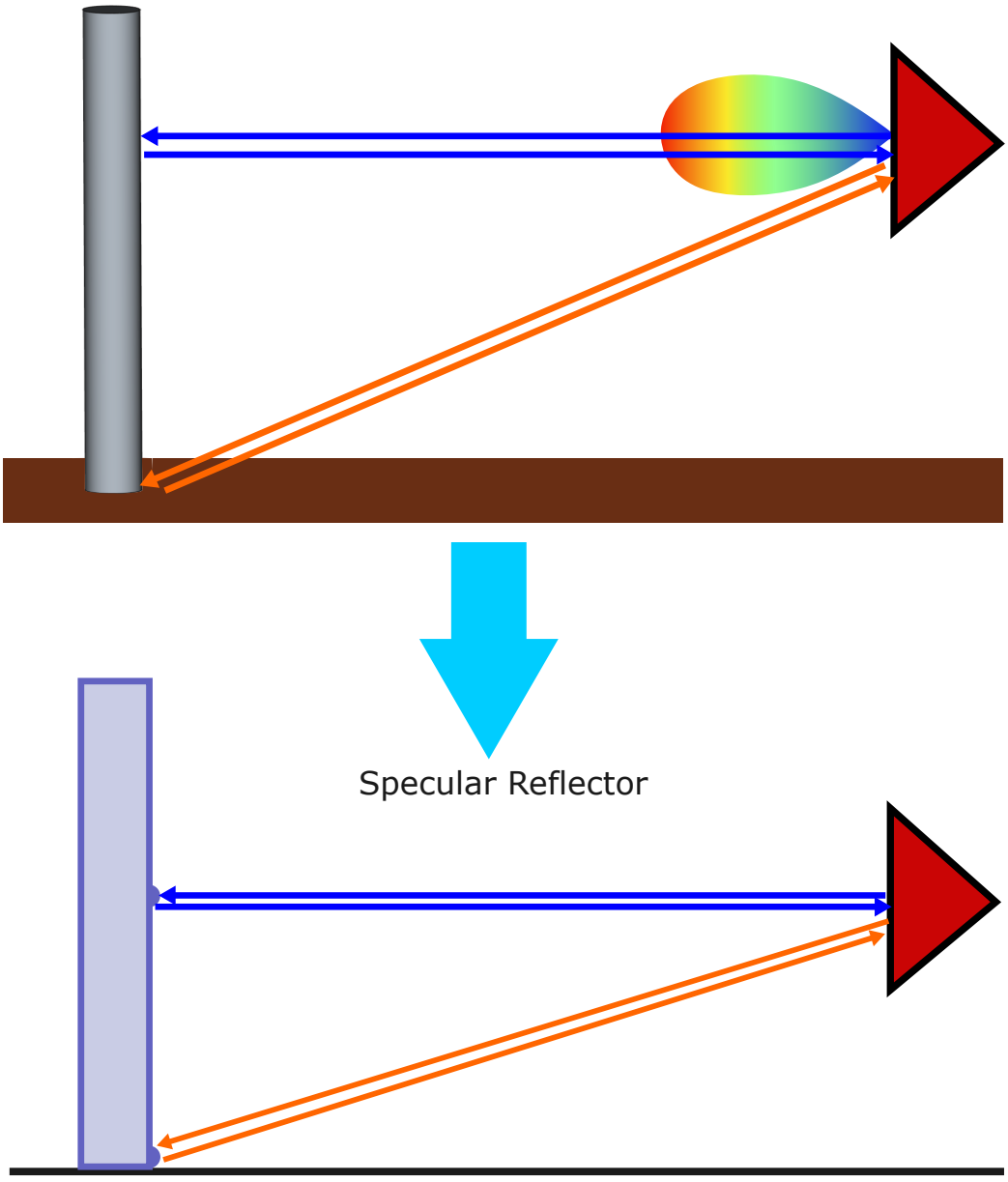

Figure 3.2: Cylinder test case for the simulation tools. On the upper side is the simulation model, and on the lower side is the corresponding theoretical model for Matlab modeling.

2. Modeled as an analytical infinite ground plane of PEC or dielectric, mainly in FEKO with the method large element PO (LEPO)

3. Modeled as a mirror so the object and the antennas are mirrored with respect to the virtual ground plane as seen in Fig. 3.3. To validate it, the results between the mirrored version and the analytical ground in FEKO are compared as seen in Fig. 3.4, where both lines match very well. Thus, this method is validated.

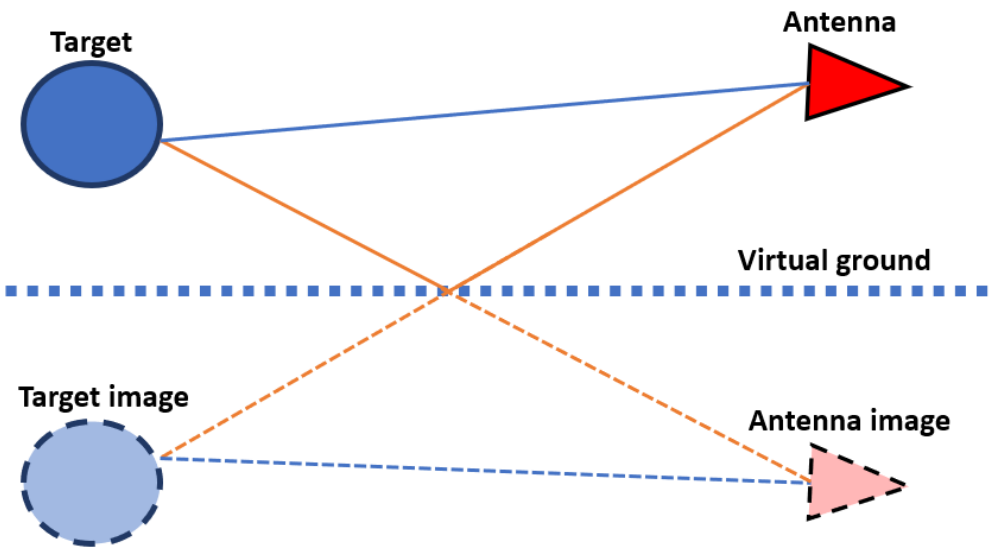

Figure 3.3: Mirroring of the antenna and the target to model the ground reflections by a virtual ground.

3.1.3 Mathematical Model in Matlab

To compare with the results of the tested software, a mathematical model in Matlab is created. The propagation model of the electric field is [21, p. 55]

$$\vec{E}(r) = \vec{E}_0 \frac{e^{-jkr}}{r}, \tag{3.1}$$

where $\vec{E}^0$ is the initial electric field emitted by the transmitting antenna, k is the wave number $k = 2\pi/\lambda$, and r is the distance traveled by the electric wave. Due to ground reflection, there are two ways for the wave to travel between the antenna and the target: one directly and the other indirectly by reflecting off the ground,

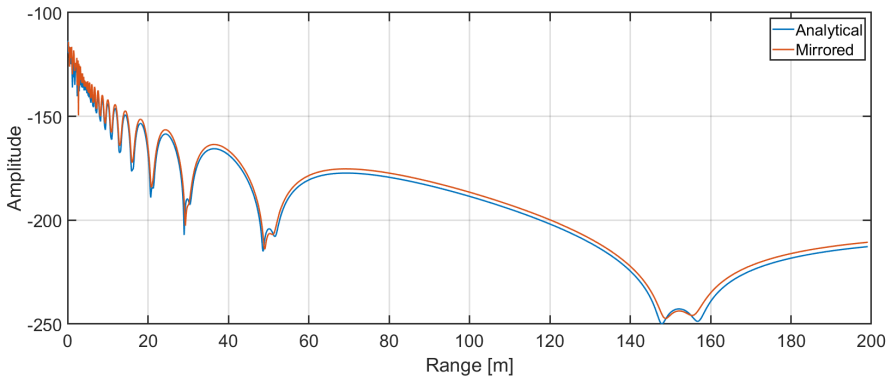

Figure 3.4: Comparison between the two methods of modeling the ground; Analytical layer vs mirroring in FEKO.

as shown in Fig. 3.5. Therefore, there are four paths for the wave to travel from the antenna to the target and back: direct-direct, direct-indirect, indirect-direct, and indirect-indirect. The electric wave travels to the target, reflects off of it, and

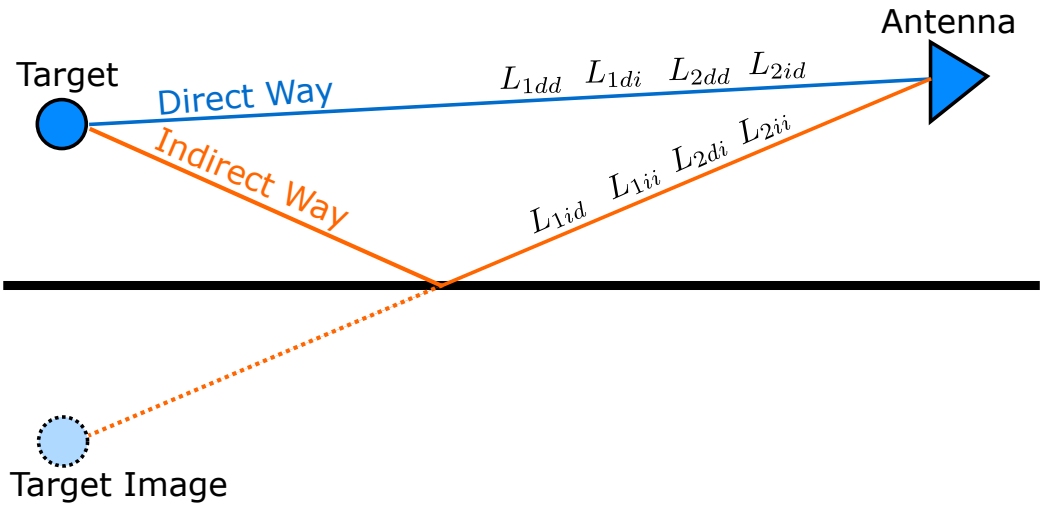

Figure 3.5: Direct and indirect ways for the electric wave to travel from the antenna to the target. The target appears as an image mirrored with respect to the ground.

then travels back to the antenna through either of the two mentioned ways. The proportion of the E field returning is relative to the radar cross section (RCS) of the target. The total E field is the sum of the four paths:

$$\vec{E}_{Rx\_total} = \vec{E}_{Rx\_dd} + \vec{E}_{Rx\_di} + \vec{E}_{Rx\_id} + \vec{E}_{Rx\_ii}, \tag{3.2}$$

where dd refers to direct-direct, di to direct-indirect, id to indirect-direct, and ii to indirect-indirect. To find each component, first, the incident electric field at the target is found as follows [22]

$$\vec{E}_{inc} = \vec{E}^0_{Tx}\frac{e^{-jkL_{1p}}}{L_{1p}} \cdot 1\,\mathrm{m}, \tag{3.3}$$

where E^0_{Tx} is the electric field at $1\,\mathrm{m}$, L_{1p} is the forward path length, and p is one of (dd, di, id, ii). Now, to estimate the scattered E field, it is assumed that the target reflected the incident E field, multiplied by a constant C_T according to its RCS, as follows:

$$\vec{E}_{Rx\_p} = \vec{E}_{inc}C_T\frac{e^{-jkL_{2p}}}{L_{2p}}, \tag{3.4}$$

$$= \vec{E}^0_{Tx}\frac{e^{-jkL_{1p}}}{L_{1p}}C_T\frac{e^{-jkL_{2p}}}{L_{2p}} \cdot 1\,\mathrm{m}, \tag{3.5}$$

$$= \frac{C_T\vec{E}^0_{Tx}}{L_{1p}L_{2p}}e^{-jk(L_{1p}+L_{2p})} \cdot 1\,\mathrm{m}, \tag{3.6}$$

where L_{2p} is the backward path length. Now, it is multiplied by a constant to account for the ground reflection coefficient for the indirect paths:

$$\vec{E}_p = \frac{\Gamma_p C_T\vec{E}_0(1\,\mathrm{m})}{L_{1p}L_{2p}}e^{-jk(L_{1p}+L_{2p})}, \tag{3.7}$$

where Γ_p is the reflection coefficient of the ground for the indirect way and 1 for the direct way, L_{1p} is the length of the forward way, L_{2p} is the length of the return way, and C_T is a constant accounting for the RCS of the target. To find it, the equation for the RCS is used [3, p. 584]:

$$RCS = \lim_{r\to\infty} 4\pi r^2\frac{|\vec{E}_{sc}|^2}{|\vec{E}_{inc}|^2}, \tag{3.8}$$

where $\vec{E}_{sc}$ is the scattered electric field and $\vec{E}_{inc}$ is the incident electric field. Since it is in the near field, the limit is not taken, and the equation is reordered to get:

$$|\vec{E}_{sc}| = \sqrt{\frac{RCS}{4\pi}}\frac{|\vec{E}_{inc}|}{r}, \tag{3.9}$$

and by comparing it with (3.4) it is deduced that

$$C_T = \sqrt{\frac{RCS}{4\pi}}. \tag{3.10}$$

3.1.3.1 Reflection Coefficients -Fresnel Equations

In order to model the ground as a dielectric layer, the reflection coefficient of the ground with respect to the incidence angle is calculated as done in section 2.4.

3.1.3.2 Comparison between the Mathematical Model in Matlab and the Simulation in FEKO and HFSS

To validate the method, the results of the mathematical model are compared with those of the simulation using FEKO. The simulation case in FEKO is a metallic sphere of radius $0.05\,\mathrm{m}$ at a height of $0.3\,\mathrm{m}$. The simulation is carried out with a varying range from 1 to $200\,\mathrm{m}$. Four cases are simulated: One using perpendicular polarization over a road of PEC and one over a road of Asphalt material. The other is using parallel polarization for both cases. The mathematical model is a one-point scattering center at the same height and range. The results of the mathematical model are shifted to align with FEKO because there is a constant shift between both results. Fig.3.6 shows the comparison of the two cases with PEC ground, and fig.3.7 shows the comparison of the cases with Asphalt ground.

It is seen that there is a good match between the results of FEKO and the mathematical model. Another comparison is performed between the mathematical model and the simulation in HFSS for a sphere with a radius of $0.3\,\mathrm{m}$ at a height of $0.4\,\mathrm{m}$. The results are shown in Fig.3.8, which shows a very good match between the results in terms of RCS.

3.1.4 Comparison between the Results of the Various Tools for the Sphere Case

In this section, the comparison between the results of the tested tools and the mathematical model for the sphere over ground case is shown. The ground here is modeled as a perfect electric conductor (PEC). The results are shifted to align vertically because there is a constant shift between them. It is seen in Fig. 3.9 that there is a good match between the tools until a range of $100\,\mathrm{m}$, where the result of HFSS diverges, especially for the sphere over the ground case (where the ground is actually modeled for the simulation). The results from FEKO, Wavefarer, and the mathematical model have a good match along the entire tested range (1-$200\,\mathrm{m}$).

3.1.5 Comparison between the Results of the Various Tools for the Cylinder Case

In this section, the comparison between the results of the tested tools and the mathematical model for the metallic cylinder over ground case is shown. The

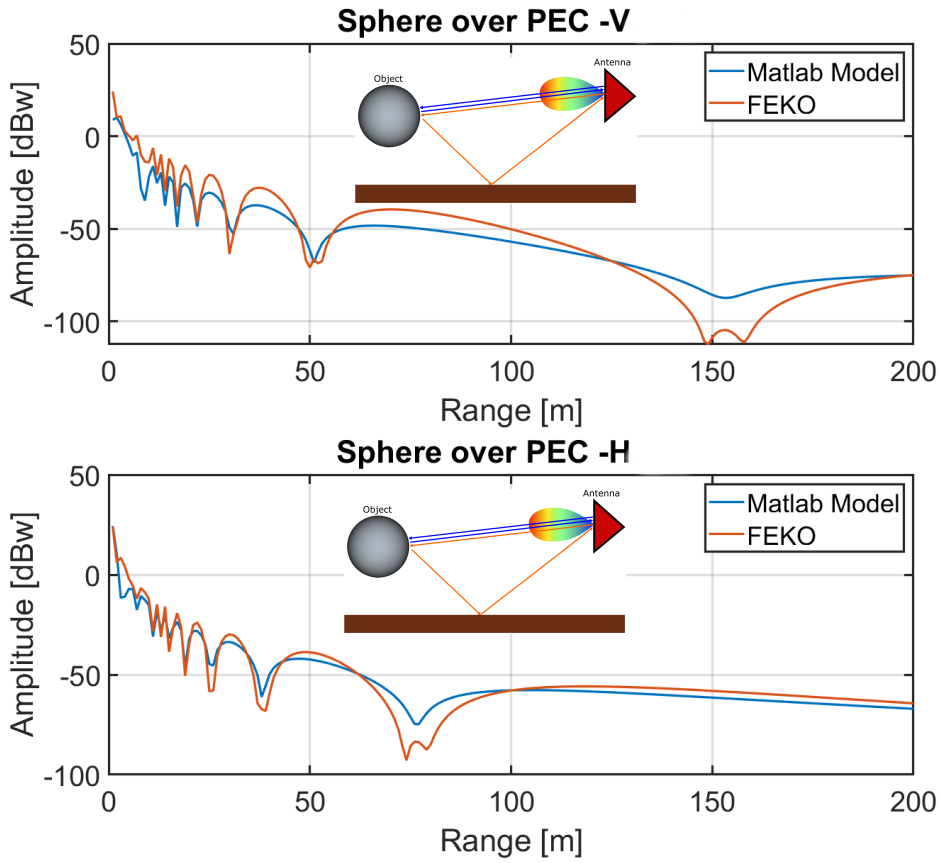

Figure 3.6: Comparison of the four cases between the mathematical model and the simulation in FEKO.

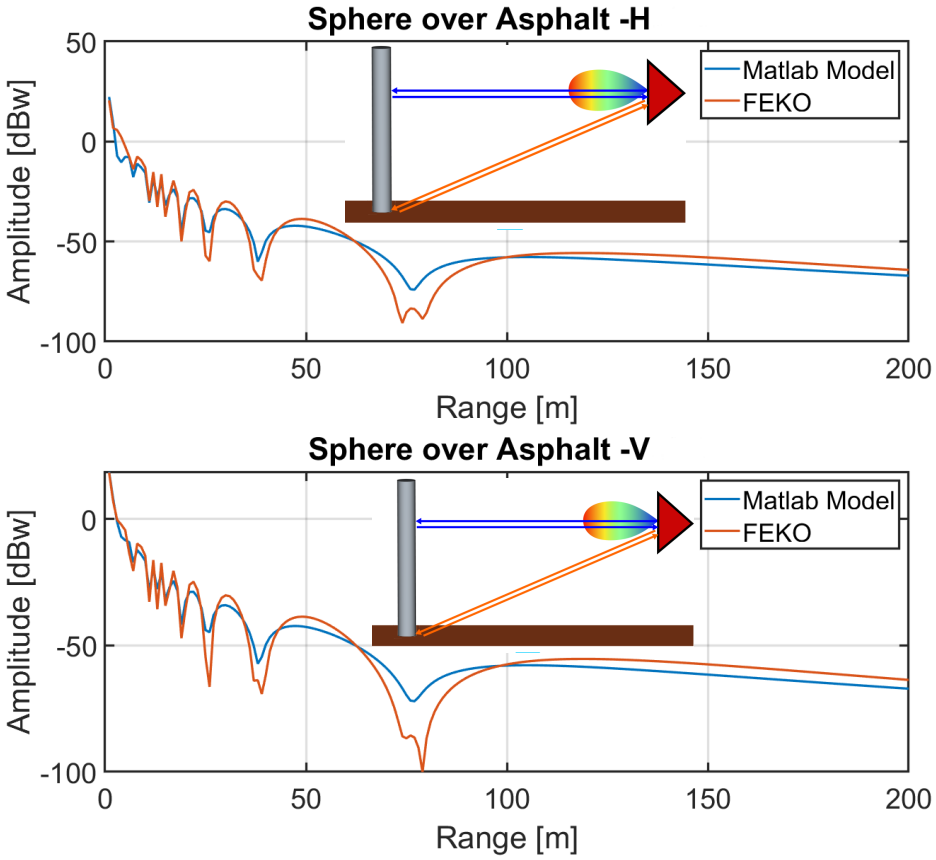

Figure 3.7: Comparison of the four cases between the mathematical model and the simulation in FEKO.

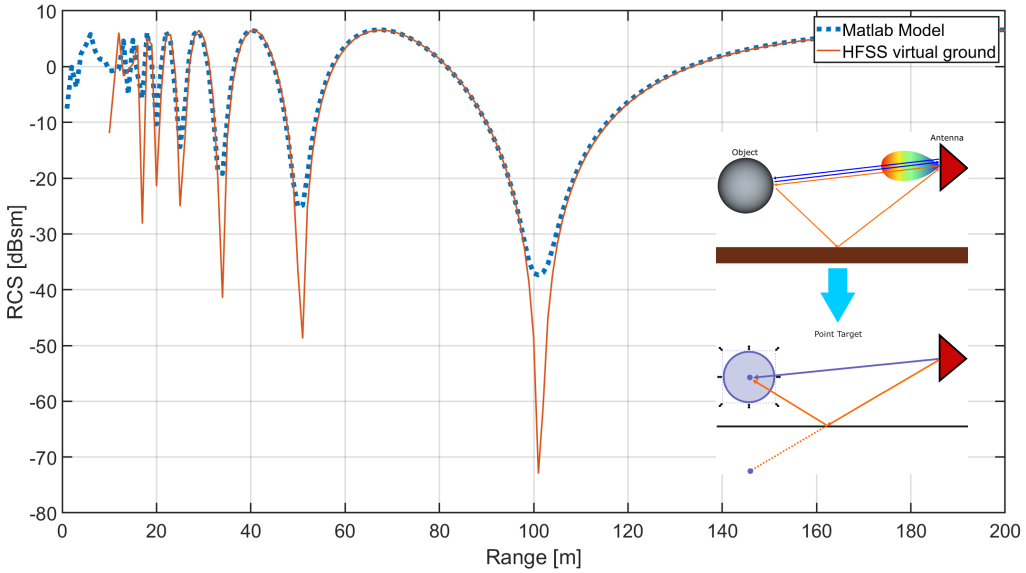

Figure 3.8: Comparison between the mathematical model and the simulation in HFSS for a sphere.

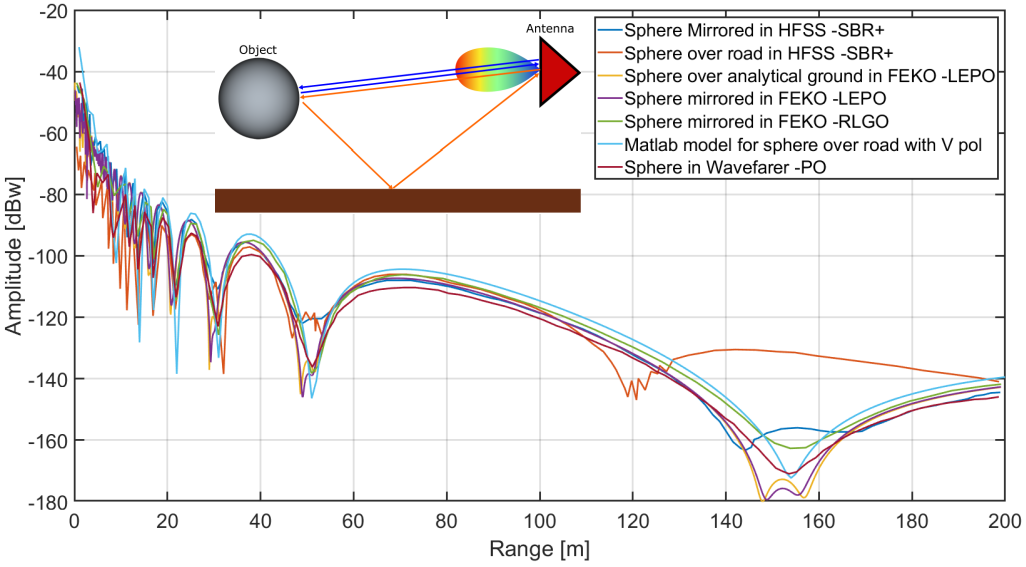

Figure 3.9: Comparison between the tested tools with the mathematical model for the sphere case.

ground here is also modeled as (PEC). The results are also shifted vertically to better align since there is a constant shift between them in the amplitude. The comparison is seen in Fig. 3.10. A good correspondence between the tests is seen

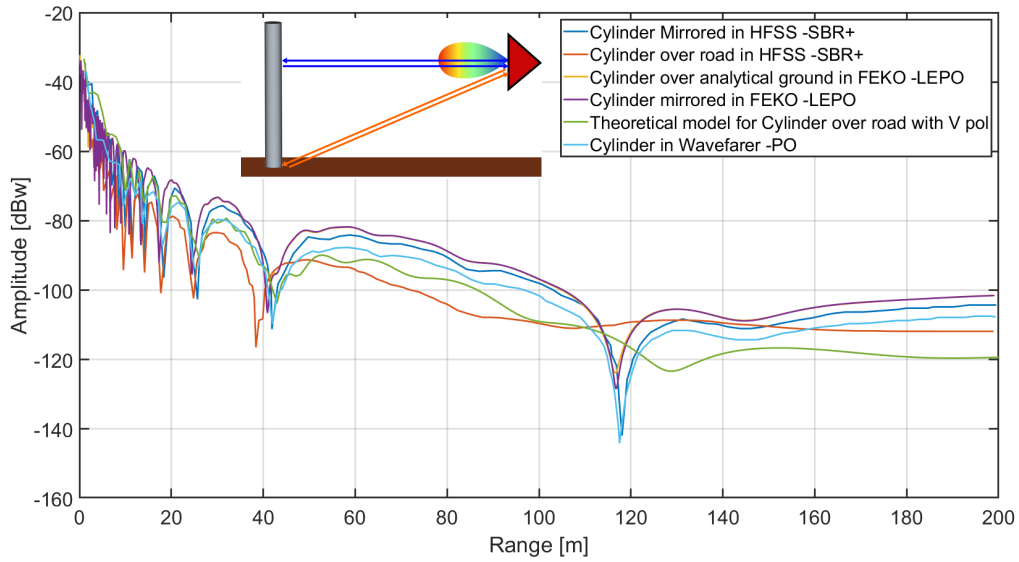

Figure 3.10: Comparison between the tested tools with the theoretical model for the cylinder case.

except for the cylinder over ground case in HFSS, which deviates after a range of $30\,\mathrm{m}$. The reason is expected to be that at far range, the simulation needs much finer angular resolution to capture the reflection of the comparatively small object (the cylinder compared to the ground), but to do that, it will take a prohibitively long time (many days) to simulate. In comparison with the mathematical model, a good match is seen up to a range of $100\,\mathrm{m}$, and then there is a deviation in the location of the next valley at around $130\,\mathrm{m}$. The reason is that the cylinder is a more complicated object with a discontinuity at the top, adding to the response. To validate the idea, a simulation of a much taller cylinder ($10\,\mathrm{m}$) is performed to reduce the effect of the top. The result is shown in Fig. 3.11 together with the mathematical model. In this case, much better correspondence is seen, proving our reasoning. However, it was not possible to model the reflection from the top with a simple scattering center, which indicates that the cylinder is a more complicated object and cannot be simply modeled as scattering centers but rather needs a simulation of the full surface to match well.

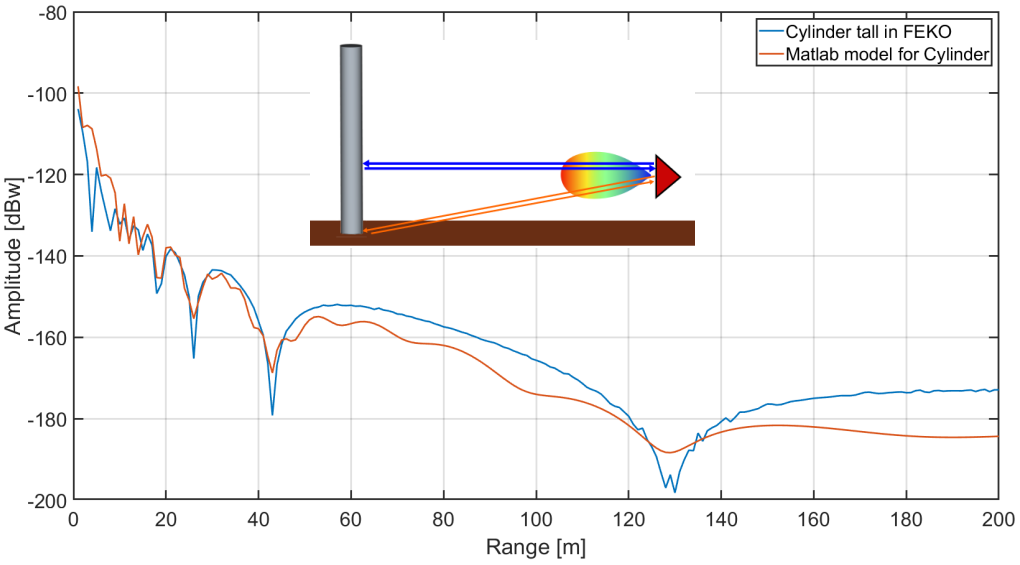

Figure 3.11: Comparison between the simulation of the tall cylinder and the mathematical model.

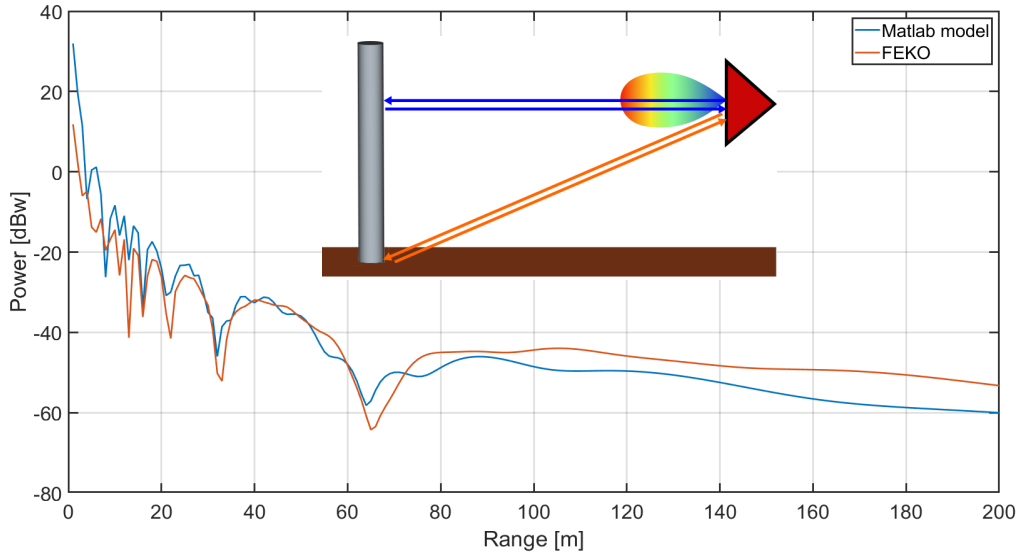

Figure 3.12: Comparison between the simulation of the cylinder over asphalt with the mathematical model.

3.1.6 Simulation Times

In this section, the simulation time for the various tools and methods is presented in the table 3.1. Two machines are used, one with an Intel Xeon processor with 28 cores and 512 GB of RAM, and the other with an Intel Xeon processor with 56 cores and 1500 GB of RAM, both with Windows 10.

Table 3.1: Simulation time for the various tools/methods.

Simulated Case	Method	Cores	Time
Mirrored Object(Cylinder, Sphere)	FEKO/LE-PO	28	42-72 sec
Mirrored Sphere	FEKO/RL-GO	28	10 h
Mirrored Plate	FEKO/PO	28	41 min
Sphere over Road	HFSS/SBR+	28	48 min
Sphere Mirrored	HFSS/SBR+	28	9 min
Sphere/Cylinder Mirrored	Wavefarer/PO	56	$\sim$30 min
Sphere/Cylinder over road	Wavefarer/PO	56	$\sim$1h:40min

3.1.7 Discussion

Due to the need for a high number of simulation runs to generate the enormous amount of data needed to train machine learning neural networks, the required simulation time is defined to be less than $10\,\mathrm{min}$. From the table 3.1, it is seen that only two cases satisfy this condition: Mirrored Object in FEKO and Mirrored in HFSS. However, with the mirroring method, the multiple reflections between the object and the ground cannot be modeled. This case is mainly met with the reflections from the lower parts of the car. Therefore, this method is dropped as well, despite the fact that it is good for comparison and testing.

3.1.8 Conclusion

The results of the simulations using several tools and methods with two predefined test cases were presented: One is sphere over ground, and the other is cylinder over ground, and the results were compared as well with the developed mathematical model considering the targets as point scattering centers. A table of the simulation times for a selection of the simulated cases was shown. In the end, the results were discussed, and the decision was reached not to use any of the tools for either of two reasons, i.e., long simulation time or low accuracy. In the following section, a ray-tracing tool using the MECA method will be developed.

3.2 Ray-Tracing Tool Using the MECA Method

In this section, the ray-tracing tool using the C++ programming language will be developed and tested, and then the MECA method will be applied to calculate the RCS of several objects. The first step is to load the object into the scene. The file format used here is "stl," which is a mesh composed of flat triangles that represents the object as seen in Fig. 3.13 for two objects: a sphere and a cylinder.

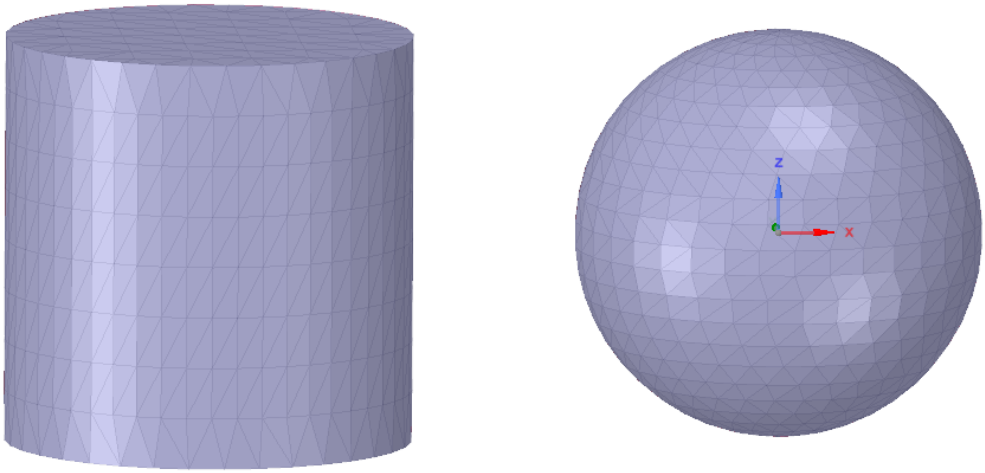

Figure 3.13: Mesh of flat triangles of two objects: a sphere and a cylinder.)

The next step is to send rays toward the object and to find the intersection points between the rays and the surface of the object. At these points, equivalent imaginary electric and magnetic currents are painted according to the previously explained equations and are repeated here for reminding:

$$\begin{aligned}\vec{J}^{MECA} &= \vec{n} \times \vec{H}^{tot}, \\ &= \frac{1}{\eta}\{\vec{E}^{inc}_{TE} \cos\theta^{inc}(1 - R_{TE})\vec{e}_{TE} + \vec{E}^{inc}_{TM}(1 - R_{TM})(\vec{n} \times \vec{e}_{TE})\},\end{aligned} \tag{3.11}$$

$$\begin{aligned}\vec{M}^{MECA} &= -\vec{n} \times \vec{E}^{tot}, \\ &= \{\vec{E}^{inc}_{TE}(1 + R_{TE})(\vec{e}_{TE} \times \vec{n}) + \vec{E}^{inc}_{TM} \cos\theta^{inc}(1 + R_{TM})\vec{e}_{TE}\},\end{aligned} \tag{3.12}$$

then, the scattered E and H fields are calculated using the equations (explained

earlier as well):

$$\vec{E}^s \approx \frac{j}{2\lambda}\frac{\exp(-j\frac{2\pi}{\lambda}r)}{r}\iint_S [\vec{r}\times\vec{M}^{MECA} - (\vec{r}\times\eta\vec{J}^{MECA}\times\vec{r})]\exp(j\frac{2\pi}{\lambda}\vec{r}\cdot\vec{r'})dS, \tag{3.13}$$

$$\vec{H}^s \approx \frac{j}{2\lambda}\frac{\exp(-j\frac{2\pi}{\lambda}r)}{r}\iint_S [\vec{r}\times\vec{J}^{MECA} - (\vec{r}\times\vec{r}\times\frac{1}{\eta}\vec{M}^{MECA})]\exp(j\frac{2\pi}{\lambda}\vec{r}\cdot\vec{r'})dS. \tag{3.14}$$

After that, the RCS is calculated using the equation [23]

$$\text{RCS} = 4\pi\lim_{r\to\infty} r^2\frac{|\vec{E}_s|^2}{|\vec{E}_i|^2}. \tag{3.15}$$

It is chosen to calculate the RCS of a sphere and a cylinder because there are equations to calculate their theoretical value for comparison with the simulation and to estimate the errors incurred by the methods used. The equation for calculating the theoretical RCS of a sphere with a radius r is [24]

$$RCS_{sph} = 4\pi r^2, \tag{3.16}$$

and for a cylinder with a radius r and a height L, and using an electromagnetic wave with wavelength λ, the RCS is [24]

$$RCS_{cyl} = \frac{2\pi L^2 r}{\lambda}. \tag{3.17}$$

The mentioned method is applied on a sphere with a radius r = $0.3\,\mathrm{m}$, and a cylinder with a radius r = $0.3\,\mathrm{m}$ and a height of L = $0.5\,\mathrm{m}$ at a frequency of $76\,\mathrm{GHz}$, and the theoretical RCS of both of them is calculated, which allows us to calculate the error using the equation

$$Error = \frac{|RCS_{sim} - RCS_{th}|}{RCS_{th}} * 100. \tag{3.18}$$

The results are listed in Table 3.2. As can be seen, the error is large. This is because the sphere and the cylinder are curved objects, which here are represented by flat triangular facets that deviate from the actual surface depending on how large these facets are. The error depends on the mesh size, which will be studied in the next section. Fig. 3.14 illustrates the deviation between a mesh composed of flat triangles from the actual curved surface and the effect on the hit-points between the rays and the surface.

The following section will study this phenomenon quantitatively. This work is reprinted, with permission, from [25],

Table 3.2: The simulated and theoretical RCS of a sphere and a cylinder and the corresponding errors

Object	RCS_{sim}	RCS_{th}	Error %
sphere	0.0807	0.2827	71%
cylinder	432.69	119.38	262%

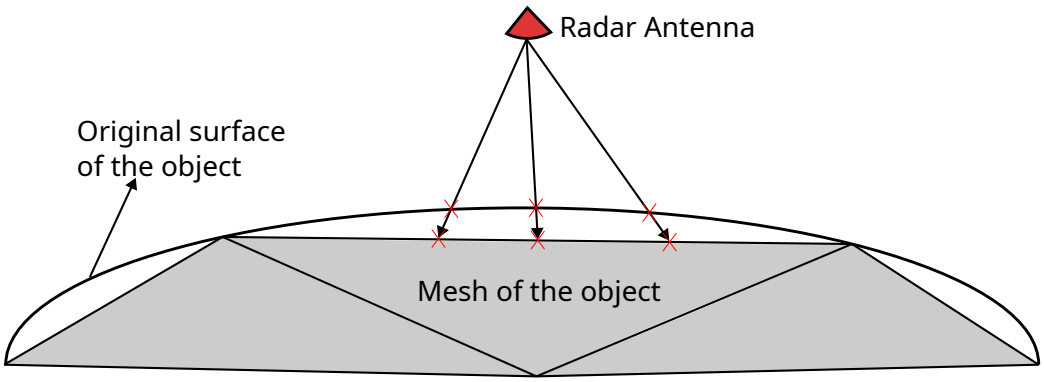

Figure 3.14: The deviation of the flat triangles from the curved surface.

3.2.1 The Effect of Facet Size on the RCS Simulation when Considering Curved Objects

When performing electromagnetic ray-tracing simulation with asymptotic methods like geometric optics (GO) and physical optics (PO), usually the first step is to convert the objects into a mesh composed of triangular flat facets. This will result in errors because the flat facets do not exactly represent the curved parts of the object. This error depends on the meshing criteria, like the maximum surface deviation between the curved surface and the flat triangles, the maximum edge length of the triangles, and the maximum angle difference between the normal to the facet and the normal to the curved surface (normal to the tangential plane to the curved surface at each point). This problem is also reported in [26], and one solution to this problem is to interpolate between the triangles to increase the mesh fidelity and reduce the error, as suggested by [27]. Other methods to deal with curved surfaces are to approximate it by triangles with second-order curved surface instead of the flat one [28] [29] [30] and to utilize Splines directly to represent the surface according to the isogeometric analysis (IGA) [31] [32].

In this work, the effect of the meshing criterion ”maximum surface deviation (SD)” on the errors in the RCS will be studied. This criterion is the largest distance between the generated flat triangle and the original curved surface of the object, as is shown in Fig. 3.15

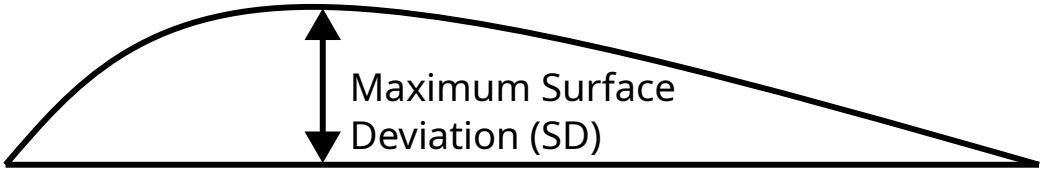

Figure 3.15: The maximum surface deviation (SD), © 2022 IEEE.

This criterion is used because it ensures a good quality mesh with a minimum number of mesh cells due to its technique that produces a higher resolution with a large number of mesh cells at strongly curved sections, where it is needed, and fewer cells at less curved areas. First, to ensure the errors are not due only to the fact that SBR+ is an approximate method but also due to the shape of the faceted sphere, the simulation using both SBR+ and the multi-level fast multi-pole (MLFMM) method is carried out since MLFMM is a full-wave method and more accurate than the asymptotic method SBR+. The simulation is done on a sphere of radius $0.05\,\mathrm{m}$ at $76.5\,\mathrm{GHz}$ while changing the incidence angle in the range $0°$-$10°$. Then the maximum error in mm is taken, and this is repeated for four values of the surface deviation that are (0.01, 0.05, 0.1, 0.5) in mm. The error results are listed in table 3.3

Table 3.3: Relative RCS error from MLFMM and SBR+ methods implemented in ANSYS/HFSS, where the reference is the analytical values, © 2022 IEEE.

SD (mm)	RCS relative error (%)	
	MLFMM	SBR+
0.01	4.8	1.4
0.05	7.4	7.7
0.1	8.5	44
0.5	28.3	52

It is seen that the error increases with decreasing mesh quality in both methods, although the error in the MLFMM case is smaller than expected. The RCS around the faceted sphere fluctuates because if a cross-section of such a sphere is taken, it will be a polygon, not a circle. For this reason, a simulation is performed taking the RCS while changing the angle of incidence around the sphere, and

the resulting graph is shown in Fig. 3.16. The figure confirms our assumption, and as can be seen, the simulated RCS fluctuates in a repeated pattern around the sphere.

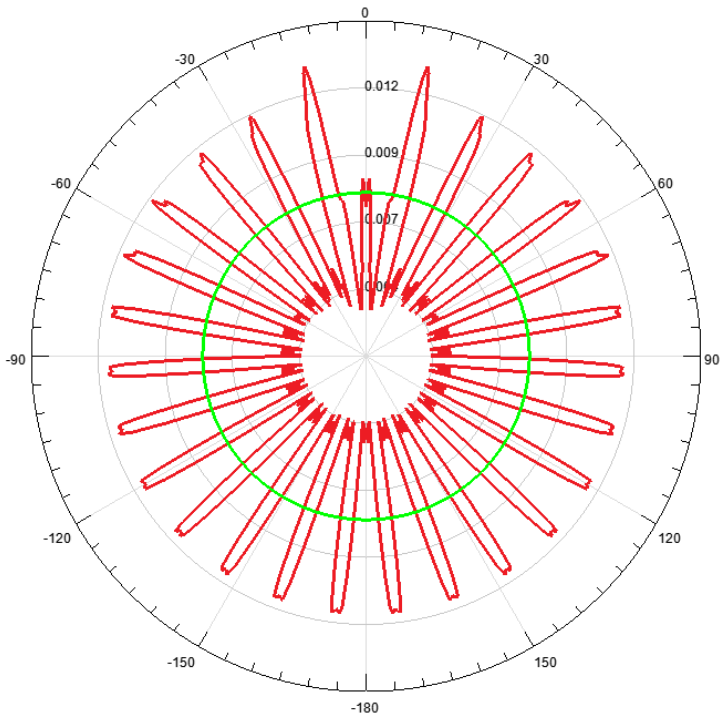

Figure 3.16: RCS of low fidelity sphere with rotating incidence angle (red curve). The green line is the RCS of a smooth sphere, © 2022 IEEE.

3.2.1.1 RCS Error with Surface Deviation

A quantitative study on the effect of meshing on the RCS is carried out in this section. The mesh is generated inside the simulation tool ANSYS HFSS for a sphere with a radius of $0.3\,\mathrm{m}$ and a theoretical RCS of $0.2827\,\mathrm{m}^2 = -5.48\,\mathrm{dBsm}$. The criterion for determining the meshing quality is the maximum surface deviation. To estimate the relative error with each meshing quality, first, a simulation is performed where the observation point is rotated around the sphere. The error is calculated for each angle, and the maximum value is recorded. This is repeated for each surface deviation value over the range [0.0001-2.0000] in mm. The resulting graph is shown in Fig. 3.17. It can be seen that the relative error is heavily fluctuating above the value $0.01\,\mathrm{mm}$, below which the RCS stabilizes close to the theoretical value. Therefore, using this meshing procedure with an SD of below $0.01\,\mathrm{mm}$ is suggested as a good method to approximate the surface

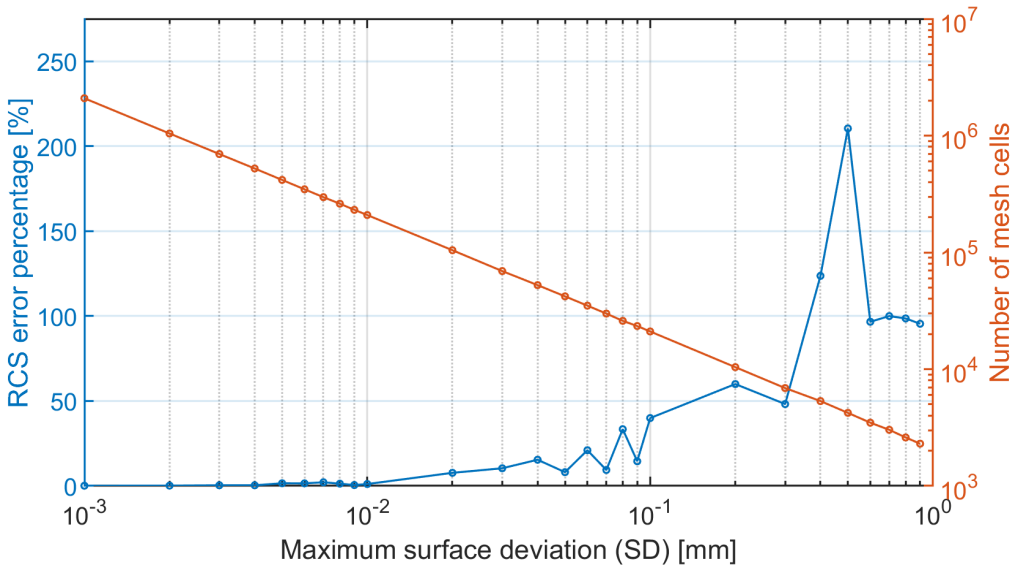

Figure 3.17: RCS error vs surface deviation and number of mesh cells, © 2022 IEEE.

of curved objects. It also shows that the number of mesh cells to achieve this level of accuracy for a sphere is above $200{,}000$, which shows that for targets with curved surfaces, there is a need to further decrease the number of facets.

3.2.1.2 Validation with Cylinder Shape

To validate the meshing parameter found in the previous section, another shape is simulated, which has an analytical formula for RCS and a curved surface, and it is a cylinder with a height of $1\,\mathrm{m}$ and a radius of $0.3\,\mathrm{m}$. The simulation is done using the HFSS/SBR+ method and the meshing criterion "maximum surface deviation (SD)" of $0.01\,\mathrm{mm}$ at $76\,\mathrm{GHz}$. The estimated RCS by the simulation is $482\,\mathrm{m}^2$ ($26.8\,\mathrm{dBsm}$), while the theoretical value is calculated to be $477.5\,\mathrm{m}^2$ ($26.7\,\mathrm{dBsm}$), and the resulting error here is $0.98\,\%$, which is good for most applications, and shows that the presented criterion is suitable. Typical automotive radar targets with a cylindrical profile are, e.g., bridge columns, traffic sign poles, and car entrance barriers, and they are shown in Fig. 3.18.

3.2.1.3 Curvilinear Mesh

One method that can produce an accurate RCS while using a low number of triangles is the use of curvilinear mesh elements. This method is provided by the software tool Altair/FEKO with the ray launching geometric optics (RLGO)

Figure 3.18: Typical automotive radar targets with cylindrical profile. (a) Bridge column, (b) car entrance barriers, and (c) traffic sign pole, © 2022 IEEE.

method. This technique allows the triangular facets to have a curved shape, which better represents the original surface curvature. As a test, a sphere with a radius of $0.3\,\mathrm{m}$ is meshed using this technique with an edge-length of $0.15\,\mathrm{m}$, and is shown in Fig. 3.19 This technique is used to simulate this sphere over several values of edge-length, and the RCS along with the error is shown in Table 3.4 The results

Table 3.4: Simulation using RLGO method in Altair/FEKO and curvilinear triangles, © 2022 IEEE.

Edge Length (m)	Number of Triangles	RCS (m^2)	Error(%)
0.05	1094	0.2897	2.4
0.1	272	0.2714	4.0
0.15	144	0.2719	3.8

show that a reasonable accuracy can be achieved with a much lower number of mesh cells compared with flat triangles (~ 1000 vs $\sim$200,000) for a sphere with a radius of $0.3\,\mathrm{m}$.

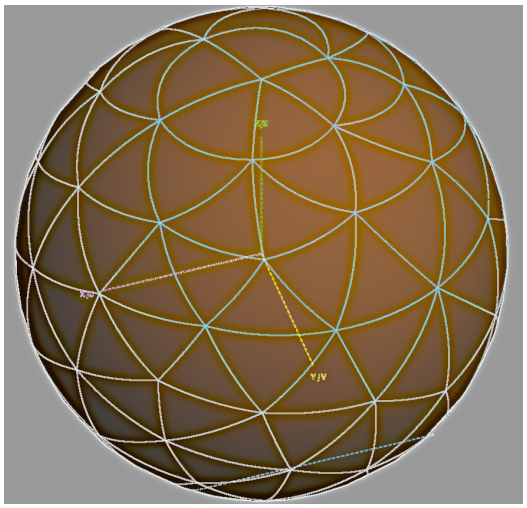

Figure 3.19: Sphere meshed using curvilinear triangles with edge-length of $0.15\,\mathrm{m}$, © 2022 IEEE.

3.2.2 Validation of the Ray-Tracer Tool with Properly Meshed Objects

It has been shown that the large error encountered in testing the ray-tracer tool was due to the coarse meshing of the objects. Now the tool is tested with a sphere and a cylinder meshed using maximum surface deviation (SD) of $0.01\,\mathrm{mm}$ as suggested. The sphere has a radius of $0.3\,\mathrm{m}$, and the cylinder has a radius of $0.3\,\mathrm{m}$ and a height of $0.5\,\mathrm{m}$, where they are simulated at a frequency of $76\,\mathrm{GHz}$. The simulation results, along with the theoretical values and the relative errors, are listed in Table 3.5. As can be seen, the errors now are very small, which validates both the meshing method and the simulation technique.

Table 3.5: The simulated and theoretical RCS of a sphere and a cylinder and the corresponding errors when meshing the objects with SD of 0.01 mm, © 2022 IEEE.

Object	RCS_{sim}	RCS_{theory}	Error (%)
sphere	0.281	0.2827	0.6%
cylinder	118.4	119.38	0.8%

In case the object is available as a mesh only, which means that the original CAD file is not available to perform the previous meshing method to get the

required resolution, the low-fidelity mesh needs to be handled directly. This will be handled in the next section, which is reprinted, with permission, from [33], © 2023 IEEE.

3.2.3 Extracting Curvature Information From Low Fidelity Mesh for Electromagnetic Ray-Tracing Simulations

As discussed, meshing an object with the required high quality, or refining an existing mesh through interpolation, will require a large number of mesh cells/triangles. Therefore, the existing mesh should be dealt with by estimating the curved surface from the available triangles or mesh points. There exists an algorithm to estimate quadratic surface patches like in [34], or to fit B-spline batches to a triangle mesh in [35]. Then, an algorithm is needed to find the intersection points between rays and these surfaces, like in [36] and [37]. In this work, first, the normals at all vertices are found according to [38], then estimating the average curvature tensors as in [39], and finally the intersection point between the ray and the curved surface is found, and the correct normal and reflected ray via our suggested approximate method. Fig. 3.20 illustrates the steps taken.

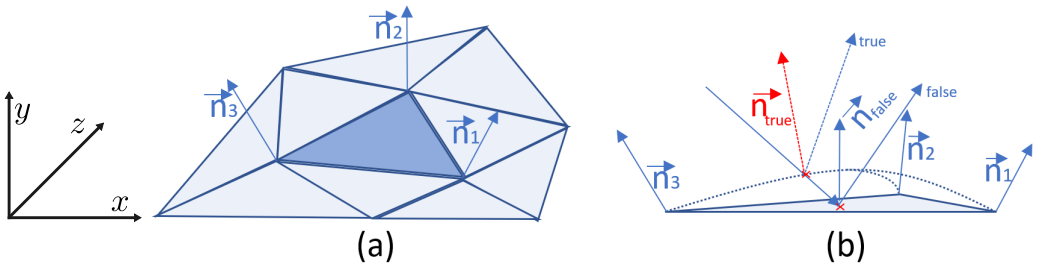

Figure 3.20: Illustration of the method. First in (a), finding the normals to the vertices. Secondly, in (b), estimating the curvature, then finding the intersection point, the correct normal, and the reflected ray, © 2022 IEEE.

3.2.3.1 Finding the Normals at the Mesh Vertices Depending on the Facet Normals

The first step of the modified method is to find the normal vectors at the vertices of the mesh, taking into consideration the neighboring facets to approximate a curved surface. The approach presented in [38] is adopted, which calculates the normal at the vertex by averaging over the normals of the adjacent facets, weighted by the lengths of the edges and the sin function value of the angle between them. Fig. 3.21 shows one vertex Q with three connected triangles (there could be more than

three) and their normals, which are used to approximate the vertex normal N. The

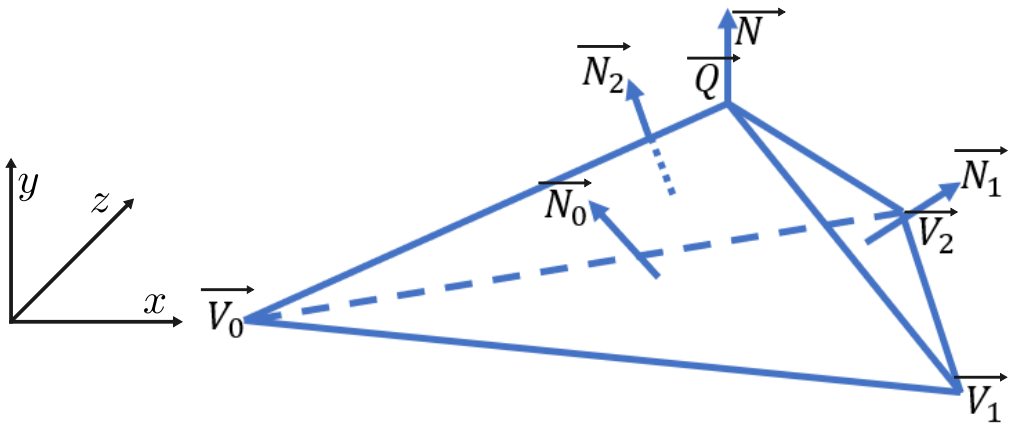

Figure 3.21: A vertex Q and the connected triangles with their normals, © 2022 IEEE.

equation used in the reference paper to find the normal is:

$$c\vec{N} = \sum_{i=0}^{2} \frac{\overrightarrow{QV}_i \times \overrightarrow{QV}_{i+1}}{|\overrightarrow{QV}_i|^2 |\overrightarrow{QV}_{i+1}|^2} = \sum_{i=0}^{2} \frac{\vec{N}_i \sin\alpha_i}{|\overrightarrow{QV}_i||\overrightarrow{QV}_{i+1}|}, \tag{3.19}$$

where V_i is a vertex (node) of the triangles connected to the vertex in question Q, which means that QV_i is the edge vector directed from Q to V_i, α_i is the angle between the edges of the triangle i that are connected to the vertex Q, N_i is the normal to the flat triangle i, and c is a scalar multiplier of the resulting normal N. To simplify calculations, the following formula is used:

$$A_i = \sin\alpha_i |\overrightarrow{QV}_i||\overrightarrow{QV}_{i+1}|/2, \tag{3.20}$$

which is derived as follows, considering Fig. 3.22 and setting Q to be the coordinate origin:

$$A_i = |\overrightarrow{QV}_{i+1}| \frac{|\overrightarrow{V_iD}|}{2} = |\overrightarrow{QV}_{i+1}||\overrightarrow{QV}_i| \frac{\sin\alpha}{2}. \tag{3.21}$$

Substituting (3.21) into (3.19) yields the following equation:

$$c\vec{N} = \sum_{i=0}^{2} \frac{2\vec{N}_i A_i}{|\overrightarrow{QV}_i|^2 |\overrightarrow{QV}_{i+1}|^2}. \tag{3.22}$$

By using this formula, the vertex normals of the mesh are obtained, and Fig. 3.23 shows the result for a sphere

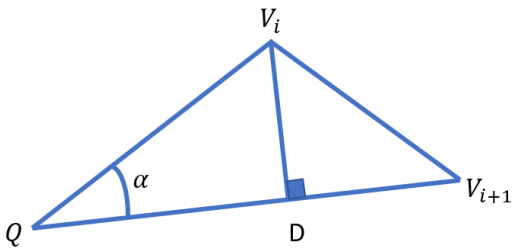

Figure 3.22: Triangle to derive alternative area equation, © 2022 IEEE.

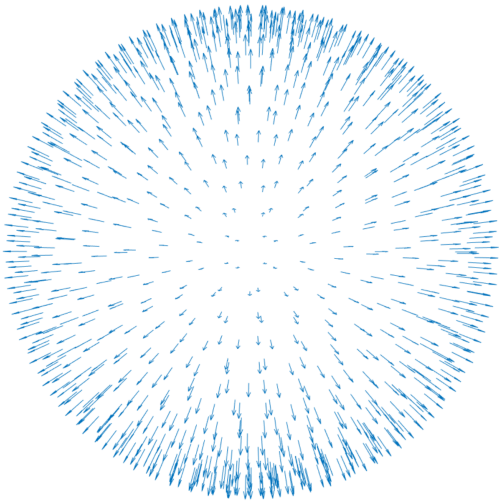

Figure 3.23: The resulting vertex normals of a triangle-based mesh of a sphere, © 2022 IEEE.

3.2.3.2 Estimating the Curvature Tensors from the Triangular Mesh and the Vertex Normals

In this step, the curvature tensors Π_i of the triangular mesh and the vertex normals previously calculated are estimated as done in [39]. The normal curvature k_n of a surface at some point p_i in some direction s is the reciprocal of the radius of the osculating circle touching the surface at that point in that direction, and it satisfies the formula:

$$k_n = \begin{pmatrix} s_u & s_v \end{pmatrix} \begin{pmatrix} \Pi_{11} & \Pi_{12} \\ \Pi_{21} & \Pi_{22} \end{pmatrix} \begin{pmatrix} s_u \\ s_v \end{pmatrix} = \vec{s}^{\,T} \Pi \, \vec{s}, \tag{3.23}$$

where s is a unit-length vector in the tangent plane of the surface with orthonormal coordinates u and v centered at the point. The symmetric matrix Π ($\Pi_{12} = \Pi_{21}$) is known as the Weingarten matrix or the second fundamental tensor. The eigenvalues of this tensor are the principal curvatures of the surface at the point, which are the maximum and minimum normal curvatures in the principal directions, which are the eigenvectors. To estimate the average value of the tensor on the triangle, first, it is written in terms of the directional derivatives of the surface normal as follows:

$$\Pi = (D_u\vec{n} \; D_v\vec{n}) = \begin{pmatrix} \frac{\partial n}{\partial u} \cdot u & \frac{\partial n}{\partial v} \cdot u \\ \frac{\partial n}{\partial u} \cdot v & \frac{\partial n}{\partial v} \cdot v \end{pmatrix}. \tag{3.24}$$

Multiplying this matrix by a direction in the tangent plane results in the derivative of the normal in this direction, as in the equation:

$$\Pi\vec{s} = D_s\vec{n}. \tag{3.25}$$

To solve for the tensor, a finite difference approximation is used along the edges of the triangle. An orthonormal basis is established in the tangent plane with unit vectors $\vec{u}$ and $\vec{v}$ such that $\vec{u}$ is along $\vec{e}_0$ and $\vec{v}$ is along $\vec{u} \times \vec{N}_0$, where $\vec{N}_0$ is the normal of the triangle's surface as illustrated in Fig. 3.24. Discretizing (3.25) along the triangle's edges gives the system of equations on Fig. 3.24.

To solve for Π, the multiplication in the equations is performed, and the resulting formulas are rearranged as follows:

$$\Pi_{11} + \Pi_{12}\frac{\vec{e}_i \cdot \vec{v}}{\vec{e}_i \cdot \vec{u}} = \frac{\Delta\vec{n}_i \cdot \vec{u}}{\vec{e}_i \cdot \vec{u}}, \tag{3.26}$$

$$\Pi_{21} + \Pi_{22}\frac{\vec{e}_i \cdot \vec{v}}{\vec{e}_i \cdot \vec{u}} = \frac{\Delta\vec{n}_i \cdot \vec{v}}{\vec{e}_i \cdot \vec{u}}. \tag{3.27}$$

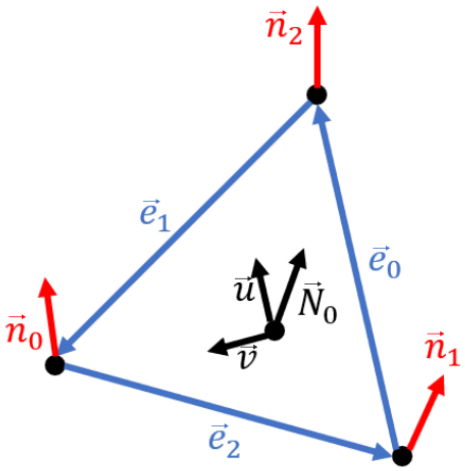

$$\Pi \begin{pmatrix} \vec{e}_0 \cdot \vec{u} \\ \vec{e}_0 \cdot \vec{v} \end{pmatrix} = \begin{pmatrix} (\vec{n}_2 - \vec{n}_1) \cdot \vec{u} \\ (\vec{n}_2 - \vec{n}_1) \cdot \vec{v} \end{pmatrix},$$

$$\Pi \begin{pmatrix} \vec{e}_1 \cdot \vec{u} \\ \vec{e}_1 \cdot \vec{v} \end{pmatrix} = \begin{pmatrix} (\vec{n}_0 - \vec{n}_2) \cdot \vec{u} \\ (\vec{n}_0 - \vec{n}_2) \cdot \vec{v} \end{pmatrix},$$

$$\Pi \begin{pmatrix} \vec{e}_2 \cdot \vec{u} \\ \vec{e}_2 \cdot \vec{v} \end{pmatrix} = \begin{pmatrix} (\vec{n}_1 - \vec{n}_0) \cdot \vec{u} \\ (\vec{n}_1 - \vec{n}_0) \cdot \vec{v} \end{pmatrix}.$$

Figure 3.24: One triangle of the mesh with its coordinate system on the left. And on the right, the resulting system of equations, © 2022 IEEE.

These equations can be written in the form $b + ax_i = y_i$ and solved using linear least squares, which yields the matrix equation

$$\begin{pmatrix} \Sigma x_i^2 & \Sigma x_i \\ \Sigma x_i & n \end{pmatrix} \begin{pmatrix} a \\ b \end{pmatrix} = \begin{pmatrix} \Sigma x_i y_i \\ \Sigma y_i \end{pmatrix}. \tag{3.28}$$

The solution can be found using the equations

$$a = \frac{n\Sigma x_i y_i - \Sigma x_i \Sigma y_i}{n\Sigma x_i^2 - (\Sigma x_i)^2}, \tag{3.29}$$

$$b = \frac{\Sigma y_i \Sigma x_i^2 - \Sigma x_i \Sigma x_i y_i}{n\Sigma x_i^2 - (\Sigma x_i)^2}. \tag{3.30}$$

After applying this method, for example, to a sphere with radius of $0.3\,\mathrm{m}$, and extracting the eigenvalues of the tensors, the same values $k_1 = k_2 = 3.333$ for all tensors are found, which is corresponding to the theory that states that the normal curvature for a sphere is the same everywhere and it equals the reciprocal of the radius of the sphere $1/r$ [13]. In this case, the radius is $r = 0.3\,\mathrm{m}$, so the curvature is $1/0.3 = 3.333$.

3.2.3.3 Finding the Corrected Intersection between the Ray and the Curved Surface

In this section, the previously calculated curvature tensors and vertex normals will be used to find the correct intersection point between the ray and the curved surface. The ray is defined by an origin and direction. It can be seen as a virtual line that passes through the origin and is directed along the direction, which represents the line along which the EM waves propagate, starting at the origin, which is usually the radar's transmitter. The method is outlined as follows using Fig. 3.25 as an illustration:

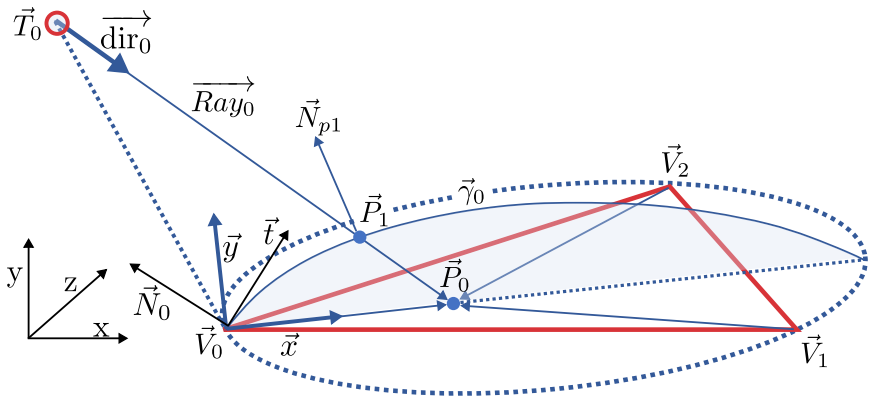

Figure 3.25: A ray hitting the triangle at $\vec{P}_0$ and the coordinate system to find the intersection point with the curve at $\vec{P}_1$, © 2022 IEEE.

- Use the usual method to find the intersection point $\vec{P}_0$ between the flat triangle and the ray $\overrightarrow{\text{Ray}_0}$ with an origin at $\vec{T}_0$ and a direction along $\overrightarrow{T_0P_0}$ or the unit vector $\overrightarrow{\text{dir}_0}$.
- A new coordinate system xyz is constructed in the plane that contains the points $(\vec{V}_0, \vec{P}_0, \vec{T}_0)$.
- The unit vector $\vec{x}$ is constructed along $\overrightarrow{V_0P_0}$ using the equation:

$$\vec{x} = \frac{\overrightarrow{V_0P_0}}{|\overrightarrow{V_0P_0}|}. \tag{3.31}$$

- The unit vector $\vec{y}$ is created on the plane containing $(\vec{V}_0, \vec{T}_0, \vec{P}_0)$ and perpendicular to $\vec{x}$. This is done by subtracting the component of $\overrightarrow{V_0T_0}$ along $\vec{x}$ from itself to get only the component perpendicular to $\vec{x}$, which is

along $\vec{y}$. Therefore, we normalize this vector to get $\vec{y}$, which is done using the equation:

$$\vec{y} = \frac{\overrightarrow{V_0T_0} - \overrightarrow{V_0T_0} \cdot \vec{x}\,\vec{x}}{|\overrightarrow{V_0T_0} - \overrightarrow{V_0T_0} \cdot \vec{x}\,\vec{x}|}. \tag{3.32}$$

- The intersection between the plane containing the points ($\vec{V_i}, \vec{T_0}, \vec{P_0}$) and the curved surface is assumed to be γ_0

- The y value of the curve γ_0 in this coordinate system can be expressed using Taylor expansion as:

$$\begin{aligned} y_c(x) &\approx y_c(0) + y_c'(0)x + \frac{1}{2}y_c''(0)x^2, \\ y_c(0) &= 0 \text{ since the origin is at } V_0. \end{aligned} \tag{3.33}$$

- The unit vector $\vec{t}$ is the tangent to the curved surface at V_0 in the plane spanned by the unit vectors ($\vec{x}$, $\vec{y}$), and since $\vec{N_0}$ is the normal to the surface at V_0, then it is perpendicular to $\vec{t}$ as well. Therefore, $\vec{t}$ is calculated using the equation:

$$\vec{t} = \frac{\vec{N_0} \times (\vec{x} \times \vec{y})}{|\vec{N_0} \times (\vec{x} \times \vec{y})|}, \tag{3.34}$$

  where $\vec{N_0}$ is the normal to the surface at the point V_0.

- $y_c'(0)$ is the the slope of the tangent vector $\vec{t_i}$ of the curve γ_i at V_0, and in the $\vec{x}\vec{y}$ coordinates, it is:

$$y_c'(0) = \frac{\vec{t} \cdot \vec{y}}{\vec{t} \cdot \vec{x}}. \tag{3.35}$$

- κ is the curvature of the surface along γ_0, which is calculated using:

$$\kappa = \Pi\vec{x}_{uv} \cdot \vec{x}_{uv}, \tag{3.36}$$

  where $\vec{x}_{uv}$ is $\vec{x}$ projected on the uv-coordinates.

- Considering the parametric curve equation $\gamma(x) = (x, y(x))$, the equation for the curvature κ is [13]

$$\kappa = \frac{||\vec{\gamma}'' \times \vec{\gamma}'||}{||\vec{\gamma}'||^3} \tag{3.37}$$

- The equations for the derivatives are:

$$\vec{\gamma}' = (1, y_c'(0) + y_c''(0)x), \tag{3.38}$$
$$\vec{\gamma}'' = (0, y_c''(0)). \tag{3.39}$$

Then, by using the curvature equation, the following equation results:

$$y_c'' = \mp\kappa(1 + y_c'^2(0))^{3/2} \tag{3.40}$$

The sign is positive for a concave surface, and negative for a convex surface, as shown in fig.3.26.

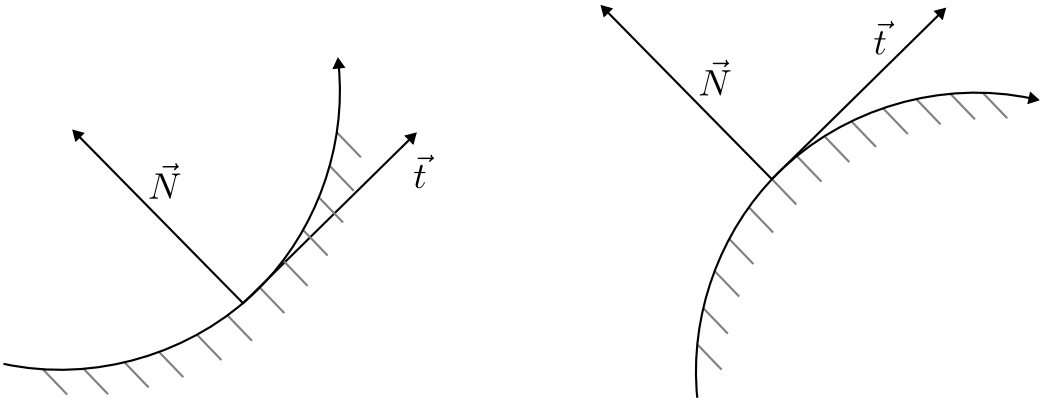

Figure 3.26: The sign of the curvature for the two cases: convex and concave surfaces, © 2022 IEEE.

- The function of the ray in terms of x and y is:

$$y(x) = y_{t0} + \frac{dy}{dx}(x - x_{t0}), \tag{3.41}$$

where x_{t0} and y_{t0} are the x and y coordinates of the ray origin, respectively, and dy/dx is the slope of the ray in the xy coordinates, and they are given by the equations:

$$y_{t0} = \overrightarrow{V_i T_0} \cdot \vec{y},$$
$$x_{t0} = \overrightarrow{V_i T_0} \cdot \vec{x},$$
$$\frac{dy}{dx} = \frac{\overrightarrow{T_0 P_0} \cdot \vec{y}}{\overrightarrow{T_0 P_0} \cdot \vec{x}}.$$

- Solving the equations (3.33) and (3.41) for equality gives:

$$\begin{aligned} & y_{t0} + \frac{dy}{dx}(x - x_{t0}) = y_c'(0)x + \frac{1}{2}y_c''(x)x^2, \\ & \Rightarrow \frac{1}{2}y_c''(x)x^2 + (y_c'(0) - \frac{dy}{dx})x + x_{t0}\frac{dy}{dx} - y_{t0} = 0, \\ & x = \frac{\frac{dy}{dx} - y_c'(0) \pm \sqrt{(\frac{dy}{dx} - y_c'(0))^2 - 2y_c''(\frac{dy}{dx}x_{t0} - y_{t0})}}{y_c''}. \end{aligned} \tag{3.42}$$

- x is chosen with the minimum absolute value and y is calculated using (3.33) or (3.41).

- The intersection point P_1 is found using

$$P_1 = x \cdot \vec{x} + y \cdot \vec{y}. \tag{3.43}$$

- Calculating the normal vector at P_1. From (3.25), it is found that the difference in the normal in the uv coordinates is:

$$\Delta\vec{N} = xD_s\vec{N} = x\Pi\vec{x}_{uv}. \tag{3.44}$$

  This difference is in the uv coordinates. Therefore, it is multiplied by the unit vectors $\vec{u}$ and $\vec{v}$ to find the difference in the global coordinates, which leads to the following equation:

$$\vec{N}_{p1} = \vec{N}_{v0} + x\left[(\Pi_{00}x_{uv0} + \Pi_{01}x_{uv1})\vec{u} + (\Pi_{10}x_{uv0} + \Pi_{11}x_{uv1})\vec{v}\right]. \tag{3.45}$$

- Repeat the process for the three vertices and calculate the average of them to be the new hitting point and normal.

3.2.3.4 Test Results

For testing the method, two objects are chosen, which are a sphere and a cylinder, as usual, because there are theoretical values for their RCS to compare our results with. The sphere is with a radius of $0.3\,\mathrm{m}$, and the cylinder is with a radius of $0.3\,\mathrm{m}$ and a height of $0.5\,\mathrm{m}$ at a frequency of $76\,\mathrm{GHz}$. First, for visual inspection, the intersections between the rays and the original faceted shape of both the sphere and the cylinder are plotted, where the color is proportional to the cosine of the angle between the ray and the normal at the hitting point. Fig. 3.27 and Fig. 3.28 show the resulting pictures for the faceted case, where the curvature is not

considered, for both shapes in (a), and when the curvature is considered in (b) according to the curvature reconstruction algorithm in (3.2.3.3). By comparison, a clear difference between the two cases is visible (the flat facets are seen in the first case, while in the second case, a smooth surface is seen), which indicates that the curvature in both cases is recovered in (b).

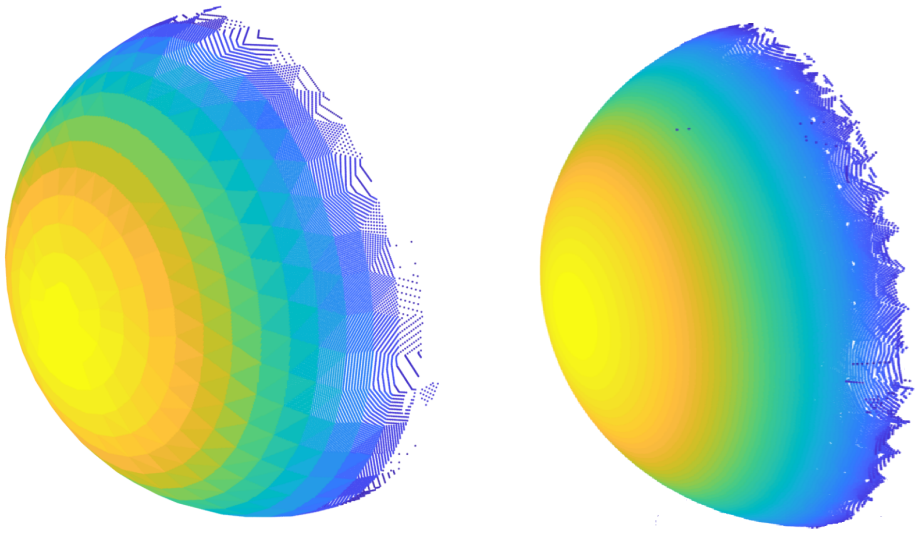

Figure 3.27: The hitting points between the rays and the original flat facets of a sphere in (a) and with curved surface reconstructed from the triangular mesh in (b). The color is proportional to the cosine of the angle between the ray and the surface, © 2022 IEEE.

The results of the RCS simulation in both cases are listed in Table 3.6

The results show clearly that the RCS values calculated without considering the curvature are completely wrong, while the usage of the estimated curved surface results in simulated values that match the theoretical ones with practically acceptable errors below $5\,\%$.

3.2.3.5 Convergence Analysis

To find for which values of the surface deviation (SD), the resulting RCS is close to the theoretical value, a convergence analysis is performed, where the simulation is done for a range of SD values, and the results are listed in Table **??**

As can be seen from the table, the simulated RCS value converges to the theoretical one, with a minimum error of $0.3\,\%$. The suitable SD value can be chosen according to the desired trade-off between the accuracy and the number of facets, depending on the application.

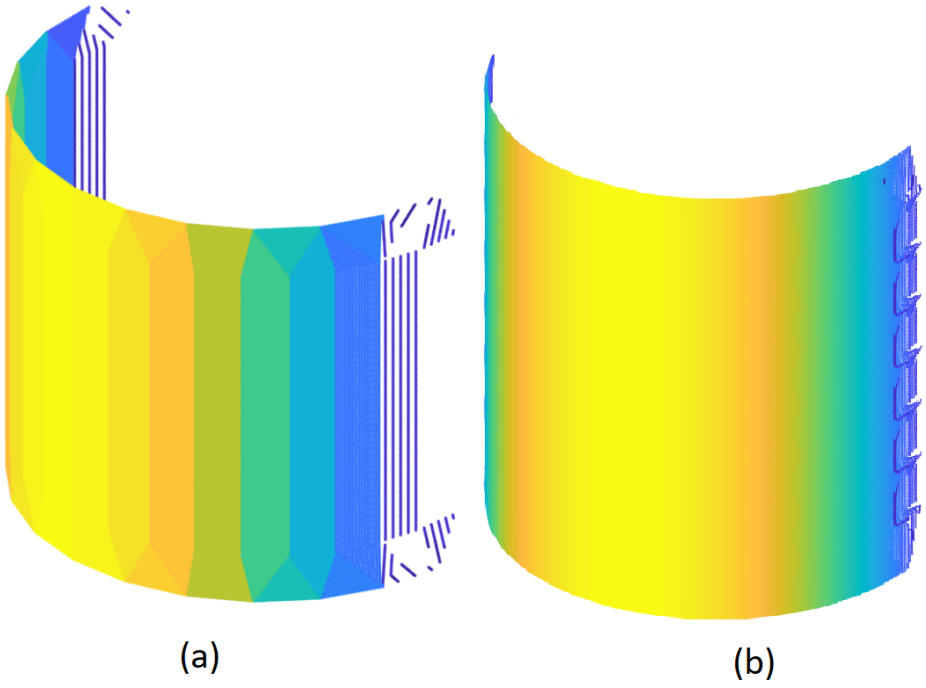

Figure 3.28: The hitting points between the rays and the original flat facets of a cylinder in (a) and with the original estimated curved surface in (b). The color is proportional to the cosine of the angle between the ray and the surface,

Table 3.6: The simulated and theoretical RCS of a sphere and a cylinder and the corresponding errors with and without considering the curvature, © 2022 IEEE.

The Object	Sphere	Cylinder
RCS Equation	πr^2	$2\pi L^2 r/\lambda$
RCS Theoretical Value $[m^2]$	0.2827	119.4
Simulated RCS without Curvature Reconstruction $[m^2]$	0.081	433
Relative Error $[\%]$	71.3	262
Simulated RCS with Curvature Reconstruction $[m^2]$	0.276	115
Relative Error $[\%]$	2.3	3.6

3.2.3.6 Conclusion

In this section, the problem of a low-fidelity triangle-based mesh of objects during electromagnetic simulations has been covered. The method first estimates the normals at the vertices by averaging over the neighboring triangles, then the average curvature tensors are estimated, and based on these, the correct hitting points between the rays and the estimated curved surface are found, along with the correct normals at the intersections. The visual results show a clear difference in the figures between the cases with and without curvature approximation. And this is validated by the numerical results where the RCS values match well the theoretical ones, supported by a convergence analysis, reaching high accuracy with an error of $0.3\,\%$. The next section will show another method for ray-tracing, which is to shoot the rays to the centers of the facets.

3.2.4 Ray-Tracing to the Centers of the Facets

In this section, the ray-tracing tool is developed to trace rays from the radar directly to the centers of the triangular facets instead of the uniform rays. This will make it simpler to ensure that rays are not sent to the empty space but only to the object. Therefore, the triangles should be small to get good accuracy, specifically, the edges should not be more than a quarter wavelength, and hence, in our case, at $76\,\mathrm{GHz}$, the limit is $1\,\mathrm{mm}$. When larger triangles are encountered, they will be subdivided into smaller triangles, and then the ray-tracing process is carried out.

Table 3.7: Convergence results: RCS and error values for a range of the parameter SD, © 2022 IEEE.

SD (Surface Deviation)	n of facets	RCS [m^2]	Error [%]
30	56	0.881	211
15	112	0.508	79
5	352	0.384	35
2	864	0.356	25
1.5	1136	0.233	17
1	1704	0.276	2.3
0.5	3304	0.284	0.4
0.1	16108	0.282	0.3

Fig. 3.29 shows an object composed of both small and large triangles, where the large triangle is subdivided into smaller ones, and rays are sent to the centers of these small triangles.

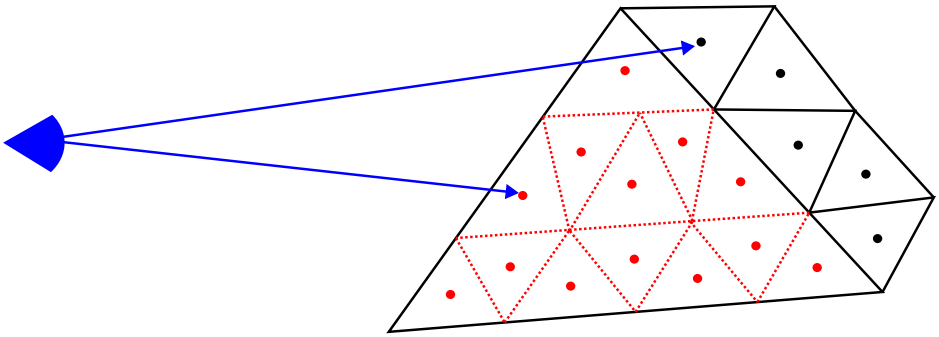

Figure 3.29: Mesh of varying sizes of triangles. Rays are sent to the centers of the triangles or the centers of the subdivided triangles when they are larger than required.

This method is tested with a sphere with a radius of $0.3\,\mathrm{m}$ and a cylinder with the same radius and a height L of $0.5\,\mathrm{m}$ at a frequency of $76\,\mathrm{GHz}$, and they are meshed as suggested earlier with maximum surface deviation (SD) of $0.01\,\mathrm{mm}$, which results in triangles that are larger than the criterion, and thus they need subdivision as a first step. The results are listed in Table 3.8 As can be seen,

Table 3.8: The simulated and theoretical RCS of a sphere and a cylinder and the corresponding errors.

Object	Theoretical RCS Value [m^2]	Simulated RCS Value [m^2]	Relative Error [%]
Sphere	0.2827	0.285	0.81 %
Cylinder	119.4	119.2	0.17 %

the errors are very small in this case, which validates the method. Next, the multi-bounce functionality will be implemented.

3.2.5 Implementation of the Multi-Bounce Feature

Rays can hit the object, reflect off the surface, and hit another part of the object or another object. This is called multi-bounce propagation. It is implemented here

in a way that at each hit location, the scattered electromagnetic field at the Radar receiver is calculated and added to the overall response.

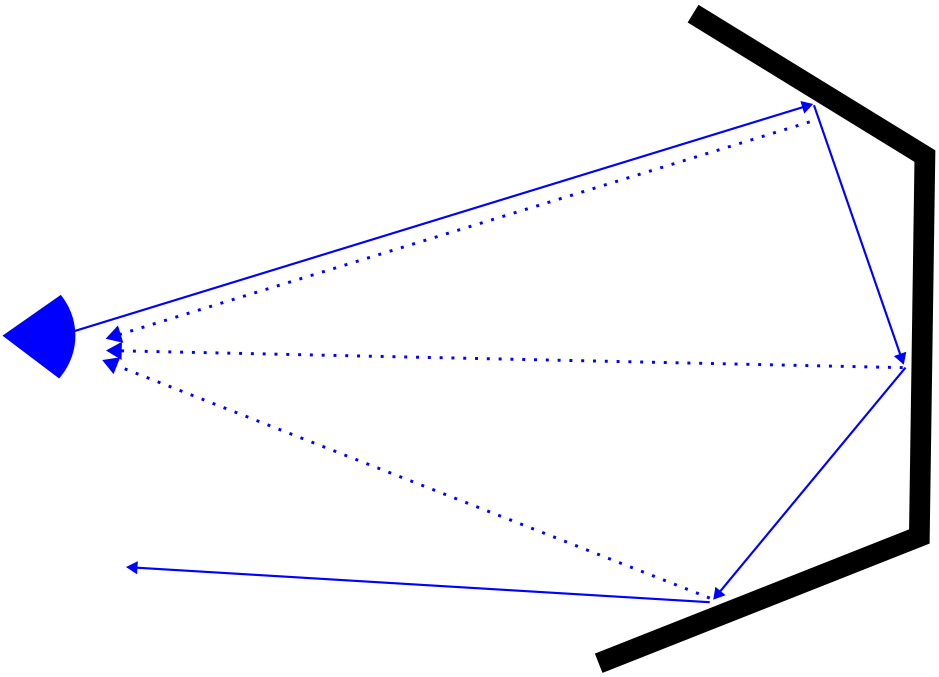

Figure 3.30: Multi-bounce: rays are sent to the object, reflect off the surface, and hit other parts, and the scattered fields are gathered at the antenna from each bounce.

This feature is implemented before the curvature extraction method. Therefore, it does not consider the curvature of the surface, and the testing is done with objects with flat surfaces.

To validate the implementation, two objects are tested that have a theoretical equation to calculate their RCS. The first is a corner reflector, which is like a pyramid with its base removed, with an edge length of $161\,\mathrm{mm}$ (Fig. 3.31a). The second is a dihedral corner reflector, which is like two plates with an angle of $90\,\mathrm{deg}$ between them with dimensions (a,b) of $20\,\mathrm{mm}$ (Fig. 3.31b). The equation for the RCS of the corner reflector with edge a is [40]

$$RCS_{CR} = \frac{4\pi a^4}{3\lambda^2}, \tag{3.46}$$

and for the dihedral corner reflector with dimensions (a,b) as shown in the figure, it is [41]

$$RCS_{Dihedral\ CR} = \frac{8\pi a^2 b^2}{\lambda^2} \tag{3.47}$$

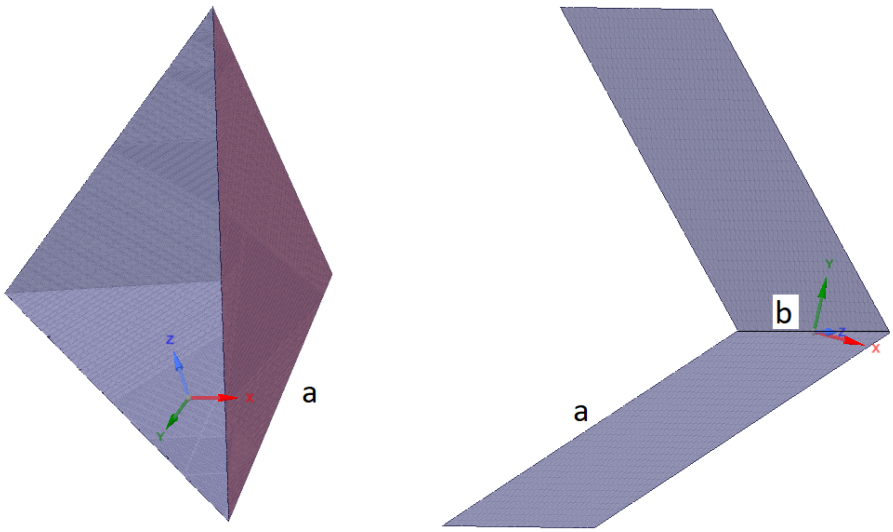

Figure 3.31: Picture of a corner reflector and a dihedral corner reflector.

The simulated RCS values at a frequency of 76 GHz along with the theoretical values and the errors are listed in table 3.9. As can be seen in the table, the errors

Table 3.9: The simulated and theoretical RCS of a corner reflector and a dihedral corner reflector, and the corresponding errors.

Object	Theoretical RCS Value $[m^2]$	Simulated RCS Value $[m^2]$	Relative Error [%]
Dihedral corner reflector	0.2644	0.268	1.36 %
Corner reflector	182.8	180	1.5 %

are small, which validates the implementation. The next step is to implement the multi-path functionality.

3.2.6 Implementing the Multi-Path Feature

In automotive scenarios, objects are rarely in free space; rather, they are located on the ground. Therefore, when simulating realistic scenarios, the effect of the

ground on the return signal of a radar should be accounted for. The effect of the ground results in the multi-path phenomenon, where the signal between the radar and the object travels through two different paths: the direct path and the indirect path, where the signal hits the ground between the radar and the target, as shown in Fig. **??**.

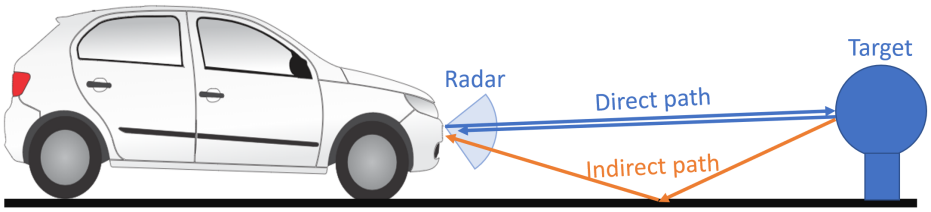

Figure 3.32: Multi-path scene where the direct and indirect paths are shown.

This causes the signal between the radar and object to go and come back in four routes, namely direct-direct, meaning the signal travels from the antenna to the object and returns back without ground effect. The direct-indirect path, where the signal travels from the radar to the object and then reflects off the ground before hitting back the antenna. The indirect-direct path, where the signal travels in the opposite direction to the direct-indirect one. And the indirect-indirect path, where the signal reflects off the ground in both directions, as depicted in Fig. 3.33. This problem is studied in literature including [42] [43] [44] [45]

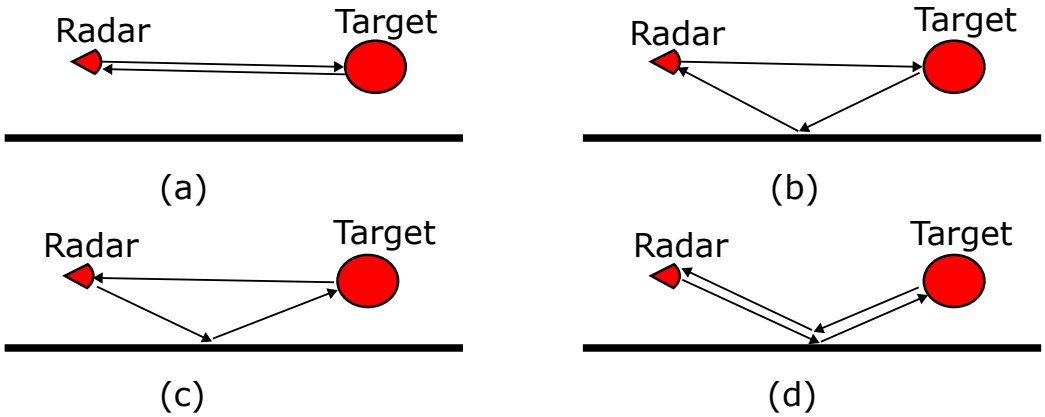

Figure 3.33: Four-path cases: (a) direct-direct, (b) direct-indirect, (c) indirect-direct, (d) indirect-indirect.

[46]. It is dealt with in various ways, including the utilization of half-space Green's function, using the method of moments, or the SBR/PO method. In our method, the response of the target is calculated at a mirror of the antenna and multiply the resulting electric field by the ground reflection coefficient. The

difference between the developed method and Green's function is that in the latter, the currents induced on the object are mirrored with respect to the plane. In addition, the rays are traced from the radar to the facets' centers instead of sending uniform rays, which ensures that no rays are sent into space, and thus miss the object. The fields from the four paths interfere with each other at the receiver antenna, which results in peaks and troughs depending on the relative phases. When performing RCS measurement over range, the RCS profile will have a shape depending on the target shape and height. Therefore, this shape can be used to estimate the height of targets in driving scenarios. The resulting technique to account for multi-path propagation effects of any target is split into two stages: In the first stage, the whole object is traced using the center of the facets as ray-tips and using ray-tracing, it is found whether every facet is in the lit region by direct path (there is direct line of sight from the antenna to the center) or indirect path (the is a line going from the antenna and reflects off the ground specularly, and then hit the facets center). This information is stored for the next stage to reduce computations, along with other information like the reflected rays and the virtual currents. In the next stage, the algorithm starts from each reflected ray and virtual current to perform multi-bounce calculations until the ray exits the bounding box of the object or the number of reflections reaches the maximum. The flowcharts of both stages are shown in Fig. 3.34 and Fig. 3.35, respectively.

3.2.7 Test Results

To validate the complete simulation method 3.2, first, it is compared with the simulation in HFSS using the SBR+ method. The simulation in HFSS is done in two ways. In the first, the actual ground is included in the model, and in the second, the ground is removed and the antennas are mirrored to account for the four-path model. The ground model in HFSS is a flat plane with a rectangular shape and specific material that is meshed like other objects in the scene and participates in the ray-tracing process, as shown in Fig. 3.36.

Two objects are used, a sphere with a radius of $0.3\,\mathrm{m}$ and a corner reflector with an edge side of $161\,\mathrm{mm}$, which has at a frequency of $76.5\,\mathrm{GHz}$ an RCS of $22.7\,\mathrm{dBsm}$. The scenario is a range sweep from $1\,\mathrm{m}$ to $200\,\mathrm{m}$. The results for the sphere are shown in Fig. 3.37, and for the corner reflector in Fig. 3.38. It can be seen from the plots that in both cases, the results from the ray-tracing tool and HFSS considering virtual ground are almost identical from a range of $20\,\mathrm{m}$ up to $200\,\mathrm{m}$. The reason for the deviation before that range is the resolution, because the lower the range, the higher the frequency of the nulls in the profile, which requires an increasingly much lower step size to capture the shape correctly, as shown in Fig. 3.39.

However, in the case of the sphere, the case of actual ground matches only up

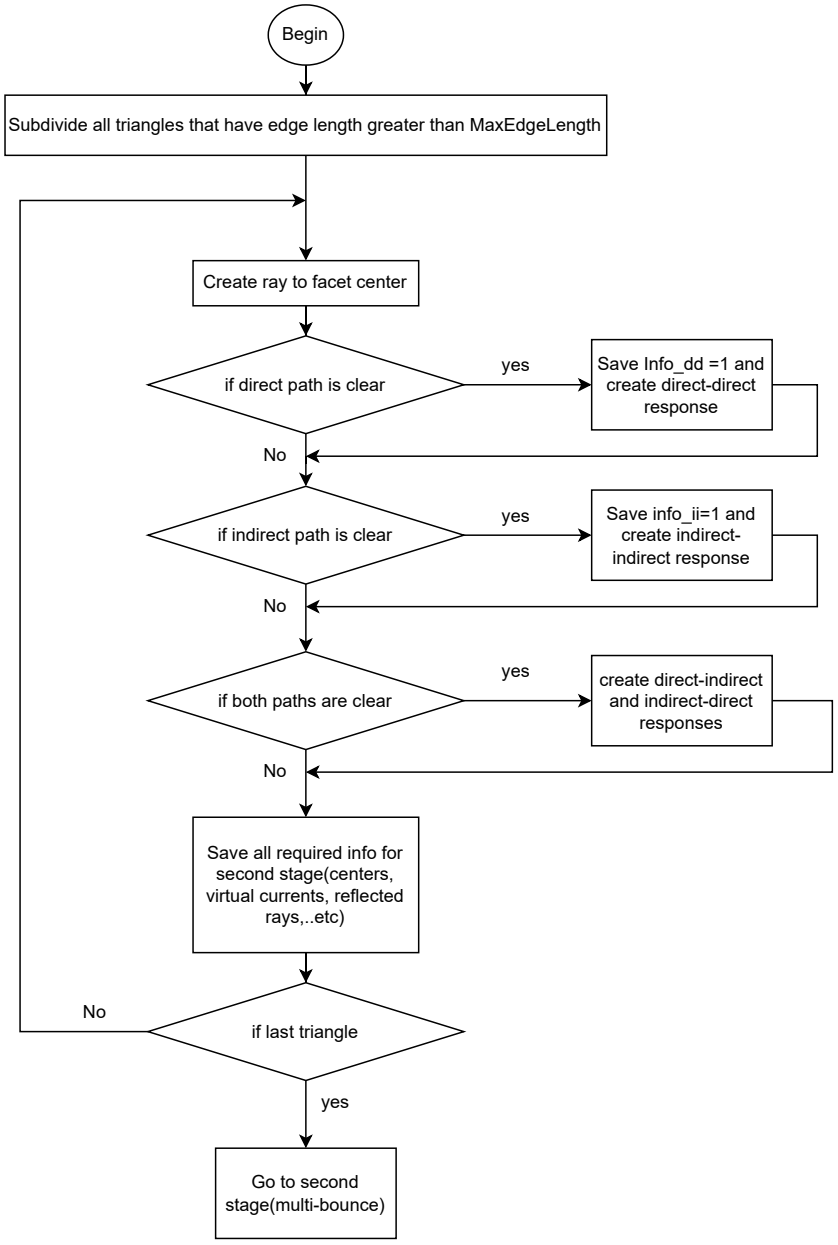

Figure 3.34: Flowchart of stage 1 of the simulation method.

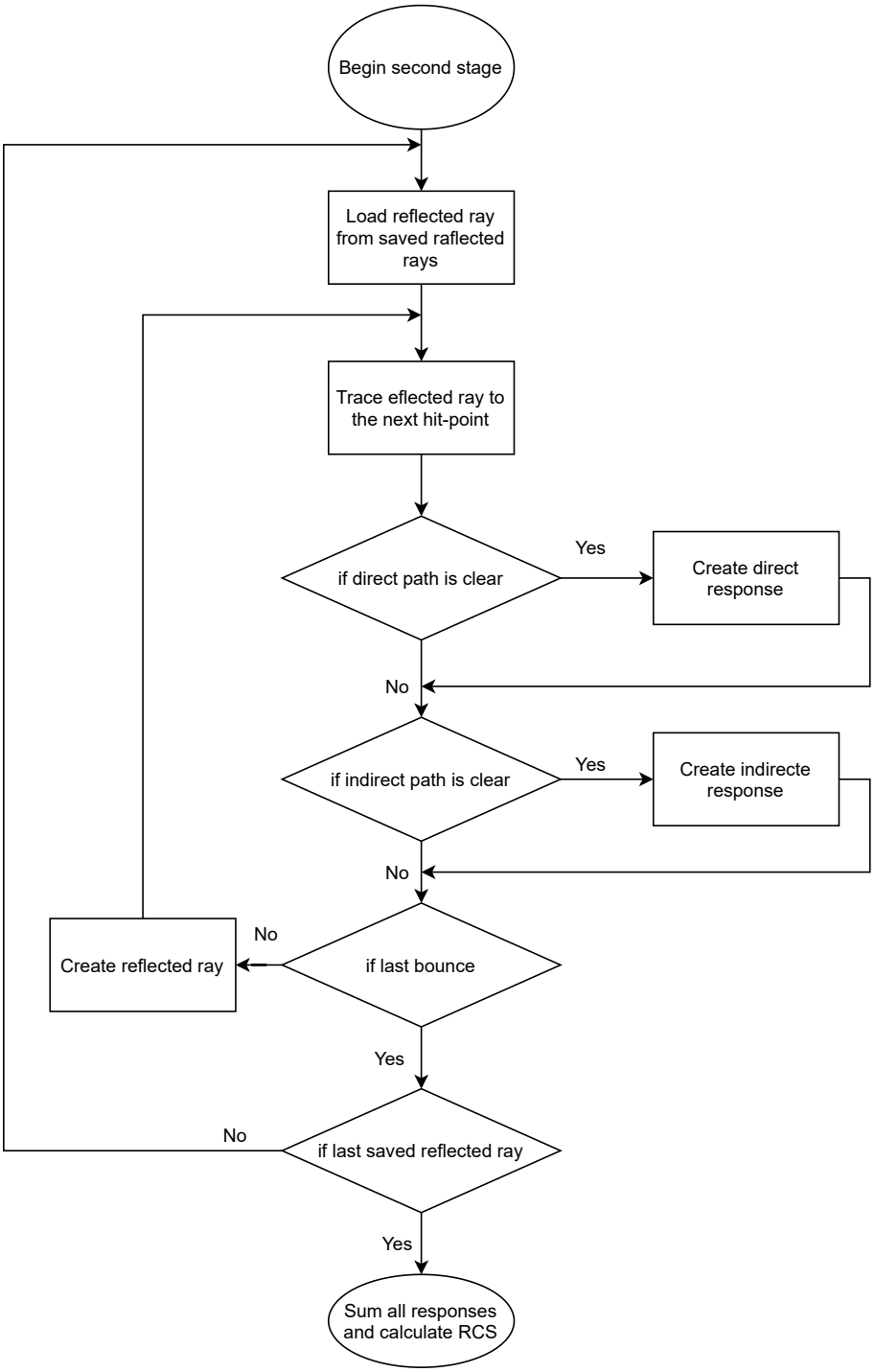

Figure 3.35: Flowchart of stage 2 of the simulation method.

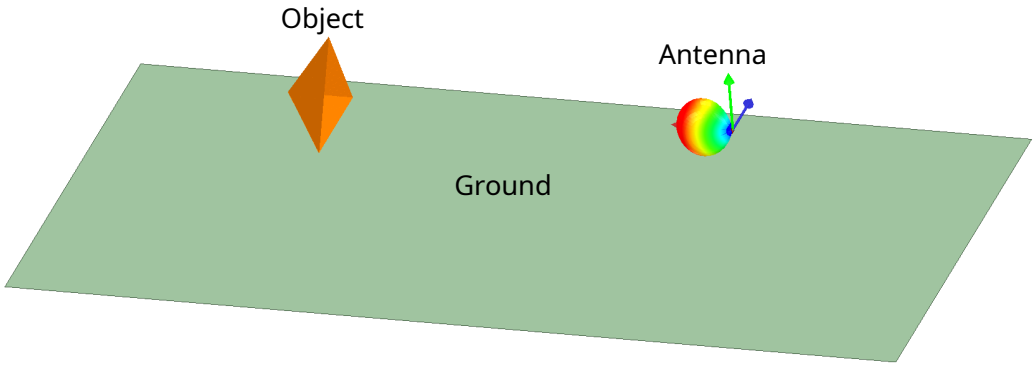

Figure 3.36: Simulation setup including the ground.

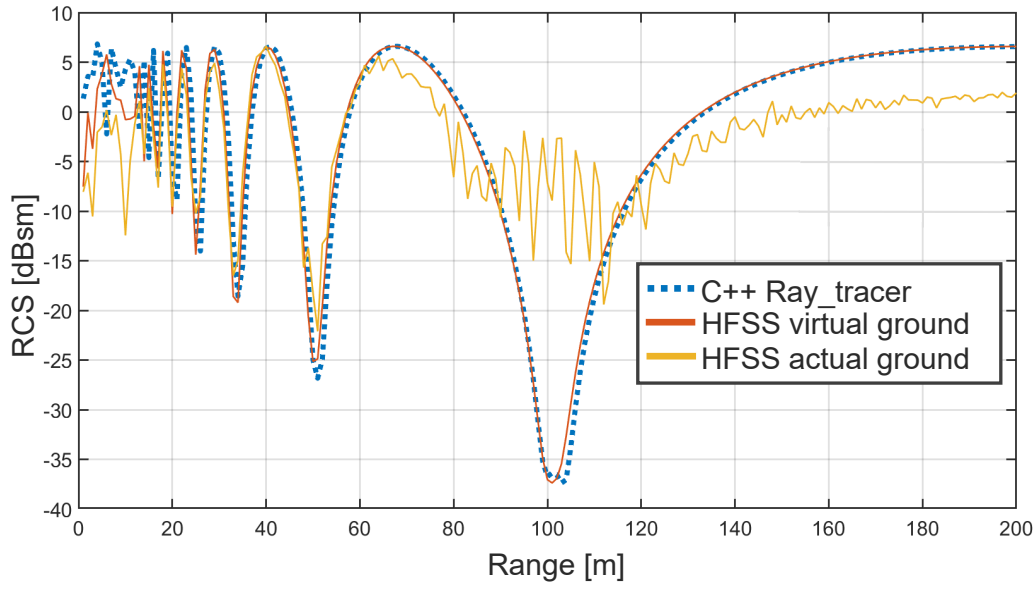

Figure 3.37: RCS of a sphere from $1\,\mathrm{m}$ to $200\,\mathrm{m}$. Comparison between own ray-tracer tool and HFSS/SBR+ with both virtual and actual ground.

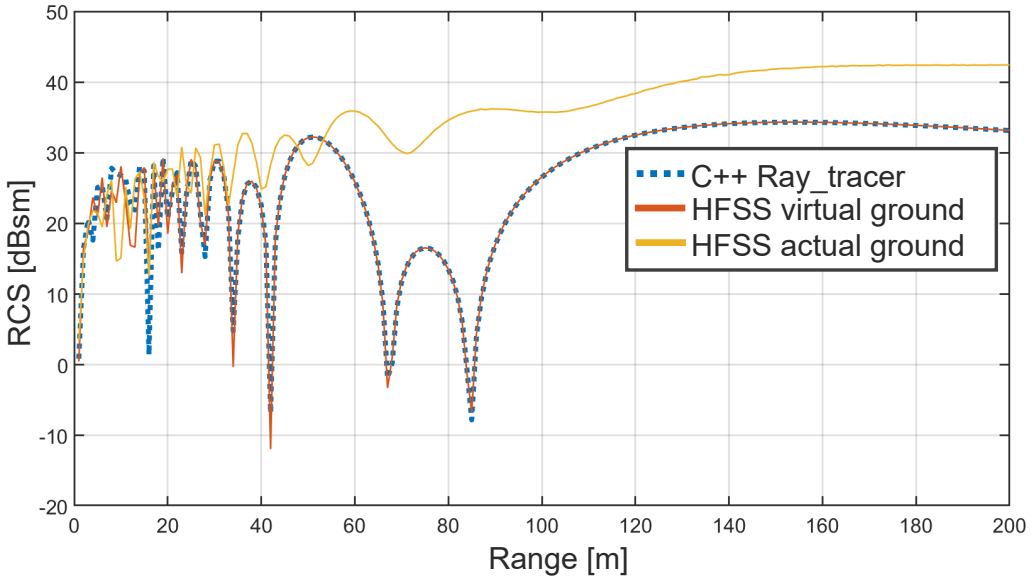

Figure 3.38: RCS of a corner reflector from $1\,\mathrm{m}$ to $200\,\mathrm{m}$. Comparison between own ray-tracer tool and HFSS/SBR+ with both virtual and actual ground.

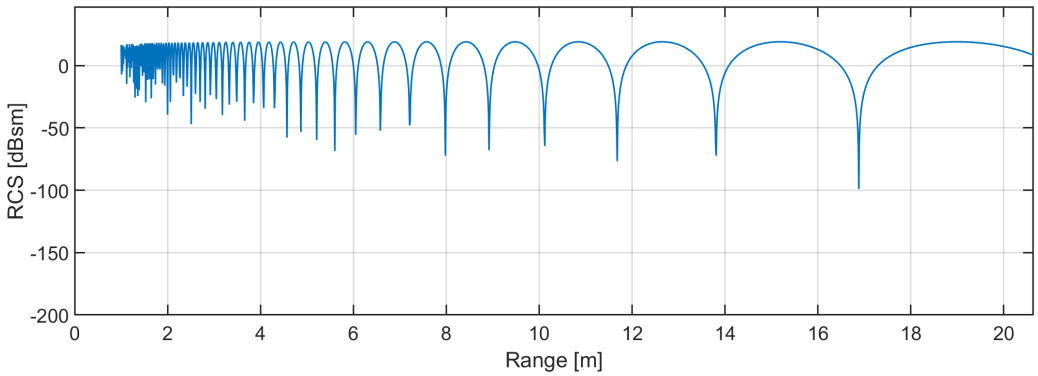

Figure 3.39: The lower the range, the higher the frequency of the nulls in the range-profile.

to $60\,\mathrm{m}$ and then it oscillates away from the other two. In the case of the corner reflector, the results do not match entirely. The reason for the worse results when including the ground is that the density of the rays is determined depending on the first object they hit. If the criterion is set as four rays per wavelength, the default and recommended settings in HFSS, then for the rays that hit the ground first, this condition will be satisfied on the location of the first hit, but when the rays reach the object at a large distance from the hit-point, the rays will have diverged and the distance between two rays will be greater than quarter wavelength, thus less dense than the required criterion as shown in Fig. 3.40.

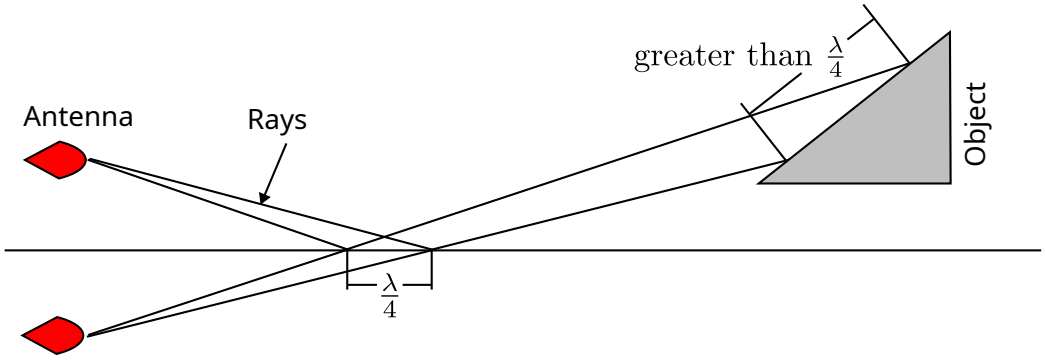

Figure 3.40: Rays that satisfy the criterion of four rays per wavelength on the ground do not satisfy it on the object after reflection.

Therefore, our ray-tracing tool is compared with corresponding data from measurement, and the result is shown in Fig. 3.41. As can be seen, the measurement from a range of $40\,\mathrm{m}$ up to $200\,\mathrm{m}$ matches well. This validates the simulation tool and confirms that it is more accurate compared with commercial software HFSS when including the ground model. The deviation from the simulation in the near range (0 - 40 m) is due to the fact that it has a highly oscillatory behavior at this range, which is difficult to capture in measurements. In the trough (140 - 160 m), it is assumed that the actual ground is not perfect like in the simulation. For one, it has a rough surface and might not be perfectly flat. In addition, the reflection from the road surface has a volumetric component that is not accounted for in the simulation, and also the reflection is partially diffuse, unlike in the simulation, which considers only specular reflection with no phase deviation.

3.2.7.1 Timing

The time it takes for one range sweep (200 steps) using our own tool is $26\,\mathrm{min}{:}7\,\mathrm{s}$, while using HFSS/SBR+ and considering mirroring it is $2\,\mathrm{h}{:}42\,\mathrm{min}$. Both on a

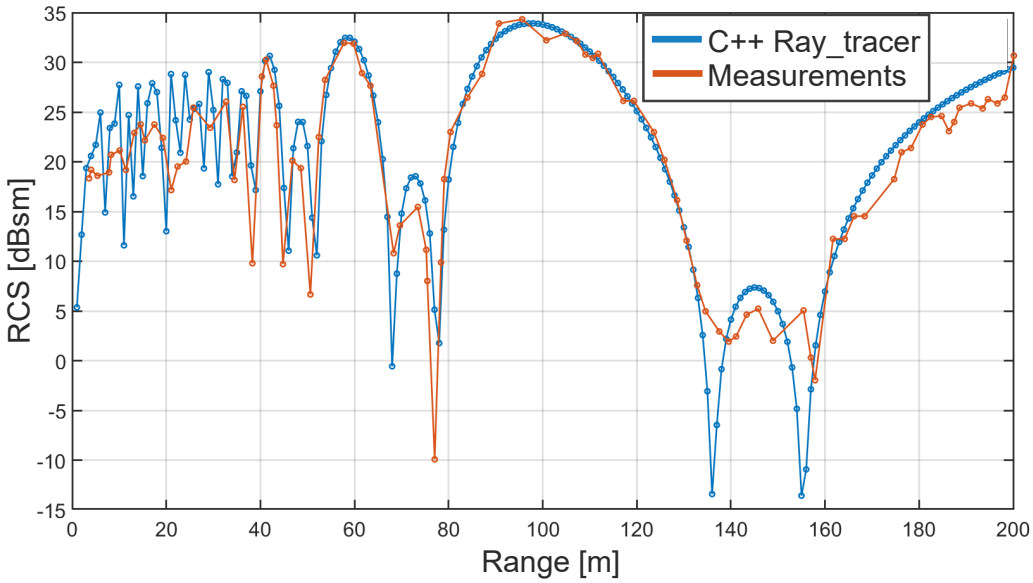

Figure 3.41: RCS of a corner reflector from $1\,\mathrm{m}$ to $200\,\mathrm{m}$. Comparison between the own ray-tracer tool and measurement.

machine with a Core i7 processor using a single core, and 64 GB of memory. On the other hand, in HFSS, when including the ground in the simulation and using 25 cores on an Intel Xeon processor with 512 GB of memory, the time it takes for the sweep is $9\,\mathrm{h}{:}50\,\mathrm{min}$. This shows firstly that our own tool is faster than HFSS/SBR+ in this specific example, and secondly that when including the ground model, the HFSS model is both inaccurate and much slower. Therefore, using our tool for this scenario is advantageous. Additional speedup can be expected when implementing the parallel computing feature to compare with HFSS when using a multi-core processor and a GPU.

3.3 Conclusion

In this chapter, the problem of low-fidelity mesh is presented. An analysis study on the effect of the meshing criterion on the error of the simulation results is shown. Then, a solution is developed where the curvature of the mesh is recovered within the ray-tracing tool and considered to correct the hit-point and the surface normal. After that, the tool is extended by adding multi-reflection and multi-path effects. The RCS results match very well with the other tools and the measurement. The speed of the tool is higher in single-core performance than

HFSS, considering a comparable scenario. Therefore, further development is required to perform multi-core simulation and compare speeds in that case.

To achieve faster speeds, a simpler method is used, which is to represent the car by a scattering point and a radiation pattern. In the next chapter, an extension to this model is proposed, where the single dimension (angle only) radiation pattern is replaced with a two-dimensional (angle and range) radiation pattern, where the multi-path effect is considered as well.

Chapter 4

RCS Radial Map

So far, the usage of a ray-tracing tool with the modified physical optics to generate RCS data has been discussed. Although this method is faster than full-wave methods, there is still a need for a near-real-time simulation method for large scenes. For this reason, usually simpler methods employing point scattering centers are utilized. In this method, an object is represented by its RCS radial pattern instead of the full geometry. This, however, usually does not take the multi-path effect resulting from the ground reflection into consideration. Another factor that affects the RCS of a target is its dimension. For large and complex targets like cars, the near-field region extends to a long distance, covering the entire range of the radar. Therefore, one RCS value for all ranges is not sufficient. In this work, the concept of extending the RCS angular pattern to be a two-dimensional angle-range pattern is presented, and then applying the multi-path effect analytically to the pattern, because adding the ground to the simulation model increases the required time significantly. This approach results in an RCS map that can be used to represent the targets in driving scenario simulations. This work is reprinted, with permission, from [22],

4.1 Radial RCS Simulation

First, the simulation is done using the standard RCS simulation based on the SBR+ method in the commercial tool HFSS, which calculates the far-field RCS values. It is performed in 1° angular steps around a Mustang car model (one model was used for testing). The resulting pattern is shown in Fig. 4.1. The simulated far-field RCS of the car shows a peak of $46\,\mathrm{dBsm}$. This does not correspond to measurement results shown in the literature, which show a peak slightly above $20\,\mathrm{dBsm}$ [47]. This is because the measurements are done in close proximity to the car (less than $10\,\mathrm{m}$), and thus, in the near-field of the car, which is calculated

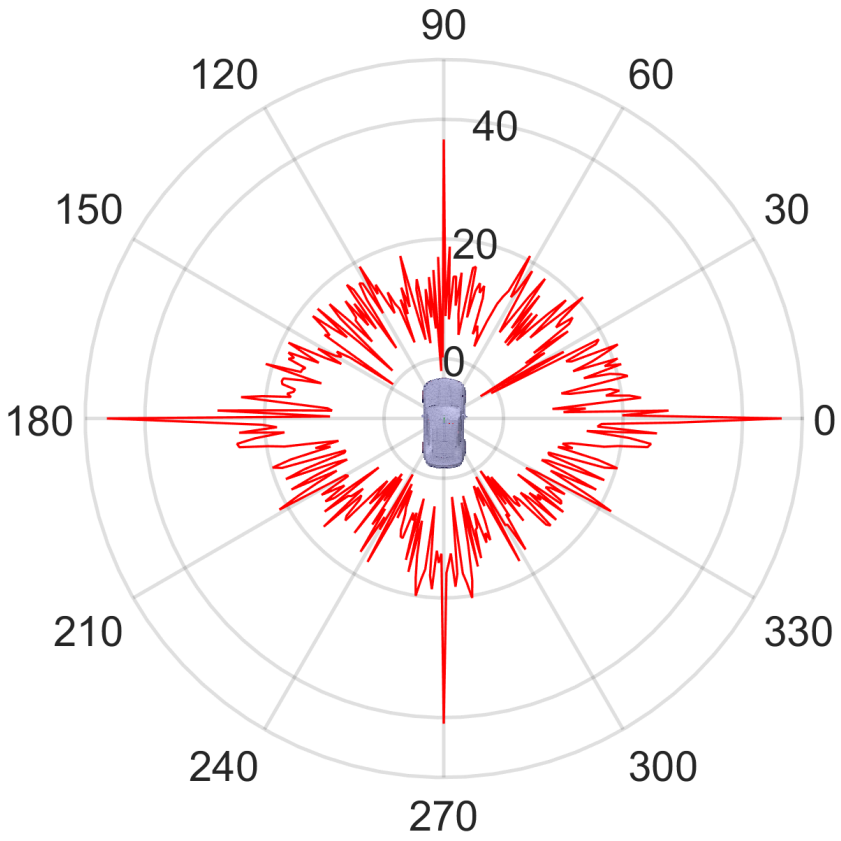

Figure 4.1: RCS pattern of a Mustang car model, © 2022 IEEE.

using the following equation [3, p. 288]

$$d_F = 2\frac{D^2}{\lambda}, \tag{4.1}$$

where d_F is the range at which the far-field region starts, D is the longest dimension of the object, and λ is the wavelength. Calculating it for a car with a length of $5\,\mathrm{m}$, at a frequency of $76\,\mathrm{GHz}$, results in a range for far-field condition of $d_F = 12.8\,\mathrm{km}$. Therefore, the antenna at a distance of $10\,\mathrm{m}$ from the car is clearly in the near-field region. This analysis is verified in the next section.

4.2 Simulation of Car RCS Using Antennas

To verify the previous conclusion, a simulation with actual antennas is done to measure the RCS over a range from $1\,\mathrm{m}$ to $8\,\mathrm{km}$. The antenna is designed as a single inset-fed patch antenna at $76\,\mathrm{GHz}$ for both the transmitter and receiver, which are shifted vertically, and the direct link between them is ignored in the simulation by taking only the scattered part of the signal. The patch with its far-field and E field distribution is shown in Fig. 4.2, and the gain pattern at cross sections of $0\,\mathrm{deg}$ and $90\,\mathrm{deg}$ are shown in Fig. 4.3. HFSS is used to perform the

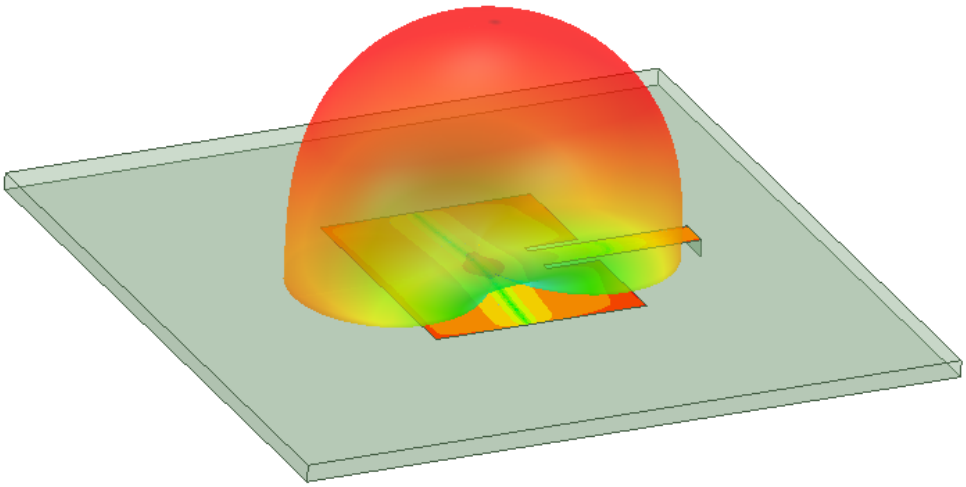

Figure 4.2: Patch with far-field and E field overlay, © 2022 IEEE.

EM simulations. The simulation in HFSS gives the scattering parameters between the antennas, which relate induced voltages on one antenna due to the voltages on the other, and consequently, the electric fields generated by it. Therefore, the

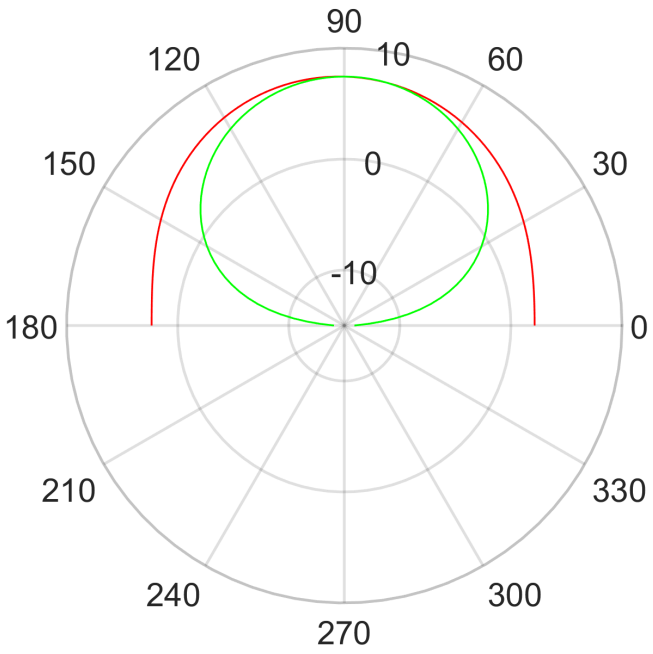

Figure 4.3: Far-field patterns of the designed path antenna. The green, almost closed line is for the vertical plane parallel to the direction of the feed line. The red line is for the plane perpendicular to the former, © 2022 IEEE.

following equation is given [48]:

$$V_{21} = S_{21} \cdot V_1, \tag{4.2}$$

$$\Rightarrow E_{21} = C \cdot S_{21} \cdot V_1, \tag{4.3}$$

where V_{21} is the voltage at antenna two due to voltage V_1 applied to antenna 1, S_{21} is the scattering parameter or coupling between both antennas, $\vec{E}_{21}$ is the resulting electric field, and C is a constant accounting for antenna characteristics like gain and impedance. Therefore, to calculate the RCS from the scattering parameters, the following equation is used [3, p. 584]

$$RCS = \lim_{r\to\infty} 4\pi r^2 \frac{|\vec{E}_{sc}|^2}{|\vec{E}_{inc}|^2}, \tag{4.4}$$

where r is the range, $\vec{E}_{sc}$ is the scattered electric field, and $\vec{E}_{inc}$ is the incident field at the target. But the limit is not taken because the value is estimated by an antenna near the object. This results in the following formula:

$$RCS = 4\pi \cdot r^2 \cdot \left| \frac{\vec{E}_{21}^{sc}}{\vec{E}_{31}^{inc}} \right|^2, \tag{4.5}$$

where $\vec{E}_{mn}$ is the electric field at antenna m resulting from antenna n, and antennas (1,2,3) are shown in Fig. 4.4.

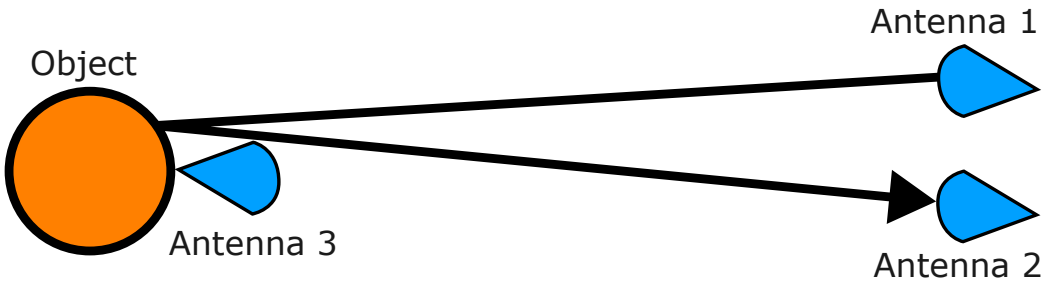

Figure 4.4: The distribution of the three antennas (1,2,3) in the simulation configuration.

The equation for the complex-valued phasor electric field is: [21, p. 55]

$$\vec{E}(r) = \vec{E}_0 \frac{e^{-jkr}}{r}. \tag{4.6}$$

The phase term becomes 1 when taking the absolute value, which shows that $E \propto 1/r$, and therefore by taking the reference value at $1\,\mathrm{m}$, the following is found

$$\left|\vec{E}_{31}^{inc}\right| = \frac{\left|\vec{E}_{31}^{ref}\right| \cdot 1m}{r}, \tag{4.7}$$

$$\Rightarrow RCS = 4\pi \cdot r^4 \cdot \left|\frac{\vec{E}_{21}^{sc}}{\vec{E}_{31}^{ref}}\right|^2 \cdot (1\,\mathrm{m}^{-2}), \tag{4.8}$$

$$\Rightarrow RCS = 4\pi \cdot r^4 \cdot \left|\frac{S_{21}^{sc}}{S_{31}^{ref}}\right|^2 \cdot (1\,\mathrm{m}^{-2}), \tag{4.9}$$

where $\vec{E}_{21}^{sc}$ is the scattered electric field intensity at Rx resulting from Tx, considering scattering off the object's surface, while $\vec{E}_{31}^{inc}$ is the incident electric field intensity at range r, where the target is located, representing the incident field in free space. $\vec{E}_{31}^{ref}$ is the reference signal taken by the exact same antenna at $1\,\mathrm{m}$ to avoid the need to measure the incident field directly and cancel the constant C and voltage V_1 from the equation. To verify the RCS simulation method, a small sphere with a radius of $0.05\,\mathrm{m}$ is simulated for which an analytical formula exists to compare the results. The theoretical result is $0.0079\,\mathrm{m}^2$, while the simulated is $0.0081\,\mathrm{m}^2$ with a relative error of $\sim$2%, which is acceptable for this application. After that, a car model is used for an RCS over range simulation as shown in Fig. 4.5.

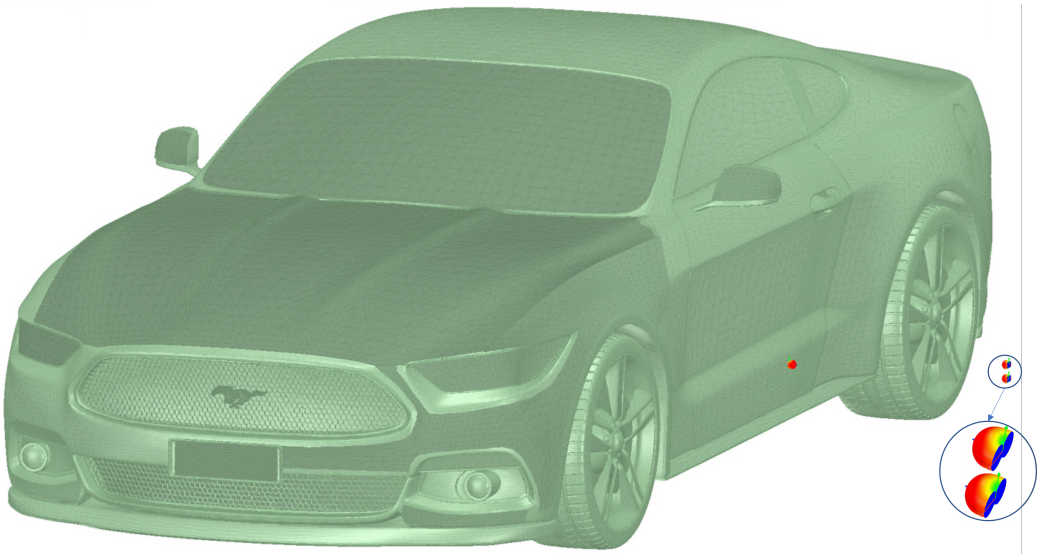

Figure 4.5: A car model and the antennas' far-fields, © 2022 IEEE.

The resulting RCS over range profile is shown in Fig. 4.6 and a zoomed view in Fig. 4.7. It can be seen that the RCS value does converge on a high value

of above $40\,\mathrm{dBsm}$. However, from the zoomed view, it can be seen clearly that the RCS fluctuates significantly in the first $500\,\mathrm{m}$, and in the very near range, up to 100 m, it fluctuates around $20\,\mathrm{dBsm}$ which has a better agreement with the measurements since they are done in close range to the car.

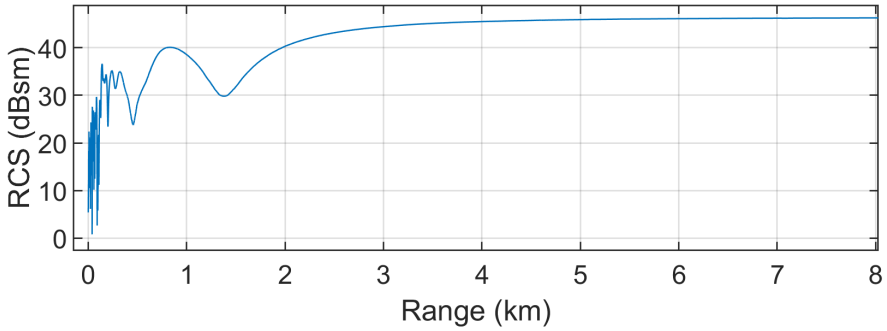

Figure 4.6: RCS over range profile, © 2022 IEEE.

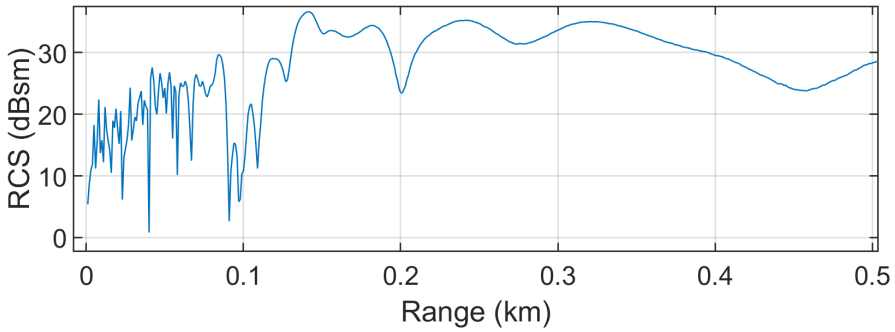

Figure 4.7: RCS over range profile (zoomed), © 2022 IEEE.

4.3 RCS Radial Pattern

In this section, the RCS is simulated around the car in angular step of $3°$, and this is done for the range [$5\,\mathrm{m}$-$500\,\mathrm{m}$] and $30\,\mathrm{km}$. Fig. 4.8 shows the pattern for $10\,\mathrm{m}$ and $30\,\mathrm{km}$. It is shown that the maximum RCS at the far range is almost $50\,\mathrm{dBsm}$, while at the near range is slightly above $20\,\mathrm{dBsm}$, which better corresponds to the measured values.

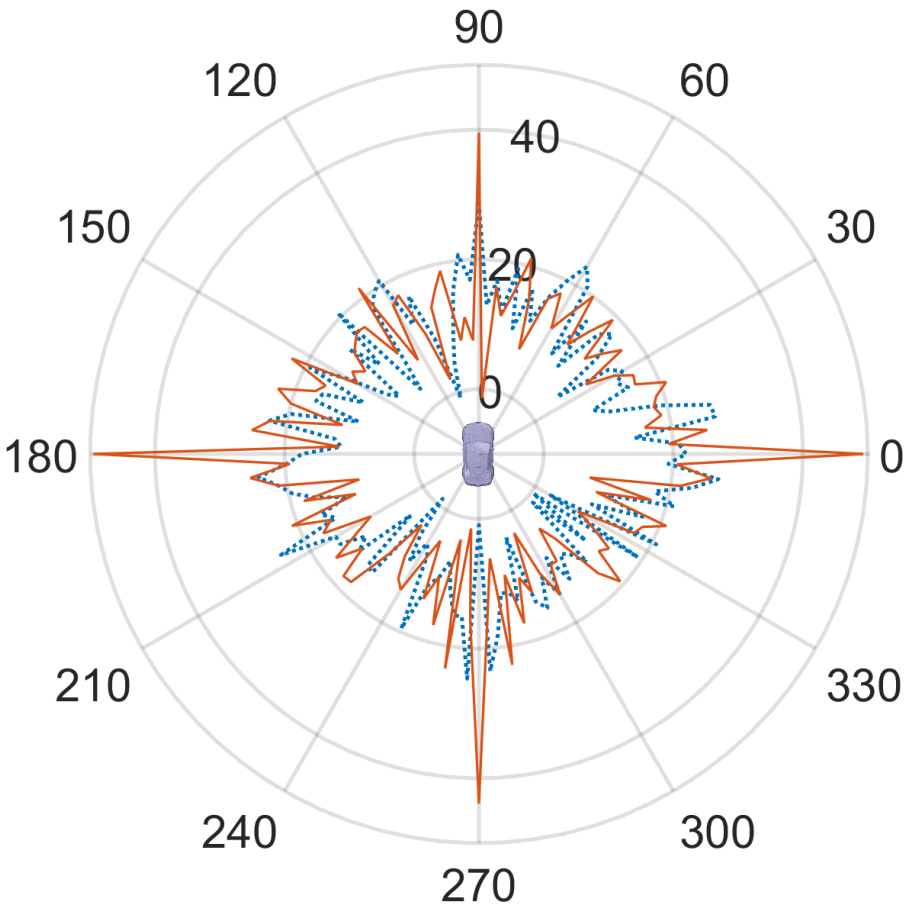

Figure 4.8: RCS pattern of a vehicle model in Fig. 4.5 at $10\,\mathrm{m}$ (blue dotted line) and $30\,\mathrm{km}$ (red solid line), © 2022 IEEE.

4.4 RCS Radial Map with Multi-Path

To include the effect of the ground reflection, the four-path model is applied analytically to the RCS values at each angle and range from the simulated results. The four-path model considers the signal propagation from the transmitter to the target and then reflects back to the receiver in four different paths: direct-direct (dd), direct-indirect (di), indirect-direct (id), and indirect-indirect (ii) as shown in Fig. 4.11. The signal back at the receiver is calculated using

$$\vec{E}_{Rx\_total} = \vec{E}_{Rx\_dd} + \vec{E}_{Rx\_di} + \vec{E}_{Rx\_id} + \vec{E}_{Rx\_ii}, \tag{4.10}$$

where $\vec{E}_{Rx\_p}$ is the signal at the receiver over the path p. The equation (3.7) was reached, which states:

$$\vec{E}_{Rx\_p} = \frac{\Gamma_p C_T \vec{E}_{0Tx}}{L_{1p} L_{2p}} e^{-jk(L_{1p}+L_{2p})}, \tag{4.11}$$

where Γ_p is the reflection coefficient for each path, 1 for dd, the ground reflection coefficient Γ_g for di and id, and $(\Gamma_g)^2$ for ii. L_{1p} and L_{2p} are both calculated geometrically as illustrated in Fig. 4.11. C_T is found to be (3.10):

$$C_T = \sqrt{\frac{RCS}{4\pi}}, \tag{4.12}$$

which is calculated using:

$$C_T = \sqrt{\frac{RCS}{4\pi}} \tag{4.13}$$

$$= \sqrt{\frac{4\pi r^4 \frac{|S_{21}^{sc}|^2}{|S_1^{ref}|^2}}{4\pi}} \tag{4.14}$$

$$= r^2 \left| \frac{S_{21}^{sc}}{S_1^{ref}} \right|. \tag{4.15}$$

We get the S parameters from the simulations. The reference E field $\vec{E}_{0Tx}$ is necessary only if we are interested in the resulting E field. But since here only the RCS is calculated, the reference E field will cancel out and does not affect the result as expected, because the RCS is independent of the E field value transmitted, but depends only on the ratios. Therefore, it can be set to any value, and here it is set to 1.

To increase the accuracy, a prior step, similar to [49] is carried out to extract the contour of the car to shift the scattering center from the origin to the car's

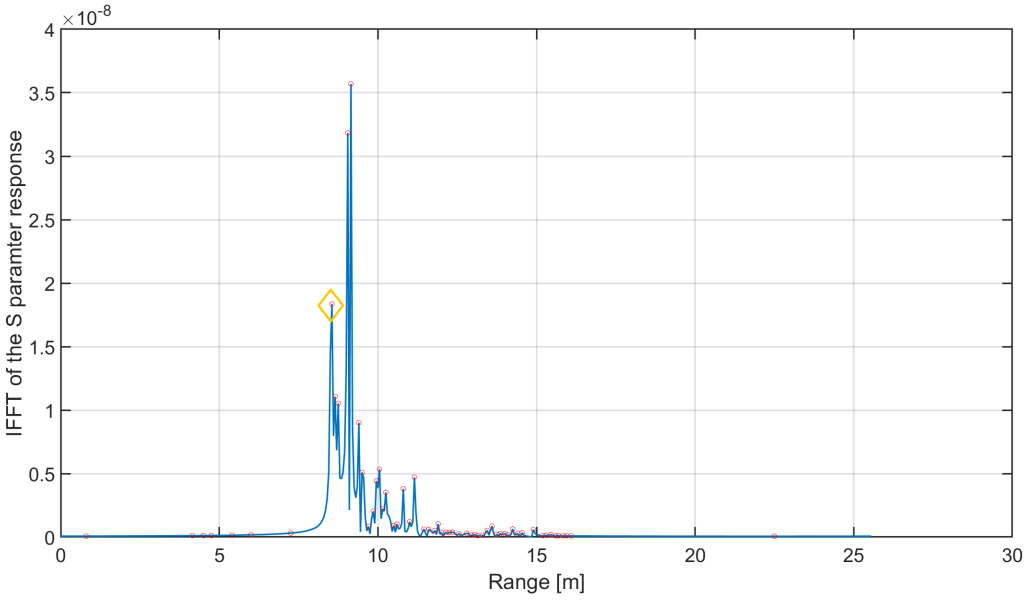

Figure 4.9: The range profile of the car at one angle with the selected peak, © 2022 IEEE.

surface. First, a frequency sweep is performed at each angular step at a range of $10\,\mathrm{m}$ to get the frequency response, then an inverse Fast Fourier Transform (IFFT) is performed to generate the range profile as shown in Fig.4.9.

Afterwards, the range of the first significant peak is taken and stored in a look-up table to be used for correction. The procedure is depicted in the flowchart Fig. 4.10.

Fig. 4.12 shows the resulting contour, and Fig. 4.13 shows the RCS 2D angular pattern with multi-path effect, which is a circular 2D grid around the car with the cells having RCS values at those locations, considering the multi-path effect. On top of this pattern, a range profile is overlaid to show the trough locations.

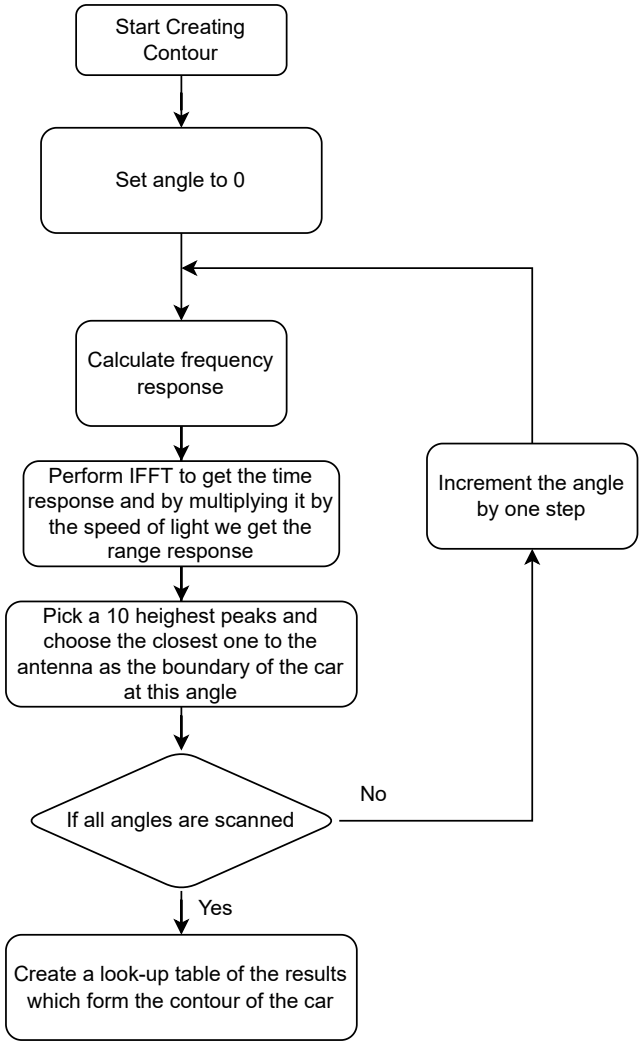

Figure 4.10: Flowchart of the procedure to produce the car contour, © 2022 IEEE.

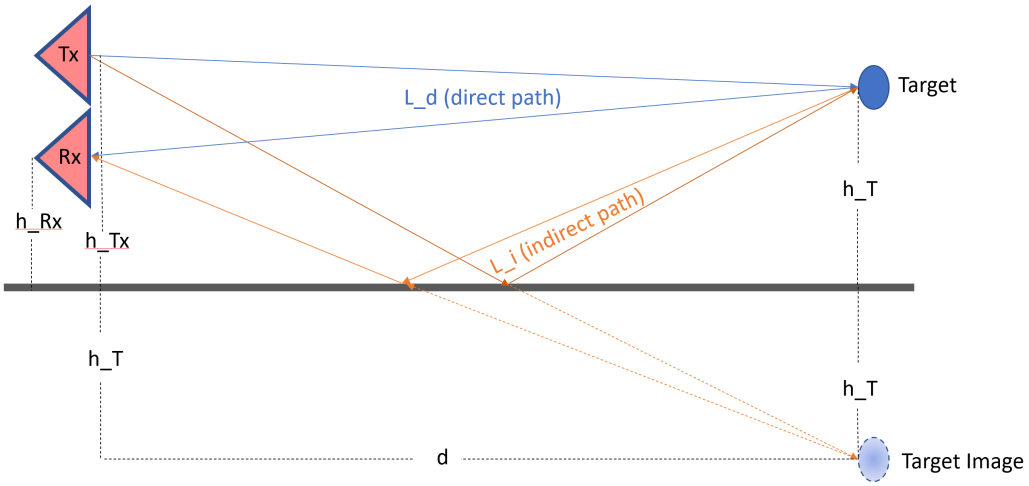

Figure 4.11: Illustration of the four-path model, © 2022 IEEE.

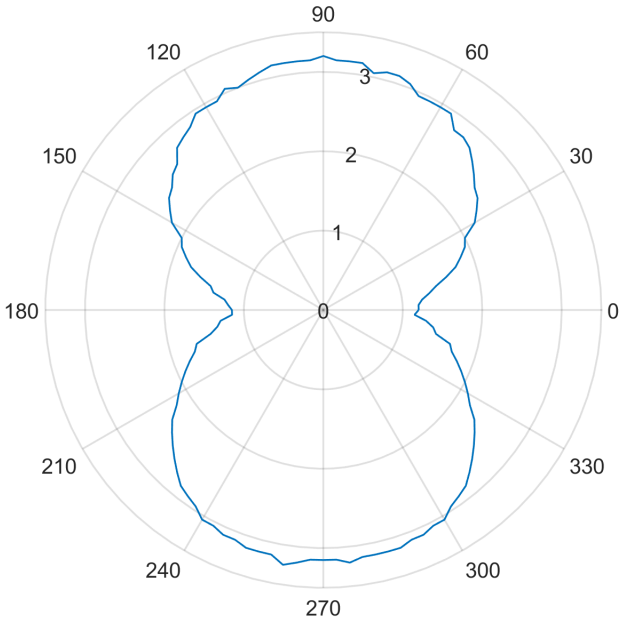

Figure 4.12: The extracted contour of the car's surface, © 2022 IEEE.

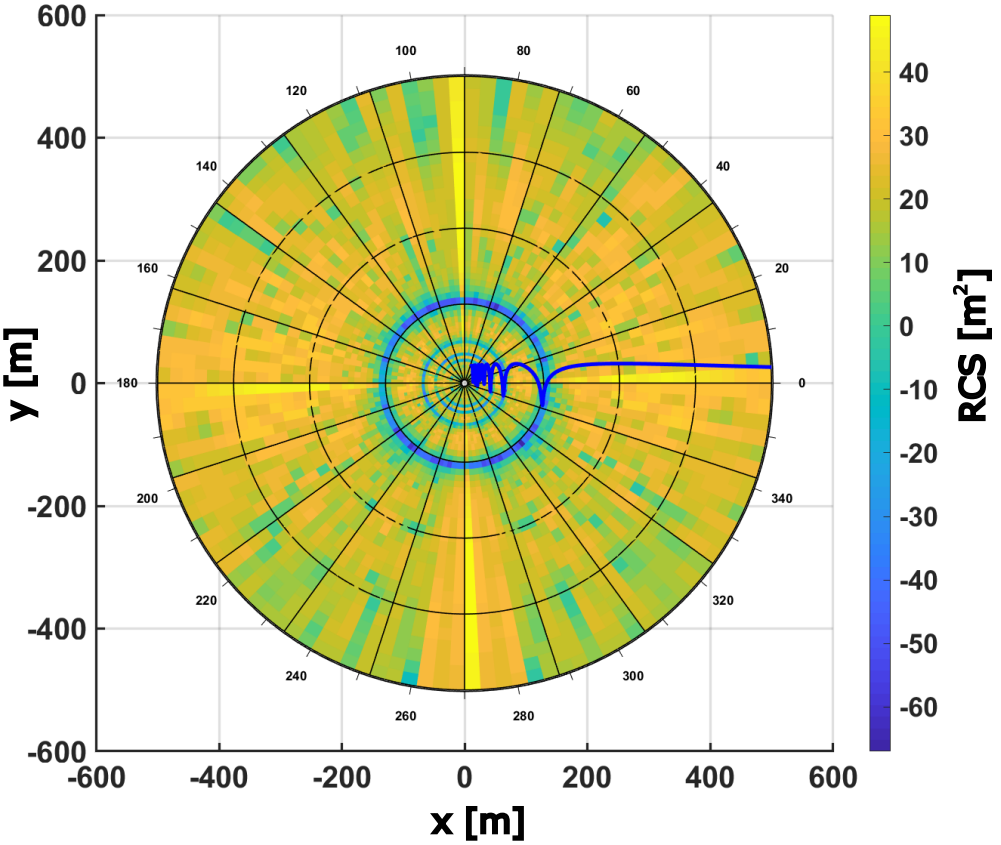

Figure 4.13: RCS 2D pattern/map with multi-path effect for a car with a range profile overlaid on top of it in blue, © 2022 IEEE.

4.5 Conclusion

It has been shown that the far-field RCS simulation of a large object is not suitable for radar simulations due to the near-field effects in close proximity to the target. Therefore, a simulation using actual antennas is performed to better represent the RCS fluctuations over range in the near range. A parametric sweep is carried out in both range and angle using ANSYS HFSS to create the RCS radial map in free space. Then the multi-path effect is applied analytically using the four-path model to account for ground reflections without actual modeling of the ground, which is computationally expensive. This resulted in an RCS radial map considering multi-path effect, which can be used in fast radar simulations without the comparatively demanding ray-tracing methods.

Chapter 5

Ghost Targets

So far, the simulation of radar in free space has been studied, but in reality, the radar in cars is always behind the fascia of the car, which can have a large effect on the radar's signal. In this section, one of the effects of the fascia is studied, which may result in ghost targets.

5.1 Introduction

When integrating a radar sensor array into a vehicle like a car, several issues resulting from the interaction between the sensor and the body of the car have to be dealt with. The effect of the fascia on the antenna pattern is, for instance, studied in [50], [51]. In this study, the ghost targets resulting from the reflection of the radar electromagnetic (EM) waves on the internal structures of the car are studied, such as the crash beam. Fig. 5.1 shows the model of a fascia and a crash beam with the antenna plate. The radar module is mounted behind the fascia on the right-front side of the car as shown in Fig. 5.2

First, a visualization of the rays is created, showing how the waves enter the crash beam, bounce multiple times, then come back to the sensor, resulting in ghost targets. Fig. 2 shows the ray visualization. The tool HFSS from ANSYS is used to perform the simulations.

To perform the electromagnetic simulation, first, an antenna is designed and its far-field is generated to be used in the ray-tracing simulation. The next section is dedicated to designing a patch antenna.

5.2 Designing a Patch Antenna for the Simulation

A patch antenna is chosen for the simulation to keep it simple. It is designed according to [21], and it has been introduced in section 4.2.

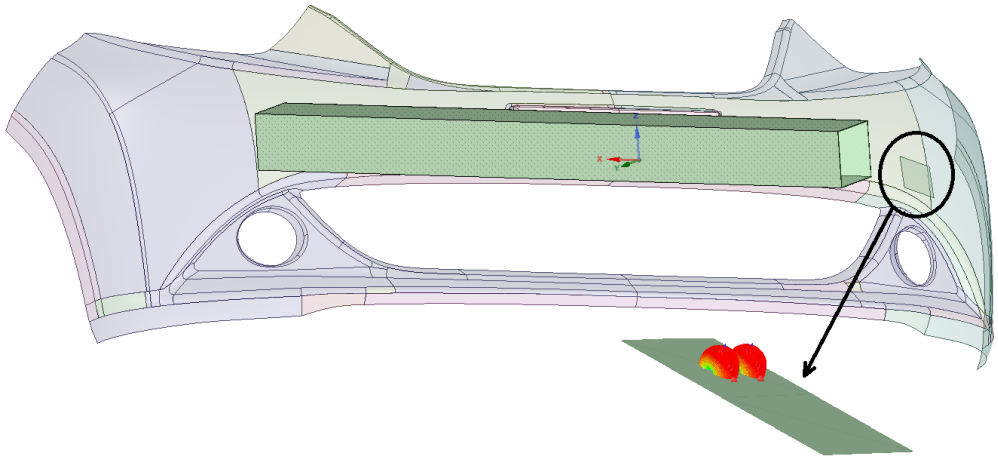

Figure 5.1: Car fascia and crash beam.

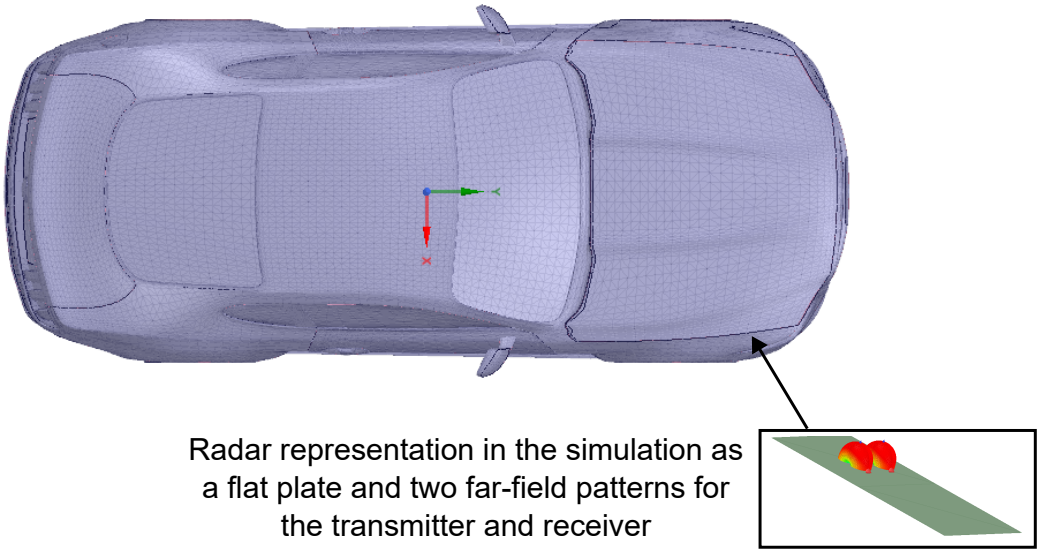

Figure 5.2: Positioning of the radar in the car

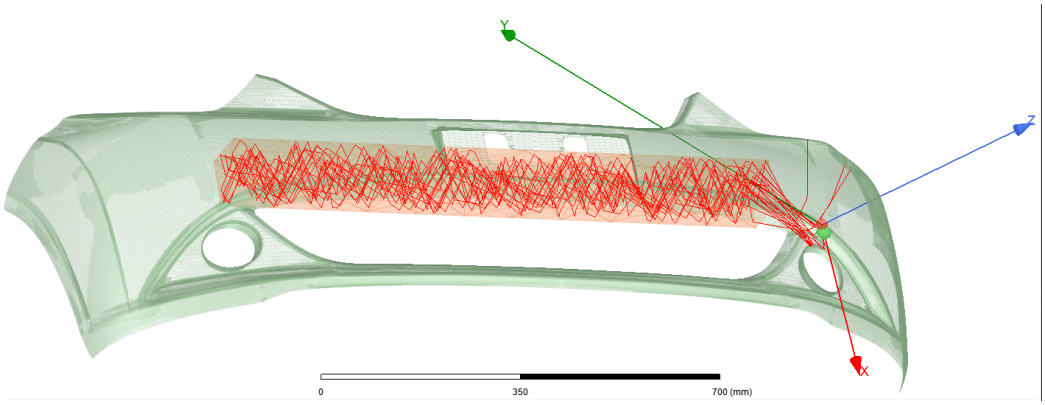

Figure 5.3: Visualization of the rays reflecting inside the crash beam.

5.3 Ghost Target Simulation

After placing the antennas as a far-field pattern, a frequency sweep is performed from $76\,\mathrm{GHz}$ up to $76.5\,\mathrm{GHz}$ with a bandwidth of $500\,\mathrm{MHz}$ and 512 points to quantify this bandwidth. This will give us the environment response in the frequency domain as shown in Fig. 5.4. To get the response in the time domain, an IFFT operation on the frequency response is performed. Multiplying the time by the speed of light results in the response with range as shown in Fig. 5.5. A peak at zero is seen, which is due to coupling between the Tx and Rx antennas, and reflection from the bumper. The other peak is due to the reflections inside the crash beam, as expected from Fig. 5.3. The figure shows rays traveling from the antenna to the crash beam, bouncing multiple times inside until exiting it again from the same opening, reaching the receive antenna and causing the peak shown at around $1.5\,\mathrm{m}$. To know whether this peak causes a detection or not, a threshold needs to be constructed in the next section.

5.4 Applying CFAR

A CFAR (constant false alarm rate) detector is a method to adapt the detection threshold to varying noise and interference levels in a realistic scenario, where these levels are not known beforehand. The main idea is to estimate the noise statistics from the data in real time, so the detector threshold can be adjusted to maintain the desired probability of false alarm P_{FA}, which is the probability that a target detection by the radar is false and there is no target in reality. Its value is chosen to be 0.001 as an acceptable level. Basically, the interference level is measured from the reference cells around the current cell or the cell under test (CUT), leaving a number of guard cells as shown in Fig. 5.6. A cell refers here to

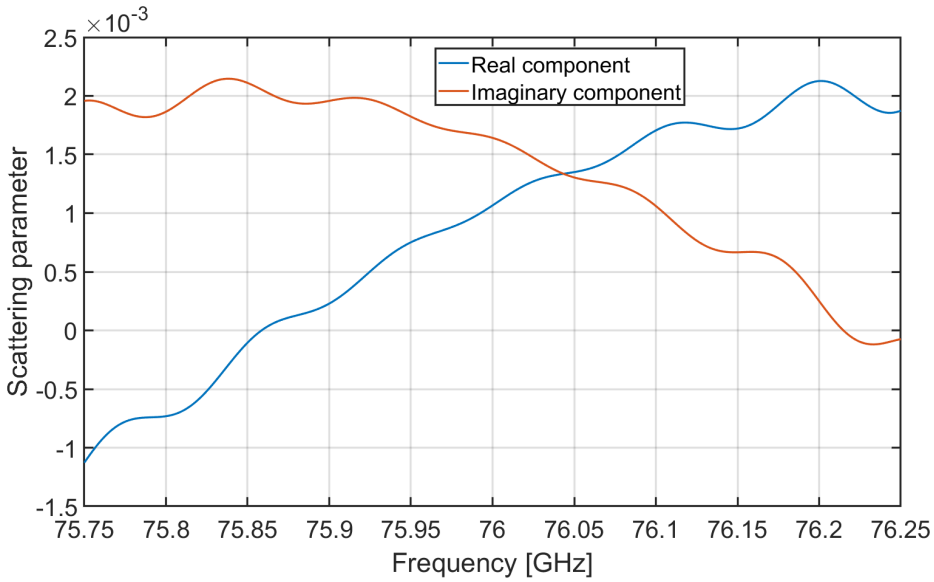

Figure 5.4: The environment response in the frequency domain.

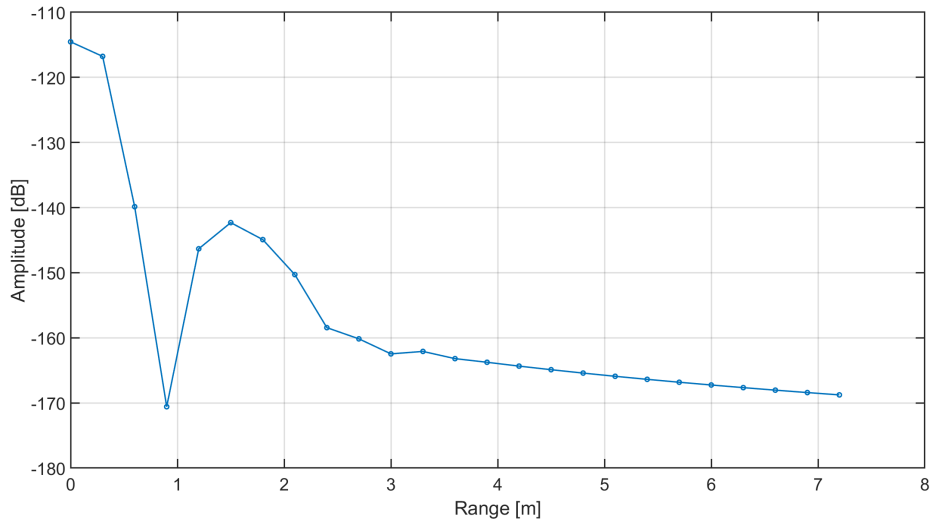

Figure 5.5: The environment response with range. The peak at 1.5 m is due to the EM waves traveling into the crash beam, bouncing multiple times, and returning back to the receiver.

the value in one range bin in the measurement data or the simulation results.

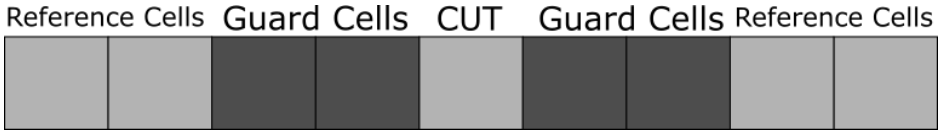

Figure 5.6: CFAR Cells.

One of the most used CFAR techniques is the cell-averaging CFAR or CA-CFAR. In this method, the reference cells are simply averaged to estimate the interference power. The threshold in this case is [52]

$$T = \alpha \frac{\sum_{i=1}^{N} x_i}{N}, \tag{5.1}$$

and the multiplier α is

$$\alpha = N(P_{FA}^{-1/N} - 1), \tag{5.2}$$

where N is the number of reference cells to be averaged. In our application, a variant called the smallest-of CA-CFAR (SOCA-CFAR) is used, which calculates the averages to the left and the right of the CUT and chooses the smallest of them as the reference. This technique reduces the possibility that the reference cells are contaminated with target energy. The implementation by Matlab is used in this case, and the result is shown in Fig. 5.7. It is shown that there is one peak below and one above the threshold line calculated using the mentioned CFAR algorithm, discarding the one at zero because it is mainly due to the coupling between the transmitter and the receiver, and reflections off the bumper surface. Therefore, there is a high probability that the radar will report a false detection (ghost target) at around $1.5\,\mathrm{m}$ due to the internal reflections of the EM waves inside the crash beam and back to the receiver. This needs to be accounted for in the post-processing by either discarding detections at this range, subtracting the energy of the ghost target peak from the measured peak at this range, or other methods.

5.5 Calibration

In order to scale the scattering parameter amplitudes to RCS values, first, a calibration needs to be performed with a known target, and here a sphere is chosen because it is simple and there exists a theoretical formula for its RCS, which additionally does not depend on frequency. The formula for the RCS of a sphere with a radius r is [24]:

$$RCS = \pi r^2. \tag{5.3}$$

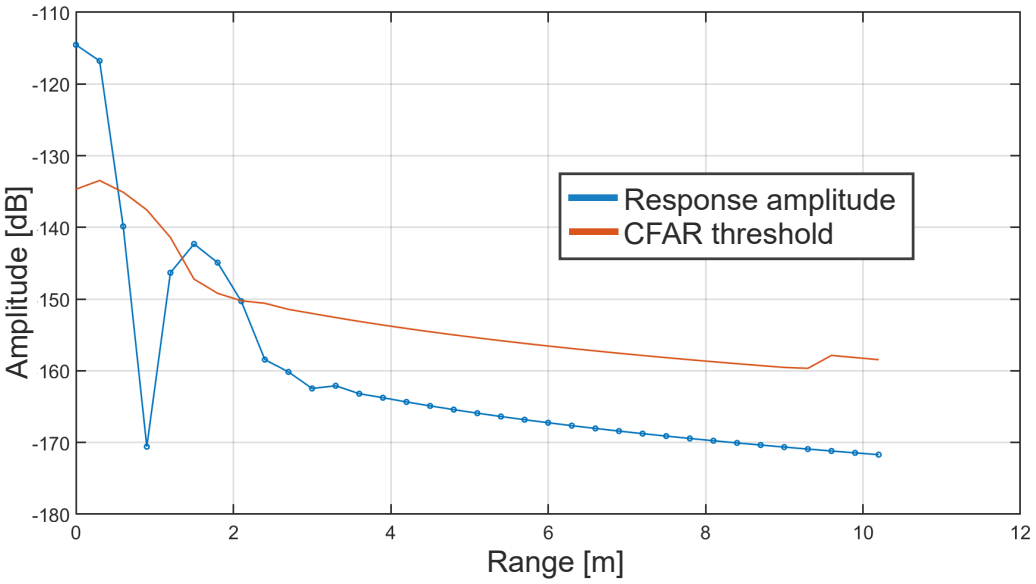

Figure 5.7: The environment response with range and applying CFAR.

The relation between the electric field E at the receiver and the target's RCS is [53]

$$|\vec{E}_{Rx}| = \left[\frac{P_t G^2 \lambda^2 \sigma}{(4\pi)^3 L_s d^4}\right]^{\frac{1}{2}} = k\frac{\sqrt{\sigma}}{d^2}, \tag{5.4}$$

where P_t is the transmitted power, G is the antenna gain, λ is the wavelength, σ is the RCS of the target, L_s are the losses, d is the distance, and k is a constant. Then the relation between the scattering parameter from the transmitter to the receiver S_{12} and the electric field $\vec{E}_{Rx}$ generated by the transmitter and measured at the receiver is

$$S_{12} = \alpha|\vec{E}_{Rx}| = \beta\frac{\sqrt{\sigma}}{d^2}, \tag{5.5}$$

where α and β are constants. Their values are not needed because when the difference is calculated, they are canceled. To perform the calibration in dB, the logarithm of both sides is taken to get

$$20\log(S_{12}) = 20\log(\beta) + 20\log(\sqrt{\sigma}) - 20\log(d^2), \tag{5.6}$$

$$= 20\log(\beta) + 10\log(\sigma) - 40\log(d), \tag{5.7}$$

then the difference is taken:

$$\Delta(20log(S_{12})) = \Delta(C) = 10\log(\frac{\sigma_2}{\sigma_1}) - 40\log(\frac{d_2}{d_1}). \tag{5.8}$$

As a reference, a sphere with radius of $0.05\,\mathrm{m}$ at a distance of $6\,\mathrm{m}$ is used to get C_0 and calculate ΔC for two other spheres: one at the same distance but double the radius ($0.1\,\mathrm{m}$), and the second of the same radius but double the distance (d=$12\,\mathrm{m}$).ΔC is calculated for the second sphere and the result is

$$\Delta C = 10\log(\frac{\pi r_1^2}{\pi r_0^2}) - 40\log(1), \tag{5.9}$$

$$= 2 \cdot 10\log(2) - 0 = 6, \tag{5.10}$$

and for the third sphere, the result is

$$\Delta C = 10\log(1) - 40\log(2), \tag{5.11}$$

$$= -12. \tag{5.12}$$

Figure 5.8 shows the simulation results for the three mentioned spheres, which shows that the difference between the reference sphere and the second sphere is $-172.5 - (-178.5) = 6$, thus validating the first calculation. In addition, the difference between the reference and third spheres is $-190.5 - (-178.5) = -12$, which validates the second calculation.

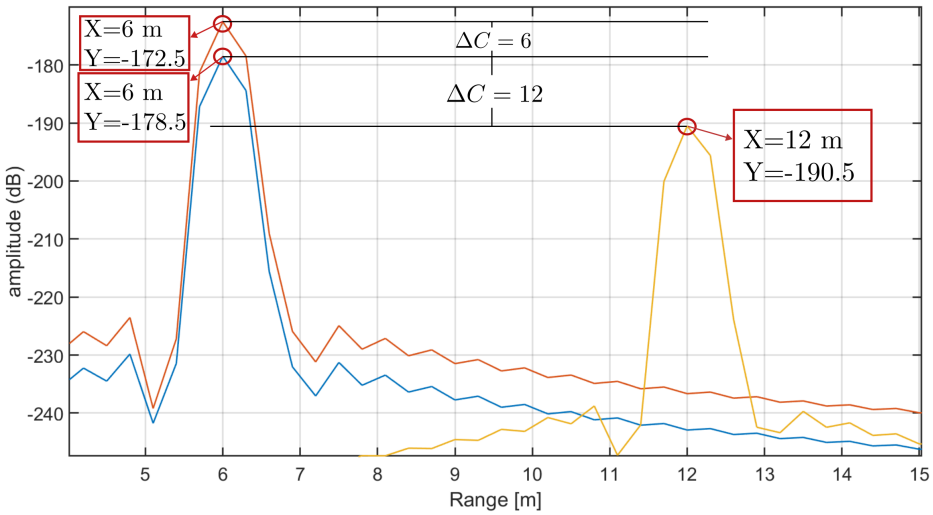

Figure 5.8: The simulation results for spheres with radii of $0.05\,\mathrm{m}$ and $0.1\,\mathrm{m}$ at a range of $6\,\mathrm{m}$ and one with a radius of $0.1\,\mathrm{m}$ at a range of $12\,\mathrm{m}$.

To validate the calibration method with another object, a corner reflector is simulated with an RCS of $22.57\,\mathrm{dBsm}$ over a range from $6\,\mathrm{m}$ up to $150\,\mathrm{m}$ and calculate the measured RCS at every range point. Fig. 5.9 shows the simulation configuration, Fig. 5.10 shows the simulation results, and Fig. 5.11 shows the RCS

found over the simulated range. For comparison, the corner reflector is simulated in an RCS simulation built in the software to get the best estimate of the actual RCS. It is seen that the simulated RCS using the calibration fluctuates around the correct value. The fluctuation is due to several factors. One factor is the fact that the corner reflector is not exactly located at the range bin center but rather in the middle between two range bins, which plays a significant role in the calculation using IFFT. Fig. 5.12 shows peaks that are not centered, but from the flat tops, it is concluded that the actual peak is between the two peaks, which causes the difference in the simulated RCS. Another reason is the fact that when performing an FFT over a period of time that is not an exact multiple of the period, there will be an error in the resulting amplitude.

Using the developed calibration, it is applied to the peak related to the ghost target at a distance of approximately 1.5 m that resulted from internal reflections inside the crash beam with a value of $-144.5\,\mathrm{dBsm}$, the RCS of the peak becomes $-7.94\,\mathrm{dBsm}$.

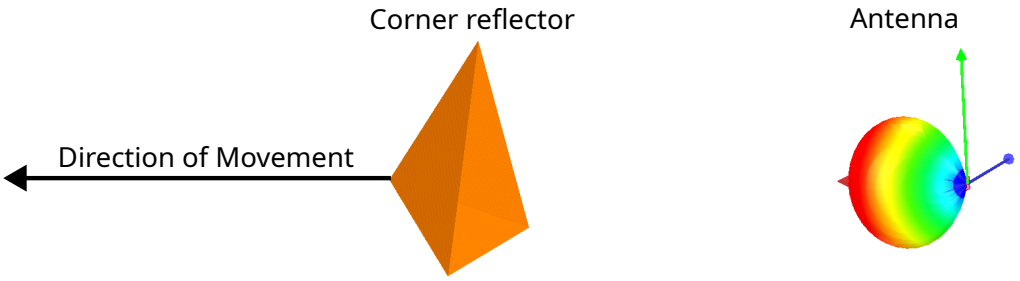

Figure 5.9: The simulation configuration of an antenna and a corner reflector moving away from the antenna each step.

5.6 Conclusion

In this section, the problem of ghost targets resulting from reflections on internal structures is discussed. First, a visualization of the rays is shown, which indicates that the EM waves enter the crash beam, undergo several reflections, then exit it, reaching the receiver antenna. To perform the actual simulation, the previously designed patch antenna is used. A frequency sweep is performed to generate the complex environment response, which, after IFFT, generates the time environment response. By multiplying it with the speed of light, the range profile resulted, which showed a peak at zero corresponding to the direct coupling and reflections from the bumper in front of the antenna. The other peak shown at around $1.5\,\mathrm{m}$ is related to the ghost target resulting from the reflections of the EM waves inside

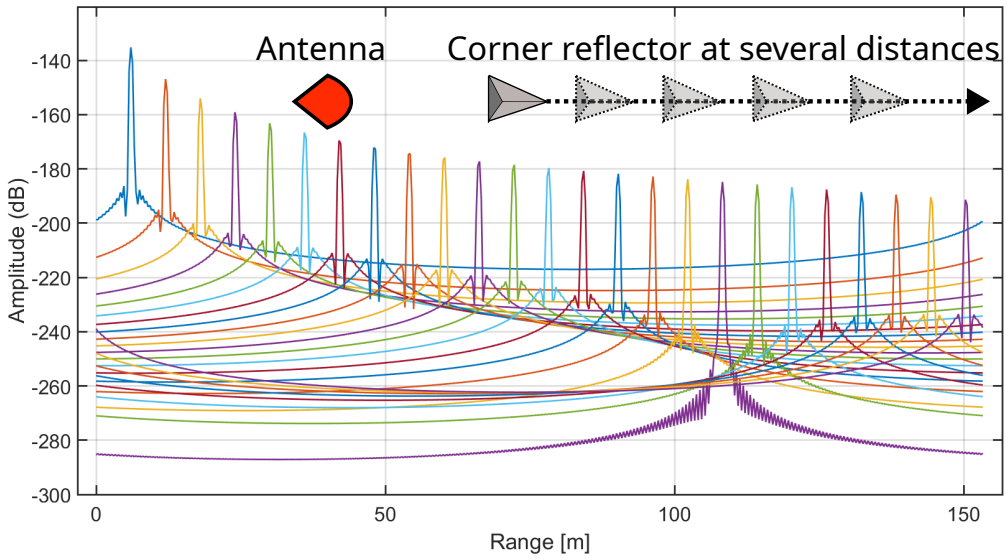

Figure 5.10: Simulated corner reflector over range from $6\,\mathrm{m}$ up to $150\,\mathrm{m}$.

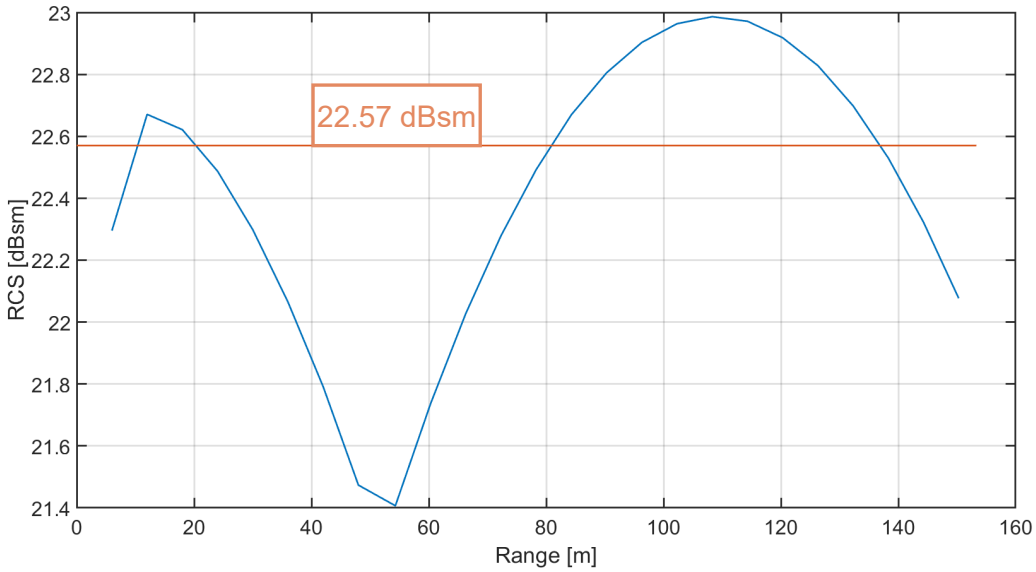

Figure 5.11: Simulated rcs of the corner reflector over range from $6\,\mathrm{m}$ up to $150\,\mathrm{m}$ and its actual RCS at $76\,\mathrm{GHz}$.

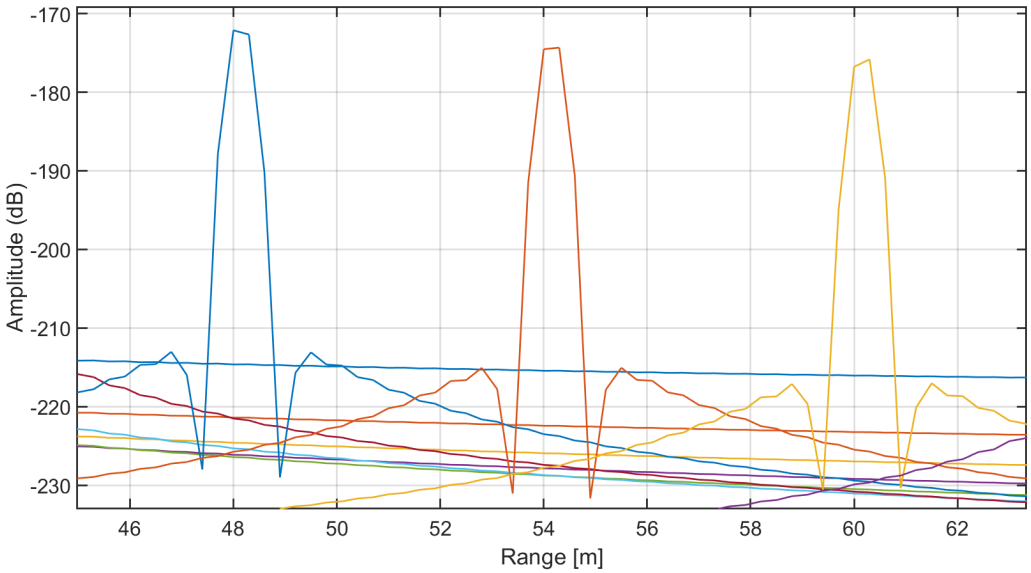

Figure 5.12: Illustration of the fact that the peak is not centered but rather between two range bins.

the crash beam, then traveling back to the receiver. To determine whether there is a high probability of the radar reporting a false target (ghost target), a CFAR threshold is created with the desired probability of false alarm of 0.001. The resulting threshold is below the second peak, indicating that the peak corresponds to a ghost target that needs to be accounted for in the post-processing. To calculate the RCS of the peak, a calibration process is performed, and then by applying it to the available peak, we find the ghost target RCS.

Chapter 6

Conclusion

In this work, a ray-tracing simulation tool is developed using the programming language C++ and the modified equivalent current approximation (MECA) method to generate RCS data that can be used to tune algorithms and train neural networks. This asymptotic method is used due to its efficiency in simulating very large scenarios in terms of wavelength, like driving scenarios with electrically large objects like cars and pedestrians. The multi-path effect is applied without including the ground in the simulation, but rather by assuming a virtual ground and using the four-path model. The multi-bounce effect is accounted for using geometric optics (GO) principles.

Before simulation, an object is transformed into a mesh composed of flat triangles, leading to errors in the RCS because the flat surfaces deviate from the curved ones depending on the meshing criteria. The effect of the criterion ”maximum surface deviation” on the error is investigated, and a figure of merit is developed to mesh objects to have a good balance between the number of mesh cells and accuracy. To handle low fidelity models, a method has been developed that first estimates the curvature of the original object from the mesh, then the intersection point between the ray and the estimated surface is found using the proposed technique. The computed RCS values based on the proposed method were very accurate, validating this method.

To achieve real-time simulation, ray-tracing cannot currently be used. Alternatively, objects are modeled by scattering centers with a radial RCS pattern. It is proposed to extend this pattern to a 2D map by considering the range as well, composing an angle-range dependent RCS map/pattern, and applying the multi-path effect using the four-path model directly without including the ground to avoid time-consuming simulations. The resulting RCS map can be used instead of the object in scenario simulations.

Lastly, one of the effects of the car’s fascia on the installed radar is considered, which is the ghost targets resulting from the internal reflections of the radar

electromagnetic waves on the inner side of the fascia and the internal metal structures of the car. This effect needs to be accounted for in the completed scenario simulator.

6.1 Future Work

To address the limitations and explore the full potential of this approach, future work may focus on:

- For improving the ray tracing tool, parallel computing needs to be implemented, utilizing CPU cores and the GPU to achieve the best performance possible.
- The multi-path and multi-bounce features should be integrated with the curvature extraction method.
- The radiation pattern of the antenna should be taken into consideration for better accuracy in mimicking the radar operation.
- Additionally, the radar module itself needs to be simulated to generate RCS and detection results the same way as in reality, and to allow for more complicated simulation scenarios.

Bibliography

[1] U. Chipengo, P. M. Krenz, and S. Carpenter, "From antenna design to high fidelity, full physics automotive radar sensor corner case simulation," *Modelling and Simulation in Engineering - Wiley Online Library*, vol. 2018, pp. 1–19, December 2018.

[2] R. Garg, "Basic principles of electromagnetic theory," in *Analytical and Computational Methods in Electromagnetics*. Artech house, 2008.

[3] C. A. Balanis, *Advanced Engineering Electromagnetics*. John Wiley & Sons, 2012.

[4] A. V. Osipov and S. A. Tretyakov, "Reflection and transmission coefficients," in *Modern Electromagnetic Scattering Theory with Applications*. John Wiley & Sons, 2017.

[5] J. Gutiérrez-Meana, J. A. Martínez-Lorenzo, and F. Las-Heras, "High frequency techniques: the physical optics approximation and the modified equivalent current approximation (meca)," in *Electromagnetic Waves*. IntechOpen, 2011, ch. 8. [Online]. Available: https://doi.org/10.5772/17307

[6] T. Möller and B. Trumbore, "Fast, minimum storage ray/triangle intersection," in *ACM SIGGRAPH 2005 Courses*. Association for Computing Machinery, July 2005, p. 7.

[7] "A minimal ray-tracer: rendering simple shapes." https://www.scratchapixel.com/lessons/3d-basic-rendering/minimal-ray-tracer-rendering-simple-shapes/ray-box-intersection.html, accessed: 2026-05-01.

[8] T. Akenine-Möller, "Fast 3d triangle-box overlap testing," in *ACM SIGGRAPH 2005 Courses*. Association for Computing Machinery, 2005, p. 8.

[9] E. A. Haines and J. R. Wallace, "Shaft culling for efficient ray-cast radiosity," in *Photorealistic Rendering in Computer Graphics: Proceedings of the Second Eurographics Workshop on Rendering*. Springer, 1994, pp. 122–138.

[10] T. Akenine-Moller, E. Haines, and N. Hoffman, "Intersection test methods," in *Real-Time Rendering*. AK Peters/CRC Press/Tylor & Francis, 2019.

[11] I. Wald and V. Havran, "On building fast kd-trees for ray tracing, and on doing that in O(n log(n))," in *2006 IEEE Symposium on Interactive Ray Tracing*. IEEE, 2006, pp. 61–69.

[12] M. Hapala and V. Havran, "Kd-tree traversal algorithms for ray tracing," in *Computer Graphics Forum*, vol. 30, no. 1. Wiley Online Library, 2011, pp. 199–213.

[13] A. N. Pressley, *Elementary Differential Geometry*. Springer Science & Business Media, 2010.

[14] A. Ioffe, "Radar based environment representation for automated driving," in *First International IQPC Conference on Vehicle Intelligence: From Imaging to Sensor Fusion and Deep Learning*, Munich, Germany, Dec. 2017.

[15] "HFSS manual created by ANSYS in the United States. Accessible through a licensed version of the software."

[16] H. Ling, R.-C. Chou, and S.-W. Lee, "Shooting and bouncing rays: Calculating the RCS of an arbitrarily shaped cavity," *IEEE Transactions on Antennas and propagation*, vol. 37, no. 2, pp. 194–205, 1989.

[17] J. Baldauf, S.-W. Lee, L. Lin, S.-K. Jeng, S. Scarborough, and C. Yu, "High frequency scattering from trihedral corner reflectors and other benchmark targets: SBR versus experiment," *IEEE Transactions on Antennas and Propagation*, vol. 39, no. 9, pp. 1345–1351, 1991.

[18] "FEKO manual created by Altair Engineering in the United States. Accessible through a licensed version of the software."

[19] "Wavefarer manual created by Remcom Inc in the United States. Accessible through a licensed version of the software."

[20] A. Porubiaková and J. Komačka, "A comparison of dielectric constants of various asphalts calculated from time intervals and amplitudes," *Procedia Engineering - Elsevier*, vol. 111, pp. 660–665, 2015.

[21] C. A. Balanis, *Antenna Theory: Analysis and Design*. John Wiley & Sons Inc., 2015.

[22] M. Saifo, A. Ioffe, M. Stefer, and M. Clemens, "Using rcs radial pattern combined with multi-path effect for automotive radar simulations," in *2022 52nd European Microwave Conference (EuMC)*, 2022, pp. 286–289.

[23] D. B. Davidson, *Computational Electromagnetics for RF and Microwave Engineering*. Cambridge University Press, 2010.

[24] P. Rajyalakshmi and G. Raju, "Characteristics of radar cross section with different objects," *International Journal of Electronics and Communication Engineering*, vol. 4, no. 2, pp. 205–216, 2011.

[25] M. Saifo, A. Ioffe, M. Stefer, and M. Clemens, "The effect of facet size on the rcs simulation of an automotive radar target with curved surface," in *2022 14th German Microwave Conference (GeMiC)*, 2022, pp. 01–04.

[26] E. Miller, D. Andersh, and A. Terzuoli, "The effect of target model facetization on rcs predictions," in *Proceedings of IEEE Antennas and Propagation Society International Symposium*. IEEE, 1993, pp. 1404–1407.

[27] M. Christensen, S. Ni, and D. Reeves, "Interpolation to increase facet resolution for rcs," in *IEEE Antennas and Propagation Society International Symposium 1992 Digest*. IEEE, 1992, pp. 961–964.

[28] Y. M. Wu, L. J. Jiang, E. Wei, and W. C. Chew, "The numerical steepest descent path method for calculating physical optics integrals on smooth conducting quadratic surfaces," *IEEE Transactions on Antennas and Propagation*, vol. 61, no. 8, pp. 4183–4193, 2013.

[29] G. Carluccio, M. Albani, and P. H. Pathak, "Uniform asymptotic evaluation of surface integrals with polygonal integration domains in terms of UTD transition functions," *IEEE Transactions on Antennas and Propagation*, vol. 58, no. 4, pp. 1155–1163, 2010.

[30] Y. M. Wu, W. C. Chew, and L. J. Jiang, "Reducing computational workload of electromagnetic scattered fields from electrically large quadratic surface at high frequency," in *2013 IEEE Antennas and Propagation Society International Symposium (APSURSI)*. IEEE, 2013, pp. 1892–1893.

[31] J. Li and S. Li, "A high precision shooting and bouncing rays method without mesh for scattering calculation of complex target," *International Journal of*

Numerical Modelling: Electronic Networks, Devices and Fields, vol. 32, no. 6, p. 2600, 2019.

[32] A. Buffa and G. Sangalli, "Isogeometric analysis: A new paradigm in the numerical approximation of PDEs cetraro, italy 2012 preface," *Isogeometric Analysis: a New Paradigm in the Numerical Approximation of PDEs*, vol. 2161, pp. V–VI, 2016.

[33] M. Saifo, A. Ioffe, X. Cai, M. Stefer, and M. Clemens, "Extracting curvature information from low fidelity mesh for electromagnetic ray-tracing simulations in automotive scenarios," in *2023 53rd European Microwave Conference (EuMC)*, 2023, pp. 476–479.

[34] A. Razdan and M. Bae, "Curvature estimation scheme for triangle meshes using biquadratic bézier patches," *Computer-Aided Design*, vol. 37, no. 14, pp. 1481–1491, 2005.

[35] M. Szilvási-Nagy and S. Béla, "B-spline patches fitting on surfaces and triangular meshes," *KoG (Croatian Society for Geometry and Graphics)*, vol. 15, no. 15, pp. 17–24, 2011.

[36] C. Sigg, T. Weyrich, M. Botsch, and M. H. Gross, "GPU-based ray-casting of quadratic surfaces." in *PBG@ SIGGRAPH*, 2006, pp. 59–65.

[37] W. Barth and W. Stürzlinger, "Efficient ray tracing for bezier and b-spline surfaces," *Computers & Graphics*, vol. 17, no. 4, pp. 423–430, 1993.

[38] N. Max, "Weights for computing vertex normals from facet normals," *Journal of Graphics Tools*, vol. 4, no. 2, pp. 1–6, 1999.

[39] S. Rusinkiewicz, "Estimating curvatures and their derivatives on triangle meshes," in *Symposium on 3D Data Processing, Visualization, and Transmission*. IEEE, 2004.

[40] "Corner reflectors," https://www.radartutorial.eu/17.bauteile/bt47.en.html, accessed: 2026-05-01.

[41] "Corner reflectors," https://www.microwaves101.com/encyclopedias/corner-reflectors, accessed: 2026-05-01.

[42] W. Yang, C. Y. Kee, and C.-F. Wang, "Novel extension of SBR–PO method for solving electrically large and complex electromagnetic scattering problem in half-space," *IEEE Transactions on Geoscience and Remote Sensing*, vol. 55, no. 7, pp. 3931–3940, 2017.

[43] J. T. Johnson, "A study of the four-path model for scattering from an object above a half space," *Microwave and Optical Technology Letters*, vol. 30, no. 2, pp. 130–134, 2001.

[44] W. Yang and C.-F. Wang, "Half-space green's function and ray tracing method for em scattering from the large object on a ground," in *2016 Progress in Electromagnetic Research Symposium (PIERS)*. IEEE, 2016, pp. 1646–1646.

[45] W. Yang, T.-T. Chia, C.-Y. Kee, and C.-F. Wang, "An efficient high frequency method to compute electromagnetic scattering of large 3d target on rough surface," in *2015 IEEE International Symposium on Antennas and Propagation & USNC/URSI National Radio Science Meeting*. IEEE, 2015, pp. 1126–1127.

[46] L. Lozano, I. González, M. J. Algar, and F. Cátedra, "Efficient RCS analysis of complex targets on infinite ground plane," in *Proceedings of the 2012 IEEE International Symposium on Antennas and Propagation*. IEEE, 2012, pp. 1–2.

[47] S. B. J. Gowdu, A. Schwind, R. Stephan, and M. A. Hein, "Monostatic RCS measurements of a passenger car mock-up at 77 GHz frequency in virtual environment," in *2019 49th European Microwave Conference (EuMC)*. IEEE, 2019, pp. 996–999.

[48] R. Mavaddat, "The scattering paramters of a 2-port network," in *Network Scattering Parameters*. World Scientific, 1996.

[49] S. B. J. Gowdu, A. Schwind, R. Stephan, and M. A. Hein, "Monostatic RCS measurements of representative road traffic objects in the 76–81 GHz frequency band," in *2020 IEEE Radar Conference (RadarConf20)*. IEEE, 2020, pp. 1–6.

[50] L. Salman, S. Salman, and S. Carpenter, "mm-wave antenna array modeling for autonomous vehicle radar applications," *Academia.edu*, 2018.

[51] S. Buitrago, S. Blanch, and J. Romeu, "Automotive radar and radome calibration to improve the direction of arrival detection performance," in *12th European Conference on Antennas and Propagation (EuCAP 2018)*, 2018, pp. 1–5.

[52] M. A. Richards, *Fundamentals of Radar Signal Processing*. McGraw-Hill Education, 2014.

[53] M. A. Richards, J. Scheer, W. A. Holm, and W. L. Melvin, *Principles of Modern Radar*. Citeseer, 2010, vol. 1.